Doklady Physics, Vol. 46, No. 3, 2001, pp. 145–148. Translated from Doklady Akademii Nauk, Vol. 377, No. 1, 2001, pp. 30–33.

PHYSICS

Changes in the Elemental Composition of a Condensate under Basalt Impact Evaporation

L. I. Ivanov*, I. O. Sharikov*, V. P. Kolotov, N. N. Dogadkin**, O. I. Yakovlev**, and E. E. Kazilin*****

Presented by Academician V.V. Osiko May 29, 2000

Received June 20, 2000

Samples of the lunar ground were delivered to the Earth for the first time by the Apollo-11 (1969) and Apollo-12 missions, as well as by the Luna-16 (1970) and Luna-20 (1972) Soviet automatic stations. These samples stimulated studies devoted to the nature of the appearance of the lunar-surface dustlike cover, the so-called lunar regolith.

Two mechanisms of the regolith appearance were considered, namely volcanic and meteoritic. However, imitating investigations carried out for studying the formation of regolith from basalt, which is one of the basic substances of the lunar surface [1], have shown that the mechanism for regolith formation is meteorite action [2].

This fact confirms the important role of high-speed collisions of solids in both the formation of surface structure and possible differentiation of the elemental composition at the accretion stage and later stages of the development of planets and other extraterrestrial bodies [3]. It is evident that the principal cause for the formation of lunar-surface layers by precipitation of eruptions and partial condensation accompanying high-speed collisions is the high specific power of the energy release involved. This quantity may vary in broad limits depending on the velocity and mass of the incident bodies. Under lunar conditions, the mass of meteorites bombarding the lunar surface and their velocity lie within the limits of 10^{-10} to 10^{10} g and 3 to 70 km/s, respectively.

As was shown for the first time in [4], for velocities of a flying body higher than 14 km/s, the specific power of the energy release in collisions of solids may exceed 10^{14} W/cm^2. In this case, high-temperature plasma [5] must arise, with the ionic temperature lying in the energy range of several kiloelectronvolts. The consequence of this process is the complete evaporation of both the incident body and a part of the basic material in the impact zone independently of the chemical content of the interacting bodies. This fact is indirectly confirmed in the imitating experiments employing high-temperature pulse plasma generated in the "Plasma focus" facility [6].

The substance ejected as a result of collision of solids with an impact velocity exceeding 14 km/s propagates in extraterrestrial space in the form of clouds consisting of gas or dust. Their components may have different velocities depending on the mass and energy obtained at the moment of impact. In addition to the gas and dust components, liquid and solid particles of the basic material can be ejected from the impact zone. These particles arise owing to propagation of shock waves and their dissipation on inhomogeneities [7].

In the case of a decrease in the impact velocity, apart from the arising vapor phase, droplet forms of the ejected substance must play an ever increasing role, as this is characteristic of low-temperature plasma [8]. As applied to the conditions on the Moon (i.e., in the case of a weak gravity field and high vacuum), the components of the impact ejection with a velocity lower than 2.3 km/s will hit the lunar surface and form its structure. We should take into account therewith that at velocities of bombarding particles lower than 2 km/s, their super-deep penetration into the basic material is possible, which can result in changes in the chemical composition and structure over large thicknesses of near-surface layers.

Thus, it is possible that the arising lunar-surface layer, termed regolith, is a mixture of solid particles ejected as a result of meteorite impacts, solidified droplets, and the admixture of vapor-phase condensate. In this case, we can assume that the chemical composition of regolith may substantially differ from that of the basic substance and can depend, to a great extent, on the specific power of the energy released in impact. This is especially the case when the power is consider-

* *Baĭkov Institute of Metallurgy and Materials Science, Russian Academy of Sciences, Leninskiĭ pr. 49, Moscow, 117334 Russia*

** *Vernadskiĭ Institute of Geochemistry and Analytical Chemistry, Russian Academy of Sciences, ul. Kosygina 19, Moscow, 117975 Russia*

*** *Institute of Laser and Information Technology, Svyatozerskaya ul. 1, Shatura, Moscow oblast, 140700 Russia*

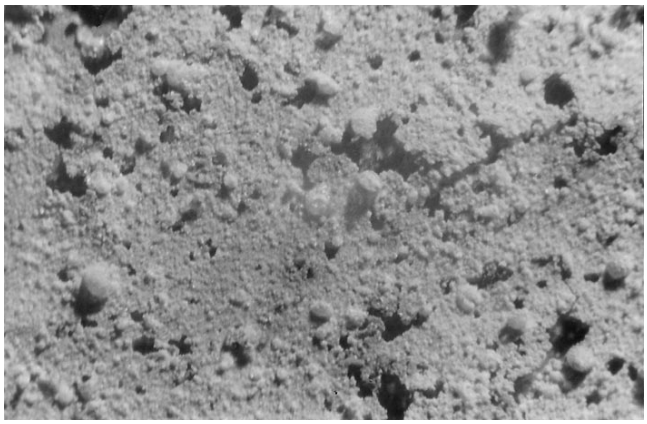

Fig. 1. Surface of the basalt condensate obtained as a result of evaporation under the action of a laser-pulse.

ably lower than 10^{14} W/cm^2 in the region of the formation of the low-temperature plasma.

In this paper, we investigate the morphology, structure, and chemical composition of natural-basalt condensate arising upon impact-induced destruction by laser pulses imitating actions of meteorites [10].

Here, in contrast to [2], principal attention is payed to studying the condensate in the region of the low specific power of the energy release (lower than 10^8 W/cm^2); this corresponds to velocities of meteorites (or their secondary fragments) close to 2.4 km/s.

The comparison of chemical contents for the condensate and the original lunar basic substance, i.e., basalt, makes it possible to estimate the distribution of constituting elements and to reveal their differentiation under impact evaporation and subsequent condensation of ejection products. This is quite important for clarification of the formation nature for the outer layer of the lunar surface.

As an initial material, we choose a usual volcanic rock (basalt) with Si, Ti, Al, Fe, Mg, Ca, Na, K as its basic chemical elements. The basalt surface was thoroughly polished and then subjected to the action of a pulsed-laser radiation with the following characteristics: wavelength $\lambda = 1.06$ μm, pulse energy = 100 J, and laser pulse duration = $\sim 10^{-3}$ s. In the present experiment, the radiation power density was varied within the limits of 10^6 to 10^7 W/cm^2. The temperature developed at the moment of the pulse hitting the target was ~4000 K [11].

The sample was fixed inside a vacuum chamber with an ultimate vacuum of 10^{-5} torr with the help of a special tripod system that allowed the sample position to be changed with respect to the system optical axis.

A laser pulse was introduced into the vacuum chamber with the help of a special optical system, making it possible to scan the sample surface. For collecting both the condensate and diverging products of pulse laser action, we used polished plates made of high-purity silicon, which were placed at a distance of 8 cm from the sample. After each pulse, several milligrams of the basalt-sample substance were ejected. The condensate-layer thickness attained approximately 0.1 mm. In order to obtain the necessary amount of condensate required for analysis, we had to produce several dozen laser shots for different regions of the basalt target. High-quality processing of the plate surface provided simple removal of the condensate film. This made it possible to solve a number of problems of analysis of the film elemental composition by the neutron-activation method.

Figure 1 exhibits a typical photograph of the condensate surface. It represents a finely divided film with glasslike melt droplets (glass spherulites) scattered on it. They are preferably of light color, although there are colorless forms among them. Many of the solidified drops have a spherical shape. The average diameter of the glass spherulites is ~1 μm.

As was shown in [8], one of the causes determining the appearance of solidified droplets is the carrying out from the walls by the low-temperature plasma of the melt crater produced as a result of the impact with the subsequent melt solidification, or at the divergence stage, or while hitting the condensate substrate. In the latter case, the structure and the morphology of the solidified droplets is, mainly, determined by the thermophysical properties of the substrate with all the characteristic features of the melt solidification in the case of directed heat removal and, in particular, by the appearance of a shrinkage cavity on the sample surface.

The obtained amount of condensate allowed us to determine the content of Na, Ca, Th, La, Ce, Sm, Eu, Yb, Lu, Sc, Fe, Co, and Cr in it. The instrumental (comparative) variant of the neutron-activation analysis was chosen as the determination method.

Synthetic multiple-element samples developed on the basis of phenol-formaldehyde resin were used as standards. The condensate, basic basalt, and standards were exposed with thermal neutrons of a fluence of $\sim 10^{17}$ neutrons cm^{-2}. The quantitative determination of the composition was performed with the help of gamma-spectroscopy methods accompanied by subsequent processing of the spectra obtained and calculation of the elemental concentrations according to the ASPRO code [14].

The data obtained concerning the content of elements in the original basalt and the condensate are presented in the table.

Comparison of the elemental content in the original basalt and in the condensate shows a stable tendency to the enrichment of the condensate by a number of certain chemical elements present in the basalt substance. This tendency is clearly seen in Fig. 2 (curve *1*), in which the content of chemical elements in the condensate is normalized to their content in the original basalt.

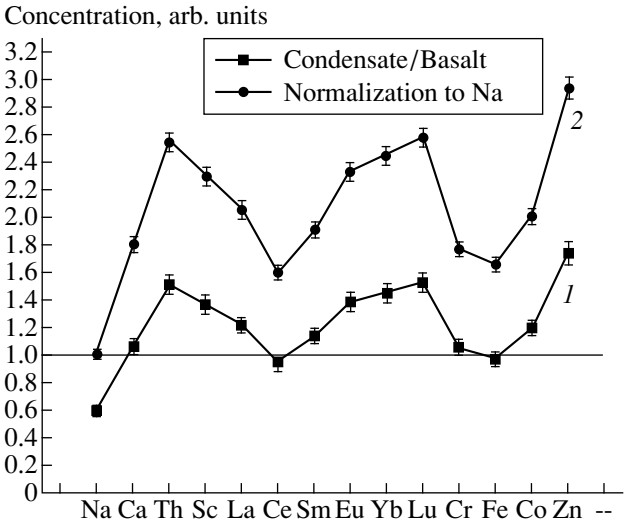

Fig. 2. Relative abundance of elements in the condensate and basalt.

The maximum enrichment, approximately by a factor of 1.4, is observed for thorium, ytterbium, and lutecium.

The results obtained confirm the previous qualitative observations testifying to the fact of differentiation of the elements present in the original basalt [15].

Elemental content in lunar basalt and in the condensate

Element	Basalt		Condensate		*n*
	content, ppm	standard deviation σ, %	content, ppm	standard deviation σ, %	
Na	1.62	0.29	0.96	0.21	3
Zn	109	20.5	192	25	1
Ca	5.22	1.24	5.57	1.18	3
Th	1.07	0.64	1.6	0.6	2
Sc	30.2	5.4	41.2	1.4	4
La	7.09	1.19	8.65	1.53	3
Ce	21.1	7.5	20.1	7.3	3
Sm	2.96	0.50	3.35	0.76	3
Eu	0.83	0.10	1.08	0.20	5
Yb	1.73	0.80	2.52	0.32	3
Lu	0.26	0.05	0.39	0.03	3
Cr	98.5	28.1	103.6	25.4	2
Fe	7.85	1.12	7.74	1.21	3
Co	41.0	8.1	49.1	6.7	4

Note: Contents of Na, Ca, and Fe are given in mass percent; *n* is the number of independent experiments.

Curve *2* (Fig. 2) exhibits a relative abundance (normalized to sodium concentration) of elements in the condensate, which is substantially smaller than in the original basalt [15]. We may conclude that the concentration of such elements as thorium, scandium, lanthanium, samarium, europium, ytterbium, and lutecium, as well as cobalt and zinc, in the condensate considerably exceeds that in the original basalt. This can be associated with the following processes:

the complete or partial dissociation of oxides and formation of low-temperature plasma (the specific energy-release power attains 10^8 W cm^{-2}, the temperature is 4000 K);

formation of clusters at the divergence of the vapor phase when decreasing its temperature with subsequent condensation;

transformation of silicate-melt oxides of various elements into the vapor phase under conditions of thermodynamically nonequilibrium processes.

In the case when the droplets present in the diverging low-temperature plasma solidify in the process of plasma divergence, they are observed in the condensate in the form of perfect spheres (see Fig. 1). Similar spherical formations can be found in the Moon regolith [12].

In this paper, absolute values are found for the content of more than ten elements in the condensate. It is important that this condensate was obtained in the process of laser-pulse evaporation, which, to a great extent, illustrates the role of basic rock ejection in the formation of lunar regolith.

On this basis, the conclusion can be made that impact evaporation under meteorite action is of important significance for understanding the physical processes of the elemental distribution in dust formations on the lunar surface. This is indirectly confirmed by the data obtained by the lunar orbital mission “Lunar Prospector” (USA, 1998), which are based on the uniform distribution of thorium in the lunar regolith on different areas of the Moon’s surface.

CONCLUSIONS

For the first time, the elemental distribution in the condensate of basalt, i.e., of basic lunar rock, is investigated quantitatively under an impact laser-pulse action imitating that of meteorite fluxes. The effect of the selective enrichment of the condensate by a number of elements constituting the basalt content is revealed.

It is shown that the morphology of the condensate surface under the imitating studies indicates, in part, the actual morphology of the surface ground of the Moon.

REFERENCES

1. I. I. Cherkasov and V. V. Shnyrev, *The Ground of the Moon* (Nauka, Moscow, 1975).

2. M. D. Nusinov, A. V. Kuznetsov, K. P. Florenskiĭ, *et al.*, Dokl. Akad. Nauk SSSR **202**, 811 (1972) [Sov. Phys.–Dokl. **17**, 138 (1972)].
3. O. I. Yakovlev, Yu. P. Dikov, and M. V. Gerasimov, Geokhimiya, No. 8, 1235 (1995).
4. Ya. B. Zel'dovich and Yu. P. Raizer, *Physics of Shock Waves and High-Temperature Hydrodynamic Phenomena* (Nauka, Moscow, 1963; Academic, New York, 1966).
5. R. Opwer and E. Burlefinger, Phys. Lett. **16**, 37 (1965).
6. S. A. Maslyaev, V. N. Pimenov, Yu. M. Platov, *et al.*, Perspektivnye Mater., No. 3, 39 (1998).
7. K. Vegel and P. Backland, J. Appl. Phys. **36**, 3697 (1965).
8. C. Korer, R. Mauerhofer, and M. Hartman, J. Appl. Phys., No. 3, 123 (1966).
9. L. V. Obukhov, L. I. Ivanov, V. L. Yanushkevich, *et al.*, USSR Inventor's Certificate No. 67473, 1972.
10. V. A. Yanushkevich, in *Proceedings of All-Union Workshop-Seminar, 1969* (Moscow, 1972), Part 3, p. 295.
11. M. V. Gerasimov, L. M. Mukhin, Yu. P. Dikov, *et al.*, Vestn. Akad. Nauk SSSR, Nos. 9–10 (1985).
12. O. D. Rodé, A. V. Ivanov, M. A. Nazarov, *et al.*, *Atlas of Microphotographs for Lunar-Ground Particle Surfaces* (Prague, 1979).
13. V. Kolotov and V. Atrashkevich, J. Ratioanal Nucl. Chem. **193** (2), 195 (1995).
14. O. I. Yakovlev, A. Yu. Lyul', G. M. Kolesov, *et al.*, Geokhimiya, No. 11, 1426 (1992).
15. M. V. Gerasimov, Yu. P. Dikov, and O. I. Yakovlev, Meteor. Planet. Sci. **34**, 42 (1999).

Translated by G. Merzon

Doklady Physics, Vol. 46, No. 3, 2001, pp. 149–152. Translated from Doklady Akademii Nauk, Vol. 377, No. 2, 2001, pp. 180–182.

PHYSICS

On Pressure Fluctuations and Spectra of Light Scattered on Elastic Thermal Waves

Corresponding Member of the RAS I. L. Fabelinskiĭ

Received September 25, 2000

1. In a perfectly pure condensed medium in which any extraneous inclusions or waviness are absent, light scattering occurs upon fluctuations of the optical dielectric constant. These fluctuations are caused by fluctuations of thermodynamic and nonthermodynamic quantities, such as fluctuations of pressure Δp, entropy Δs or temperature ΔT, solution concentration Δc, and anisotropy $\Delta\xi_{ik}$.

Since only light scattering caused by pressure fluctuations is considered below, we present the calculation of the average value of Δp squared, which was performed by Einstein [1], who developed a method for determining thermodynamic fluctuations and obtained the result

$$\langle \Delta p^2 \rangle = \frac{kT}{V^* \beta_s}. \quad (1)$$

Here, k, T, V^*, and β_s are the Boltzmann constant, the absolute temperature, the fluctuation volume, and the adiabatic compressibility, respectively. Furthermore, $\beta_s = \rho^{-1} v^{-2}$, where ρ and v are the density and adiabatic sound phase velocity.

It is rather difficult to precisely obtain the quantity Δp since far from the critical point under normal conditions, we can determine the fluctuation volume V^* only with an accuracy to an order of magnitude. Assuming that the linear size $\bar{l}$ of a fluctuation is $\sim \frac{\lambda}{25}$, where λ is the wavelength of the visible light,[1] pressure fluctuations, e.g., in a liquid attain ~0.1% of the internal pressure.

In calculating the scattered-light intensity, Einstein [1] (for liquid volumes and solutions) and Mandelstam [2] (at the interface between two media) expanded fluctuations into a Fourier series, i.e., into "formal waves."

In these studies, the expansion into formal waves represents an approach which makes it possible to calculate the intensity of scattered light.

Even before, Einstein [3] developed a theory of heat capacity of solids in which he employed the Planck formula assuming that $\hbar\Omega\left(\exp\frac{\hbar\Omega}{kT}\right)^{-1}$ (instead of the previously used kT) per degree of freedom. Thus, the heat capacity turned out to be a function of the frequency Ω of proper vibrations of atoms being contained in a solid and the absolute temperature T. It seemed that the heat-capacity theory had nothing to do with the scattering of light. In any case, even Einstein did not mention it.

However, the heat-capacity theory for solids in the region of low temperatures, which was developed by Einstein, needs improvement.

Continuing Einstein's concepts [3], Debye proposed in [4] a beautiful idea which represents a solid consisting of a large number N of particles as a continuum described by equations of elasticity theory.

To calculate the energy of a solid, it was assumed that $3N$ degrees of freedom of coupled oscillators were equivalent to $3N$ elastic waves.[2] Hence, the kinetic energy of the body's particle thermal motion was the energy of the elastic waves. In this study, the theory of light scattering (diffraction) on elastic waves was also not mentioned.

Apparently, Mandelstam [5, 6] was the first to understand that both Einstein's [1] and Mandelstam's [2] formal waves, Fourier components, and Debye thermal waves are the same phenomena. Therefore, the theory of heat capacity for a solid and the theory of light scattering do not differ from each other, and from this standpoint, pressure fluctuations are a result of interference of Debye elastic waves.

Light scattering is the diffraction of exciting light on elastic waves, and the scattered-light spectrum differs

[1] For such $\bar{l}$, the indicatrix of the scattered light intensity does not exhibit angular asymmetry.

Lebedev Physics Institute, Russian Academy of Sciences, Leninskiĭ pr. 53, Moscow, 117924 Russia

[2] Apparently in this case, not all degrees of freedom are taken into account, but the basic features of the phenomenon under consideration are.

1028-3358/01/4603-0149$21.00

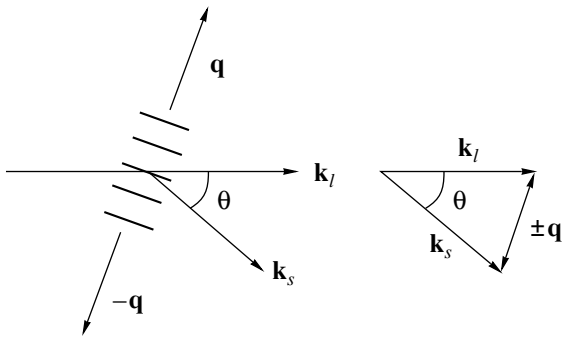

Propagation direction for light and elastic waves is determined by wave vectors $\mathbf{k}_l$ for exciting light, $\mathbf{k}_s$ for scattered light, and $\pm\mathbf{q}$ for elastic waves.

from that of exciting light due to the Doppler effect or the scattered-light modulation [7].

2. It follows from the model of a solid proposed by Debye [4] that although it represents a continuum, the frequencies of its elastic vibrations are bounded by a certain maximum frequency Ω_{max}. There is a set of elastic-vibration frequencies between $\Omega = 0$ and Ω_{max}, such that $d\Omega$ corresponds to the frequency range $dZ(\Omega)$ [4, 8], namely,

$$dZ(\Omega) = V\frac{3\Omega^2 d\Omega}{2\pi^2 v^3}, \qquad (2)$$

where V is the volume of the sample being studied and v is the mean sound phase velocity. The maximum frequency Ω_{max} is determined from the condition

$$Z(\Omega_{max}) = \int_0^{\Omega_{max}} dZ(\Omega) = V\frac{\Omega_{max}^3}{2\pi^2 v^3} = 3N. \qquad (3)$$

Assuming $\frac{V}{N} = d^3$, where d is the distance between the particles, we find from the definition of d and Eq. (3) [8]

$$\Omega_{max} = \left(\frac{3}{4\pi}\right)^{1/2}\frac{2\pi v}{d}, \quad \Lambda_{min} = \left(\frac{4\pi}{3}\right)^{1/3} d. \qquad (4)$$

Here, Λ is the minimum wavelength of the elastic wave. Within the limits from 0 to Ω_{max}, there are waves with different frequencies and different directions of propagation, i.e., different wave vectors $\mathbf{q}$.

Under these conditions, a pair of waves forming a standing wave with the same Ω and directly opposite $\pm\mathbf{q}$ can always be found (Fig. 1). On this standing wave, there occurs diffraction (scattering) of light propagating at an angle θ to the exciting light and along the direction corresponding to the Bragg condition [8].

The effective amplitude of the thermal wave can be estimated from the energy density of the elastic plane wave:

$$E_\Omega = \rho c^2 = \rho A_{eff}^2 \Omega^2, \qquad (5)$$

where c is the vibrational velocity of the wave, ρ is the density, and A_{eff} is the effective amplitude of the elastic wave.

On the other hand, following Einstein, the photon energy can be expressed by the Planck formula.

In the case under consideration, $\frac{\hbar\Omega}{kT} \ll 1$, the Planck formula transforms into the Rayleigh–Jeans formula:

$$E_\Omega = \frac{kT\Omega^2 d\Omega}{\pi^2 v^3}. \qquad (6)$$

Comparing (5) and (6), we obtain for the effective amplitude of the elastic wave

$$A_{eff} = \left(\frac{kTd\Omega}{\pi^2 \rho v^3}\right)^{1/2}. \qquad (7)$$

For example, in the case of benzene, assuming T = 300 K, $\rho = 0.8$, $v = 1.5 \times 10^5$ cm/s, and $d\Omega \simeq 10^9$ rad/s, we have

$$A_{eff} = 5 \times 10^{-11} \text{ cm}.$$

However, we should note that formula (7) contains the multiplier $d\Omega$, which introduces a certain indeterminacy in the quantitative calculation. The reason for this is that it is unclear what frequency range is implied for $d\Omega$. In our calculation, we accept $d\Omega$ as corresponding to the half-width of the Mandelstam–Brillouin component since there is no other natural quantity for $d\Omega$.

The most important conclusion from relation (7) is the following. If A_{eff} is independent of the coordinate and time, the thermal wave, hence, attenuates neither in space nor in time.

3. Owing to the time variation of pressure in the standing wave, scattered (diffracted) light is modulated with an elastic-wave frequency Ω. For a constant amplitude and phase of the light elastic wave, the spectrum of this modulated oscillation is described by the δ-function. However, it is well known that the spectrum of the molecular scattering of light yields a finite width for the Mandelstam–Brillouin components [8, 9].

By virtue of arising and decaying fluctuations, the waves forming a "diffraction grating" (Fig. 1) have a

constant amplitude, but the phase $\varphi(t)$ changes in time. For a plane wave,

$$A = A_{\text{eff}}\cos[\Omega t - \varphi(t)], \tag{8}$$

where, far from the critical temperature, $\varphi(t)$ is described by the normal, or Gaussian, distribution.

In the case of excitation of scattered light by a plane wave with frequency ω and amplitude E_0 and its modulation by the elastic wave of form (8), we find for the scattered-light field

$$E(t) \approx \frac{1}{2}A_{\text{eff}}E_0 \times \{\cos[(\omega - \Omega)t + \varphi(t)] + \cos[(\omega + \Omega)t - \varphi(t)]\}. \tag{9}$$

The first term in (9) corresponds to the Stokes (Mandelstam–Brillouin) component; the second, to the anti-Stokes component.[3] Both lines are the same, and here, we consider the shape of one of them.

The problem of calculating the spectrum shape of the signal when its amplitude is constant and the phase varies with time according to the Gauss law, i.e., the white-noise problem, is important for radio physics and has been analyzed many times. Here, in solving the optical problem, we use the results obtained by Malakhov [10] for the frequency of a generator.

The variation of the phase with time in (9) is the same as the frequency variation, so that in this case,

$$\varphi(t) = \int_{t_0}^{t}\Delta\omega(t)dt. \tag{10}$$

Here, $\Delta\omega(t)$ is the frequency fluctuation whose average value equals zero.

The spectral density of the scattered light intensity is determined as

$$I(\omega) = \frac{2}{\pi}\int_0^\infty \Phi(t)\cos\omega t dt, \tag{11}$$

where

$$\Phi(t) = \lim_{T\to\infty}\frac{1}{T}\int_0^T E(t)E(t+\tau)dt.$$

Here, $\Phi(t)$ is the correlation function, $E(t)$ corresponds to formula (9), and τ is the correlation time in the ergodic ensemble in which the fluctuations are mutually independent.

Using the rather cumbersome calculations performed in [10], the spectral density for the intensity when $[\langle\Delta\omega^2\rangle\tau^2] \ll 1$ can be written in the form

$$I(\omega) = I\frac{\frac{\langle\Delta\omega^2\rangle}{2K}}{(\omega-\Omega)^2 + \left(\frac{\langle\Delta\omega^2\rangle}{2K}\right)^2}. \tag{12}$$

Here, K is a constant with the dimension of frequency, I is the intensity, and $\Delta\omega$ in the radiophysical case is the frequency deviation from the radiator frequency.

In the optical case, the half-width of the Mandelstam–Brillouin component is

$$\delta\omega = \frac{\langle\Delta\omega^2\rangle}{2K}. \tag{13}$$

Formula (12) represents the result of kinematic calculations without allowance for masses of particles, their properties, and forces acting on them. Therefore, relation (13) cannot be applied to calculate substance parameters (e.g., absorption of sound). However, it is substantial that in the case of Gaussian statistics, we obtain for $I(\omega)$ an expression of the same form as for the solution of the dynamical problem. This dynamical calculation was performed previously (see, e.g., [8, 9]) in the same approximation and yielded the following result:

$$I(\omega) = Iad\frac{\frac{\delta}{\pi}}{(\omega-\Omega)^2 + \delta^2}. \tag{14}$$

Here, δ is the half-width of the Mandelstam–Brillouin component, which is $\delta = \frac{1}{2}\Gamma q^2$, where Γ is the time attenuation constant of the elastic wave and $\mathbf{q}$ is the wave vector. Comparing (12) and (14), we can understand the physical meaning of the frequency deviation in the spectrum of the molecular scattering of light.

ACKNOWLEDGMENTS

The author is grateful to L.P. Presnyakov for fruitful discussions.

This work was supported by the Russian Foundation for Basic Research, project no. 99-02-18483a.

REFERENCES

1. A. Einstein, Ann. Phys. **33**, 1275 (1910); *Collection of Scientific Papers* (Nauka, Moscow, 1966), Vol. 3, pp. 216–236.

[3] The central component is also presented in the spectrum (Rayleigh line) due to scattering on fluctuations of the entropy or temperature. However, the behavior of the central line is outside the scope of this paper.

2. L. Mandelstam, Ann. Phys. **41**, 609 (1913), *Full Collection of Papers* (Akad. Nauk SSSR, Moscow, 1948), Vol. 1, p. 246.
3. A. Einstein, Ann. Phys. **22**, 180 (1907); *Collection of Scientific Papers* (Nauka, Moscow, 1966), Vol. 3, pp. 134–143.
4. P. Debye, Ann. Phys. **39**, 789 (1912); *Selected Papers* (Nauka, Leningrad, 1987), pp. 436–79.
5. L. I. Mandelstam, Zh. Russ. Fiz.-Khim. O–va **58**, 381 (1926).
6. L. I. Mandelstam and G. S. Landsberg, Zh. Prikl. Fiz. **6**, 155 (1929).
7. G. S. Landsberg, Usp. Fiz. Nauk **36**, 284 (1948); *Selected Papers* (Akad. Nauk SSSR, Moscow, 1958), pp. 348–354.
8. I. L. Fabelinskiĭ, *Molecular Scattering of Light* (Nauka, Moscow, 1965; Plenum, New York, 1968).
9. I. L. Fabelinskiĭ, Usp. Fiz. Nauk **164**, 897 (1994) [Phys. Usp. **37**, 821 (1994)].
10. A. N. Malakhov, Zh. Éksp. Teor. Fiz. **30**, 884 (1956).
11. V. L. Ginzburg, *Theoretical Physics and Astrophysics* (Nauka, Moscow, 1987; Pergamon, Oxford, 1979).

Translated by G. Merzon

Doklady Physics, Vol. 46, No. 3, 2001, pp. 153–156. From Doklady Akademii Nauk, Vol. 377, No. 3, 2001, pp. 321–324.

THEORETICAL PHYSICS

Hyperviscosity of a Magnetized Plasma[1]

A. B. Mikhaĭlovskiĭ*, S. V. Konovalov*, and V. S. Tsypin**

Presented by Academician A.M. Fridman September 12, 2000

Received September 15, 2000

According to [1], the transverse electric field in magnetized plasma depends on the plasma transverse viscosity. Here, the term "transverse" implies vector or tensor components transverse to the direction of the magnetic field in plasma. For example, in the simplest case of two-dimensional geometry when the magnetic field **B** is directed along the *z*-axis of the Cartesian (*x*-, *y*-, *z*-) coordinate system, **B** ∥ **z**, the electric field **E** and its gradient are directed along the *x*-axis, **E** ∥ **x**, $\nabla E_x \parallel \mathbf{x}$ (**x**, **z** are the unit vectors along *x*, *z*). The spatial dependence of the field **E**, i.e., the function $E_x(x)$, is determined by the equation

$$\frac{\partial \pi_{zy}}{\partial x} = 0, \tag{1}$$

where π_{xy} is the corresponding component of the plasma viscosity tensor.

The conventional transport theory of magnetized plasma [2] yields the following expression for π_{xy}:

$$\pi_{xy} = -nT\frac{\nu_{\text{eff}}}{\omega_B^2}\frac{\partial V_y}{\partial x}. \tag{2}$$

Here, $V_y = -\dfrac{cE_x}{B}$ is the drift velocity in crossed (**E**, **B**) -fields, *c* is the speed of light, *n* is the density of the number of particles in the plasma, *T* is the ionic temperature, ω_B is the ion cyclotron frequency, and ν_{eff} is the effective ion-collision frequency.

We now use Eqs. (1) and (2) for studying the following problem. We assume that the half-plane $x < 0$ is occupied by quiescent plasma or by any other conducting medium in which $E_x \equiv 0$. At the same time, in the half-plane $x > 0$, there is plasma with a homogeneous density and temperature and, according to the equilibrium equation, the magnetic field is uniform. The question arises as to whether we can produce, in the region $x > 0$, a certain electric field $E_x(x) \neq 0$ bounded as $x \longrightarrow \infty$ under the condition $E_x(0) = 0$. This condition implies the absence of a jump of the plasma velocity V_y at the interface between the two media mentioned above. It follows from (1) and (2) that the answer is negative. Only a trivial solution $E_x \equiv 0$ and a solution growing linearly with increasing *x*, i.e., $E_x \sim x$, can be found for $x > 0$ from (1) and (2) within the scope of the given statement of the problem.

At this stage, another question arises: whether the above mathematical result describes an actual physical situation or is a consequence of a certain defect in our statement of the problem? In this connection, we note that expression (2) for π_{xy} was derived in [2] using expansion in a series with respect to the ratio of the ion Larmor radius ρ_i to the characteristic length *L* of the electric field inhomogeneity, $\dfrac{\rho_i}{L} \ll 1$. However, for the problem which we are interested in, the higher derivatives of the electric field E_x and, correspondingly, the velocity V_y have jumps at $x = 0$. This implies that $L = 0$ for $x = 0$. Consequently, the standard expression (2) for π_{xy} at the interface between two media is invalid and the above-formulated result on the possibility of creating the field $E_x \neq 0$ for $x > 0$ is doubtful.

It is evident that for correct solution of this problem, it is necessary to generalize formula (2) for π_{xy} without expanding it in a power series with respect to the ionic Larmor radius squared. At the same time, it is of interest to elucidate what we can obtain using the model expression for π_{xy}, which differs from (2) in its term with the third derivative of the velocity V_y, i.e., using the expression of the form

$$\pi_{xy} = -nT\frac{\nu_{\text{eff}}}{\omega_B^2}\left(\frac{\partial V_y}{\partial x} - c_L\rho_i^2\frac{\partial^3 V_y}{\partial x^3}\right), \tag{3}$$

where c_L is a certain numerical coefficient whose sign is yet assumed arbitrary. We call this term hyperviscosity. It is worth noting that the concept of hyperviscosity was used previously in modeling the problem of geodynamics (see, e.g., [3]), which is beyond the scope of

* *Institute of Nuclear Fusion, Russian Research Center Kurchatov Institute, pl. Kurchatova 1, Moscow, 123182 Russia*

** *University of Sáo Paulo, Rua do Matáo, Sáo Paulo, Brasil*

[1] The article was submitted by the authors in English.

1028-3358/01/4603-0153$21.00

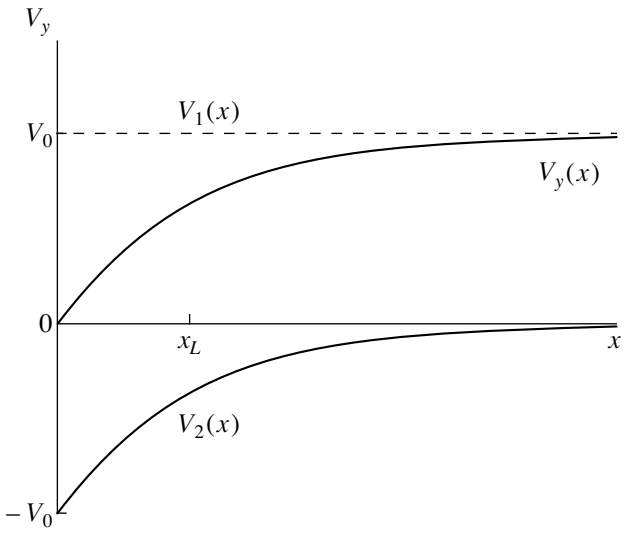

Qualitative dependence of the $V_y(x)$ corresponding to the viscosity model of form (3).

plasma physics. As for plasma physics, we may mention study [4], which dealt with hyperviscosity when numerically simulating two-dimensional drift turbulence.

Let $c_L > 0$. Then, for $x > 0$, we can construct, with the help of (1), the solution

$$V_y(x) = V_1(x) + V_2(x), \quad (4)$$

where

$$V_1(x) = V_0 = \text{const}, \quad (5)$$

$$V_2(x) = -V_0 \exp\left(-\frac{x}{x_L}\right), \quad (6)$$

with $x_L = c_L^{1/2}\rho_i$. This solution satisfies the above condition $V_y(0) = 0$. Qualitatively, this solution is represented in Fig. 1.

Expression (3) for π_{xy} is the simplest model allowing for hyperviscosity. A more complicated expression including the term with the fifth velocity derivative is

$$\pi_{xy} = -nT\frac{\nu_{\text{eff}}}{\omega_B^2}\left(\frac{\partial V_y}{\partial x} - c_L\rho_i^2\frac{\partial^3 V_y}{\partial x^3} + d_L\rho_i^4\frac{\partial^5 V_y}{\partial x^5}\right), \quad (7)$$

where, similarly to c_L, d_L is a numerical coefficient. By means of Eqs. (2) and (7), for some additional assumptions on the coefficients c_L, d_L (for details see below) in the region $x > 0$, we can construct the solution for $V_y(x)$, which, at $x = 0$, satisfies the condition of continuity for both the velocity, $V_y(0) = 0$, and its first derivative, $\left(\frac{\partial V_y}{\partial x}\right)_{x=0} = 0$. This solution can be represented in the form of (4) with $V_1(x)$ of form (5) and $V_2(x)$, which is the following generalization of (6):

$$V_2 = -\frac{V_0}{2}\left\{\left(1 + \frac{i\kappa}{k}\right)\exp[-(\kappa + ik)x] + \text{c.c.}\right\}. \quad (8)$$

Here c.c. implies the complex conjugation, $\kappa = \frac{\cos(\delta/2)}{d_L^{1/4}\rho_i}$, $k = \frac{\sin(\delta/2)}{d_L^{1/4}\rho_i}$, $\delta = \arccos\left[\frac{c_L}{2d_L^{1/2}}\right]$. Solution (8) oscillates in space and, at the same time, decays while moving away from the point $x = 0$ under the condition

$$d_L > \frac{c_L^2}{4}. \quad (9)$$

The period of spatial oscillations and the characteristic decay length are comparable with the ionic Larmor radius. Qualitatively, the function $V_2(x)$ of form (8) and the total velocity $V_y(x)$ characterized by formulas (4), (5), and (8) are similar to those given in Fig. 1; the only difference lies in the fact that there are now decaying oscillations on both $V_2(x)$ and $V_y(x)$.

Thus, in the case of either the viscosity model of form (3) with positive c_L or the model of form (7) with arbitrary-sign c_L and positive d_L, which satisfy condition (9), we can construct the desired solution with finite $E_x(x) \neq 0$ in the region $x > 0$. However, a new question arises: can the plasma theory yield the coefficients c_L and d_L satisfying these requirements? This problem was studied in [5] in the framework of the multimoment description of hydrodynamic plasma, which goes back to the Grad approach [6]. The values $c_L = \frac{5}{3}$ and $d_L = \frac{553}{300}$ found for this case confirm the validity of condition (9). However, it seems to be important to elucidate the consistency of these qualitative results with the kinetic plasma theory. This implies direct calculation of hyperviscosity on the basis of the Boltzmann kinetic equation, which is the goal of our following analysis.

Let F be the ion equilibrium distribution function, i.e., the solution of the Boltzmann kinetic equation obtained with ignoring the derivatives of $V_y(x)$. These derivatives cause a perturbation of the ion distribution function denoted as f. This perturbation is described by the perturbed part of the Boltzmann kinetic equation, which, according to [7], can be reduced to the form

$$v_\perp\cos\vartheta\frac{\partial f}{\partial x} + \frac{Mv_\perp^2}{2T}F\sin 2\vartheta\frac{\partial V_y}{\partial x} = \omega_B\frac{\partial f}{\partial\vartheta} + C(f). \quad (10)$$

Here, $C(f)$ is the collisional term. The particle velocity is represented in the form

$$\mathbf{v} = V_y\mathbf{y} + v_\perp(\mathbf{x}\cos\vartheta + \mathbf{y}\sin\vartheta),$$

so that $v_\perp$ is the modulus of the particle transverse velocity in the reference frame moving in crossed fields with the drift velocity and ϑ is the Larmor gyration phase of a particle. The collisional term $C(f)$ is taken in the model form allowing for momentum conservation:

$$C(f) = -\nu\left[f - \frac{Mv_\perp}{T}UF\cos\vartheta\right],$$

where ν is the model ion-collision frequency; U is the y-component of the ion velocity in the above-mentioned reference frame; and

$$U = \int\frac{v_\perp\cos\vartheta f d\mathbf{v}}{n}, \quad d\mathbf{v} = v_\perp dv_\perp d\vartheta.$$

For simplicity, we restrict ourselves to the problem of two-dimensional velocity distribution.

Our goal is to calculate the function f and to find the viscosity-tensor component π_{xy} defined by the relation

$$\pi_{xy} = M\int\frac{v_\perp^2}{2}\sin 2\vartheta f d\mathbf{v}. \tag{11}$$

We use the Fourier transformation assuming that each perturbed function $X(x)$ is represented by the Fourier integral of the form

$$X(x) = \int\exp(ikx)X_k dk, \tag{12}$$

where X_k is the Fourier component of $X(x)$. Then, Eq. (10) transforms to

$$\left(\frac{\partial}{\partial\vartheta} - \frac{\nu}{\omega_B} - ib\cos\vartheta\right)f_k = 2\gamma\sin 2\vartheta - 2\beta\sin\vartheta. \tag{13}$$

Here, $b = \dfrac{kv_\perp}{\omega_B}$; the functions γ and β are defined by the relations

$$\gamma = \frac{Mv_\perp^2 F\Gamma_k}{4T\omega_B}, \beta = \frac{\nu Mv_\perp FU_k}{2\omega_B T}, \Gamma = \frac{\partial V_y}{\partial x}.$$

We search for the solution to (13) in the form

$$f_k = \sum_{l>1} f_l\exp(il\vartheta) + \text{c.c.}, \tag{14}$$

restricting ourselves to the terms with $l = 1, 2$. Then, we arrive at the equations

$$\left(1 + \frac{i\nu}{\omega_B}\right)f_1 - \frac{b}{2}f_2 = \beta,$$

$$\left(2 + \frac{i\nu}{\omega_B}\right)f_2 - \frac{b}{2}f_1 = -\gamma.$$

We solve these equations in the approximation $\dfrac{\nu}{\omega_B} \ll 1$, which corresponds to the case of strongly magnetized plasma. The result can be represented in the form

$$f_i = f_i^{(0)} + f_i^{(1)}, \quad i = 1, 2, \tag{15}$$

where superscripts (0) and (1) denote the terms independent of ν and proportional to ν, respectively. The functions $f_1^{(0)}$ and $f_2^{(1)}$ are

$$f_2^{(1)} = \frac{i\nu\gamma}{4\omega_B}\frac{1 + b^2/4}{(1 - b^2/8)^2} + \frac{b\beta}{4(1 - b^2/8)},$$

$$f_1^{(0)} = -\frac{b\gamma}{4(1 - b^2/8)}.$$

The remaining functions entering into (15), namely, $f_2^{(0)}$ and $f_1^{(1)}$, are not necessary for subsequent calculations.

According to (12), $\pi_{xy}(x)$ is related to $(\pi_{xy})_k$ by

$$\pi_{xy}(x) = \int\exp(ikx)(\pi_{xy})_k dk. \tag{16}$$

Using the formulas given above, we find

$$(\pi_{xy})_k = -\frac{\nu}{4\omega_B^2}nT(I_2\Gamma_k - 2ikI_1U_k), \tag{17}$$

where $U_k = -\dfrac{1}{2}ik\rho_i^2 I_1\Gamma_k$,

$$I_1 = \frac{1}{2n}\int\left(\frac{Mv_\perp^2}{2T}\right)^2\frac{F}{1 - b^2/8}d\mathbf{v}, \tag{18}$$

$$I_2 = \frac{1}{2n}\int\left(\frac{Mv_\perp^2}{2T}\right)^2\frac{1 + b^2/4}{(1 - b^2/8)^2}Fd\mathbf{v}. \tag{19}$$

Equations (16)–(19) determine the transverse viscosity in the model allowing for the two first terms of series (14). At the same time, in this model, the ratio between the ionic Larmor radius and the spatial scale of the velocity inhomogeneity characterized by parameter b is considered arbitrary. In this sense, the above equations describe the generalized viscosity. It is assumed that they are intended for studying localized perturbations. In this case, the integrands in (18), (19) have no poles (cf. [5]).

In correspondence with the above discussion, we use these equations in deriving simpler models for π_{xy} by expanding expressions (18), (19) in a series with respect to b^2. Restricting ourselves to the terms on an order up to ρ_i^4, we reduce (18), (19) to the form

$$I_1 = 1 + \frac{3}{4}\rho_i^2 k^2, \quad I_2 = 1 + 3\rho_i^2 k^2 + \frac{21}{4}\rho_i^4 k^4.$$

Then, from Eqs. (12), (17), expression (7) follows with $\nu_{\text{eff}} = \frac{\nu}{4}$, $c_L = 2$, and $d_L = \frac{15}{4}$. In this case, condition (9) is satisfied.

Thus, the kinetics qualitatively yields the same results as the Grad-type approach. This is a weighty argument in favor of the standpoint that the solutions of type (4)–(6) and (8) with $V_y(x) \longrightarrow$ const as $x \longrightarrow \infty$ are physical reality, whose description, however, is beyond the scope of the traditional transport theory [2].

In conclusion, we would like to note that the problem considered in this paper is important, in particular, from the viewpoint of magnetic islands in plasma immersed in a sheared magnetic field [5, 8]. In this case, the plasma inside the island separatrix plays the role of the quiescent conducting medium lying in the half-plane $x < 0$, while the region $x > 0$ is similar to the region outside the separatrix. The solution found by us with $E_x \longrightarrow$ const as $x \longrightarrow \infty$ corresponds to the case of magnetic islands with a localized velocity profile in tokamaks under standard conditions when far from an island, the gradient of the equilibrium radial electric field vanishes or is negligibly small (see [5] for details). At the same time, the solution with $E_x \sim x$ corresponds to the case of islands typical for so-called flows of Mach–Alfven type [8]: in this case, we assume the presence of a noticeable strongly inhomogeneous equilibrium radial electric field. Therefore, it is clear that the expressions for the hyperviscosity and generalized viscosity derived by us can be a base for following more complete analysis of magnetic-island dynamics.

ACKNOWLEDGMENTS

The authors are grateful to Drs. V.D. Pustovitov, A.I. Smolyakov, N.C. Nascimento, and R.M.O. Galvao for fruitful discussions stimulating this work.

This work was supported in part by the Council for Grants and State Support of Reading Scientific Schools by the President of the Russian Federation, project no. 00-15-96526, the Research Support Foundation of the State of Sáo Paulo (FAPESP), National Council of Scientific and Technological Development (CNPq), and Excellence Research Programs (PRONEX) RMOG 50/70 grant from the Ministry of Science and Technology, Brazil.

REFERENCES

1. I. E. Tamm, *Plasma Physics and Problems of Controlled Thermonuclear Reactions* (Izd. Akad. Nauk SSSR, Moscow, 1958), Vol. 1, pp. 3–19.
2. S. I. Braginskiĭ, in *Reviews of Plasma Physics*, Ed. by M. A. Leontovich (Gosatomizdat, Moscow, 1963; Consultants Bureau, New York, 1963), Vol. 1.
3. K. Zhang and C. A. Jones, Geophys. Res. Lett. **24**, 2869 (1997).
4. S. A. Smith and G. W. Hammett, Phys. Plasmas **4**, 978 (1997).
5. A. B. Mikhaĭlovskiĭ, V. D. Pustovitov, V. S. Tsypin, and A. I. Smolyakov, Phys. Plasmas **7**, 1204 (2000).
6. H. Grad, Commun. Pure Appl. Math. **2**, 331 (1949).
7. V. P. Lakhin, S. V. Makurin, A. B. Mikhaĭlovskiĭ, and O. G. Onishchenko, J. Plasma Phys. **38,** 387 (1987).
8. F. L. Waelbroeck and R. Fitzpatrick, Phys. Rev. Lett. **78**, 1703 (1997).

Doklady Physics, Vol. 46, No. 3, 2001, pp. 157–160. Translated from Doklady Akademii Nauk, Vol. 377, No. 1, 2001, pp. 34–37.

TECHNICAL PHYSICS

Synthesis of Optimum-Estimate Algorithms for Surface Electrophysical Parameters in the Case of Synchronous Fluctuations of Waves with Different Polarizations

V. K. Volosyuk*, V. F. Kravchenko, and Corresponding Member of the RAS V. I. Pustovoĭt*****

Received September 25, 2000

1. In papers [1–3], when solving inverse problems of optimum estimates for parameters of surfaces on the basis of electrodynamic models, fluctuations of scattered fields with different polarizations were assumed to be statistically independent. However, in many practical cases, in particular when sounding a small-scale surface whose asperities satisfy small-perturbation conditions [4], $h(\mathbf{r}) \ll \lambda$ and $|\nabla_\perp h| \ll 1$, the multiplicative fluctuations of a signal in reception channels for vertical and horizontal polarizations are equal and characterized by the factor

$$\dot{\alpha} = \int_D h(\mathbf{r}) \exp(j\mathbf{q}_\perp \mathbf{r}) d\mathbf{r}.$$

Here, $h(\mathbf{r})$ is the height of D-surface asperities; $\mathbf{r} \in D$; and $\mathbf{q}_\perp = (p, q)$ is the horizontal projection of the scattering vector, with p and q being its components.

We consider the following formulation of the problem. We assume that a surface segment is sounded by two oscillatory waves with vertical and horizontal polarizations which are of the same amplitude and initial phase. The experiment is repeated M times; i.e., ranging of M statistically independent surface segments is performed.

The observation equations for vertical and horizontal polarizations, respectively, are written out in the form

$$\begin{aligned} u_{\mathrm{vv}_m}(t) &= \mathrm{Re}\dot{\alpha}_m \dot{A}_{\mathrm{vv}}(\boldsymbol{\lambda}) \dot{S}_0(t) + n_{\mathrm{v}_m}(t), \\ u_{\mathrm{hh}_m}(t) &= \mathrm{Re}\dot{\alpha}_m \dot{A}_{\mathrm{hh}}(\boldsymbol{\lambda}) \dot{S}_0(t) + n_{\mathrm{h}_m}(t), \quad m = 1, 2, \ldots, M. \end{aligned} \tag{1}$$

Here, $\boldsymbol{\lambda} = \|\lambda_j\|$ is the set of surface electrophysical parameters (permittivity, slope angle, etc.) to be estimated; $\dot{\alpha}_m = |\dot{\alpha}_m| \exp(j\varphi_m)$; the noise n_{v_m} and n_{h_m} is considered to be white, i.e., $R_n(t_1, t_2) = \langle n(t_1) n(t_2) \rangle = \frac{N_0}{2} \delta(\tau)$; and the amplitude factors $\dot{A}_{\mathrm{vv}}$ and $\dot{A}_{\mathrm{hh}}$ are determined by an electrodynamic model for the surface.

What is required is the best estimation of electrophysical parameters $\boldsymbol{\lambda}$ or such statistical surface characteristics as the spectrum $W(\mathbf{q}_\perp)$, cross section σ^0, angular deflections $\dot{\gamma}'_{\mathrm{h/v}}$ of signals with different polarization, their relative phase shift, etc., [2].

2. We seek the optimum estimates for parameters $\boldsymbol{\lambda}$ within the framework of the maximum likelihood method.

The likelihood function for observation equations (1) has the form

$$\begin{aligned} p[\mathbf{u}/\boldsymbol{\lambda}, \dot{\boldsymbol{\alpha}}, \varphi] &= c \prod_{m=1}^{M} \exp\{\alpha_m Q_{\Sigma m}(\boldsymbol{\lambda}) \\ &\times \cos[\Phi_{\Sigma m}(\boldsymbol{\lambda}) + \varphi_m] - \alpha_m^2 \mu_\Sigma(\boldsymbol{\lambda})\}, \end{aligned} \tag{2}$$

where

$$\mathbf{u} = \{u_{\mathrm{vv}_m}, u_{\mathrm{hh}_m}\}, \quad \dot{\boldsymbol{\alpha}} = \{\dot{\alpha}_m\}, \quad \varphi = \{\varphi_m\},$$

$$\mu_\Sigma = \mu_{\mathrm{vv}} + \mu_{\mathrm{hh}}, \quad \dot{Q}_{\Sigma m} = \left|\dot{Q}_{\mathrm{vv}_m} + \dot{Q}_{\mathrm{hh}_m}\right|,$$

$$\Phi_{\Sigma m}(\boldsymbol{\lambda}) = \arg \dot{Q}_{\Sigma m},$$

$$Q_{km} = |\dot{Q}_{km}| = \sqrt{q_{km}^2(\boldsymbol{\lambda}) + q_{\perp km}^2(\boldsymbol{\lambda})},$$

$$\Phi_{km}(\boldsymbol{\lambda}) = \arctan\left\{\frac{q_{\perp km}(\boldsymbol{\lambda})}{q_{km}(\boldsymbol{\lambda})}\right\}, \quad \mu_k = |A_k|^2 \mu_0,$$

$$\mu_0 = \frac{\mathrm{E}}{N_0}, \quad \mathrm{E} = \frac{1}{2}\int_0^T |\dot{S}_0(t)|^2 dt,$$

* *Kharkov Aerospace University, Ukraine*
** *Institute of Radio Engineering and Electronics, Russian Academy of Sciences, ul. Mokhovaya 18, Moscow, 103907 Russia*
*** *Central Design Bureau of Unique Instrumentation, Russian Academy of Sciences, ul. Butlerova 15, Moscow, 117342 Russia*

1028-3358/01/4603-0157$21.00

$$\dot{S}_{vv(hh)}(t, \boldsymbol{\lambda}, \alpha_m, \varphi_m) = \dot{\alpha}_m \dot{A}_{vv(hh)}(\boldsymbol{\lambda}) \dot{S}_{0v(h)},$$

$$q_{km} = \frac{2}{N_0}\int_0^T u_{km} S_k(t, \boldsymbol{\lambda}) dt, \quad q_{\perp km} = \frac{2}{N_0}\int_0^T u_{km} S_{\perp k}(t, \boldsymbol{\lambda}) dt,$$

$$S_k(t, \boldsymbol{\lambda}) = \mathrm{Re}[\dot{A}_k(\lambda)\dot{S}_0(t)],$$
$$S_{\perp k}(t, \boldsymbol{\lambda}) = \mathrm{Im}[\dot{A}_k(\boldsymbol{\lambda})\dot{S}_0(t)],$$

and μ is the energy signal-to-noise ratio.

By averaging the likelihood function over the phases φ_m with uniform distribution and over the factor α_m distributed according to the Rayleigh law, we arrive at the formula

$$p[\mathbf{u}/\boldsymbol{\lambda}] = c[1 + \sigma_\alpha^2 \mu_\Sigma(\boldsymbol{\lambda})]^{-M} \exp\left\{\frac{\sigma_\alpha^2 \sum_{m=1}^{M} Q_{\Sigma m}^2(\boldsymbol{\lambda})}{4[1 + \sigma_\alpha^2 \mu_\Sigma(\boldsymbol{\lambda})]}\right\}, \quad (3)$$

where σ_α^2 is the parameter of the Rayleigh distribution.

From the condition $\frac{\partial \ln p[\mathbf{u}/\boldsymbol{\lambda}]}{\partial \boldsymbol{\lambda}_\nu} = 0$, we obtain the system of likelihood equations

$$-\frac{M\mu'_{\Sigma_{av}}}{1 + \mu_{\Sigma_{av}}} + \frac{(Q_{\Sigma\Sigma}^2)'(1 + \mu_{\Sigma_{av}}) - Q_{\Sigma\Sigma}^2 \mu'_{\Sigma_{av}}}{4(1 + \mu_{\Sigma_{av}})^2} = 0, \quad (4)$$

Here,

$$Q_{\Sigma\Sigma}^2 = \sigma_\alpha^2 \sum_{m=1}^{M} Q_{\Sigma_m}^2 = \sigma_\alpha^2 \sum_{m=1}^{M} \left|\dot{Q}_{vv_m} + \dot{Q}_{hh_m}\right|^2,$$
$$\mu_{\Sigma_{av}} = \sigma_\alpha^2 \mu_\Sigma = \sigma_\alpha^2 (|A_{vv}|^2 + |A_{hh}|^2)\mu_0. \quad (5)$$

Information on the complex-valued character of the factors $\dot{A}_{vv}(\boldsymbol{\lambda})$ and $\dot{A}_{hh}(\boldsymbol{\lambda})$ is lost as a result of the averaging over the phases φ_m. However, since the signals with different polarizations have identical fluctuations, information on the complex-valued character of the ratio

$$\dot{\gamma}_{h/v} = \frac{\dot{A}_{hh}(\boldsymbol{\lambda})}{\dot{A}_{vv}(\boldsymbol{\lambda})} = \gamma_{h/v} e^{j\varphi_{h/v}}$$

is retained in the likelihood functional obtained.

The estimates for the electrophysical and geometric parameters $\boldsymbol{\lambda}$ entering into dependences $\dot{A}_{vv}(\boldsymbol{\lambda})$ and $\dot{A}_{hh}(\boldsymbol{\lambda})$ can be obtained by solving the system of nonlinear equations

$$\hat{\varphi}_{h/v} = \arg\dot{\gamma}_{h/v}(\hat{\boldsymbol{\lambda}}) = \arg\left[\frac{\dot{A}_{hh}(\hat{\boldsymbol{\lambda}})}{\dot{A}_{vv}(\hat{\boldsymbol{\lambda}})}\right],$$

$$\hat{\gamma}_{h/v} = \left|\dot{\gamma}_{h/v}(\hat{\boldsymbol{\lambda}})\right| = \left|\frac{\dot{A}_{hh}(\hat{\boldsymbol{\lambda}})}{\dot{A}_{vv}(\hat{\boldsymbol{\lambda}})}\right|, \quad (6)$$

$$\hat{\sigma}_{vv}^0 = \hat{\sigma}_{vv}^0(\hat{\boldsymbol{\lambda}}) = \sigma_\alpha^2 \left|\dot{A}_{vv}(\hat{\boldsymbol{\lambda}})\right|^2, \ \mu_0 = W_1(\mathbf{q}_\perp)\left|\dot{A}_{vv}(\hat{\boldsymbol{\lambda}})\right|^2.$$

Here, $W_1(\mathbf{q}_1) = \frac{k^4}{\pi^2} W(\mathbf{q}_\perp)$. In the right-hand side of expressions (6), there are known analytic dependences relating the left-hand sides of the equations to the parameters $\boldsymbol{\lambda}$ to be estimated. The left-hand sides of these equations also characterize the surface and must also be estimated.

We find the solution to likelihood equations (4) for the parameters $\boldsymbol{\rho} = (\varphi_{h/v}, \sigma_{vv}^0, \gamma_{h/v})$.

Substituting expressions (5) into formula (3), we arrive at the likelihood functional for the parameters $\gamma_{h/v}$ and σ_{vv}^0:

$$p[\mathbf{u}/\gamma_{h/v}, \sigma_{vv}^0] = c[1 + \sigma_{vv}^0 D(1 + \gamma_{h/v}^2)\mu_0]^{-M} \times \exp\left\{\frac{\sigma_{vv}^0 D \sum_{m=1}^{M} Q_{0vv_m}^2 \left|1 + \gamma_{h/v} e^{j\varphi_{h/v}} \dot{Q}_{h/v_m}\right|^2}{4[1 + \sigma_{vv}^0 D(1 + \gamma_{h/v}^2)\mu_0]}\right\}.$$

From the condition

$$\left.\frac{\partial^2 Q_{0_{vv}}^2}{\partial \varphi_{h/v}}\right|_{\substack{\gamma_{h/v} = \hat{\gamma}_{h/v} \\ \sigma_{vv}^0 = \hat{\sigma}_{vv}^0 \\ \varphi_{h/v} = \hat{\varphi}_{h/v}}} = 0,$$

we obtain solutions to the equations for the estimating phase $\hat{\varphi}_{h/v}$ and for the quantities $\hat{\sigma}_{vv}^0$ and $\hat{\gamma}_{h/v}$. Namely,

$$\hat{\varphi}_{h/v} = -\arg \sum_{m=1}^{M} Q_{0vv_m}^2 \dot{Q}_{(h/v)_m}$$
$$= -\arg \sum_{m=1}^{M} \left|\dot{Q}_{0vv_m} \dot{Q}_{0hh_m}\right|^2 E^{j\varphi_{(h/v)_m}},$$

with

$$\varphi_{(h/v)_m} = \arg \dot{Q}_{(h/v_m)} = \arg\left(\frac{\dot{Q}_{0hh_m}}{\dot{Q}_{0vv_m}}\right);$$

$$\hat{\sigma}^0_{vv} = \frac{\sum_{m=1}^{M} Q^2_{0vv_m}\left|1+\gamma_{h/v}e^{j\gamma_{h/v}}\dot{Q}_{(h/v)_m}\right|^2}{4MD(1+\hat{\gamma}^2_{h/v})^2\mu_0^2} - \frac{1}{D(1+\hat{\gamma}^2_{h/v})\mu_0};$$

and

$$\hat{\gamma}_{h/v} = \frac{\sum_{m=1}^{M} Q^2_{0vv}(Q^2_{(h/v)_m}-1)}{2\left|\sum_{m=1}^{M} Q^2_{0vv_m}\dot{Q}_{(h/v)_m}\right|} + \frac{\sqrt{\left[\sum_{m=1}^{M} Q^2_{0vv_m}(Q^2_{(h/v)_m}-1)\right]^2 + 4\left|\sum_{m=1}^{M} Q^2_{0vv_m}\dot{Q}_{(h/v)_m}\right|^2}}{2\left|\sum_{m=1}^{M} Q^2_{0vv_m}\dot{Q}_{(h/v)_m}\right|}.$$

Then, the effective scattering cross section for the horizontal polarization is

$$\hat{\sigma}^0_{hh} = \hat{\gamma}^2_{h/v}\hat{\sigma}^0_{vv}.$$

3. We find the limiting measurement errors for the parameters $\gamma_{h/v}$, $\varphi_{h/v}$, and σ^0_{vv} by inverting the Fisher matrix

$$\mathbf{B}_{\boldsymbol{\rho}} = -\left\langle \frac{\partial^2 \ln P[\mathbf{u}/\boldsymbol{\rho}]}{\partial\rho_\mu \partial\rho_\nu}\right\rangle\Bigg|_{\boldsymbol{\rho}=\hat{\boldsymbol{\rho}}}.$$

Namely,

$$\sigma^2_\varphi = \frac{1}{B_{\varphi\varphi}} = \frac{(1+\mu_{\Sigma_{av}})(1+\gamma^2_{h/v})^2}{2M\gamma^2_{h/v}/\mu^2_{\Sigma_{cp}}},$$

$$\sigma^2_{\sigma^0} = \frac{B_{\gamma\gamma}}{\Delta} = \frac{(1+2\gamma^2_{h/v}+\mu_{\Sigma_{av}})(1+\mu_{\Sigma_{av}})(\sigma^0_{vv})^2}{M\mu^2_{\Sigma_{av}}},$$

$$\sigma^2_\gamma = \frac{B_{\sigma^0\sigma^0}}{\Delta} = \frac{(1+\mu_{\Sigma_{av}})(1+\gamma^2_{h/v})^2}{2M\mu^2_{\Sigma_{av}}}, \quad (7)$$

$$\sigma^2_{\gamma\sigma^0} = \sigma^2_{\sigma^0\gamma} = -\frac{B_{\gamma\sigma^0}}{\Delta} = -\frac{\gamma_{h/v}\sigma^0_{vv}(1+\mu_{\Sigma_{av}})}{M\mu^2_{\Sigma_{av}}}.$$

Here, $\mathbf{B}$ is the Fisher information matrix and $\Delta = B_{\sigma^0\sigma^0}B_{\gamma\gamma} - (B_{\gamma\sigma^0})^2 = \frac{2M^2\mu^4_{\Sigma_{av}}}{(1+\mu^3_{\Sigma_{av}})(\sigma^0_{vv})^2(1+\gamma^2_{h/v})^2}$ is its determinant.

After the parameters $\boldsymbol{\rho} = (\varphi_{h/v}, \sigma^0_{vv}, \gamma_{h/v})$ have been found, the electrophysical parameters $\boldsymbol{\lambda}$ (for example, the real and imaginary parts of the complex-valued permittivity, $\mathrm{Re}\dot{\varepsilon}$ and $\mathrm{Im}\dot{\varepsilon}$, respectively) and the spectrum $W(\mathbf{q}_\perp)$ can be determined by solving the system of nonlinear equations (6).

The limiting measurement errors for the parameters $\boldsymbol{\lambda}$ and function $W(\mathbf{q}_\perp)$ are characterized by the diagonal elements of a matrix inverse to the Fisher information matrix:

$$\mathbf{B}_{\boldsymbol{\lambda}} = -\left\langle \frac{\partial^2 \ln P(\mathbf{u}/\boldsymbol{\lambda})}{\partial\lambda_i\partial\lambda_j}\right\rangle\Bigg|_{\lambda=\hat{\lambda}}.$$

There exists a functional relation $\boldsymbol{\rho} = \boldsymbol{\rho}(\boldsymbol{\lambda})$ with $\boldsymbol{\rho} = (\varphi_{h/v}, \gamma_{h/v}, \sigma^0_{vv})$ between the parameters $\gamma_{h/v}$, $\varphi_{h/v}$, σ^0_{vv} and $\boldsymbol{\lambda}$ which is described by the system of equations (6). Therefore, the first derivative of the logarithm of the likelihood function can be written in the following form:

$$\frac{\partial \ln P[\mathbf{u}/\boldsymbol{\rho}(\boldsymbol{\lambda})]}{\partial\lambda_i} = \frac{\partial \ln P[\mathbf{u}/\boldsymbol{\rho}]}{\partial\rho_\mu}\frac{\partial\rho_k}{\partial\lambda_i}, \quad \mu = 1, 2, \ldots, N.$$

Here, N is the dimension of the vector $\boldsymbol{\rho}$.

The dimensions of the vectors $\boldsymbol{\rho}$ and $\boldsymbol{\lambda}$ are taken as coincident. Then,

$$\mathbf{B}_{\boldsymbol{\lambda}} = \mathbf{P}^{\mathrm{T}}\mathbf{B}_{\boldsymbol{\rho}}\mathbf{P},$$

where $\mathbf{P} = \{\rho'_{\mu_i}\} = \left\{\frac{\partial\rho_\mu}{\partial\lambda_i}\right\}$.

The inverse information matrix takes the form

$$\mathbf{B}^{-1}_{\boldsymbol{\lambda}} = \mathbf{P}^{-1}\mathbf{B}^{-1}_{\boldsymbol{\rho}}(\mathbf{P}^{-1})^{\mathrm{T}}.$$

Here, the matrix $\mathbf{P}^{-1}$ has the following elements:

$$\beta_{11} = \frac{\mathrm{Im}\dot{\gamma}'_{h/v}\dot{\gamma}^*_{h/v}}{|\dot{\gamma}'_{h/v}|^2}, \quad \beta_{12} = \frac{\mathrm{Re}\dot{\gamma}'_{h/v}\dot{\gamma}^*_{h/v}}{|\dot{\gamma}_{h/v}||\dot{\gamma}'_{h/v}|^2},$$

$$\beta_{13} = \beta_{23} = 0,$$

$$\beta_{21} = \frac{\mathrm{Re}\dot{\gamma}'_{h/v}\dot{\gamma}^*_{h/v}}{|\dot{\gamma}'_{h/v}|^2}, \quad \beta_{22} = -\frac{\mathrm{Im}\dot{\gamma}'_{h/v}\dot{\gamma}^*_{h/v}}{|\dot{\gamma}_{h/v}||\dot{\gamma}'_{h/v}|^2},$$

$$\beta_{31} = \frac{2\pi^2 W_1(\mathbf{q}_\perp)}{k^4|\dot{A}_{vv}|^2|\dot{\gamma}'_{h/v}|^2}\mathrm{Im}(\dot{A}'_{vv})^*\dot{A}_{vv}\dot{\gamma}'_{h/v}\dot{\gamma}^*_{h/v},$$

$$\beta_{32} = \frac{2\pi^2 W_1(\mathbf{q}_\perp)}{k^4|\dot{A}_{vv}|^2|\dot{\gamma}'_{h/v}|^2|\dot{\gamma}_{h/v}|}\mathrm{Re}(\dot{A}'_{vv})^*\dot{A}_{vv}\dot{\gamma}'_{h/v}\dot{\gamma}^*_{h/v},$$

$$\beta_{33} = \frac{\pi^2}{k^4}|\dot{A}_{vv}|^{-2}.$$

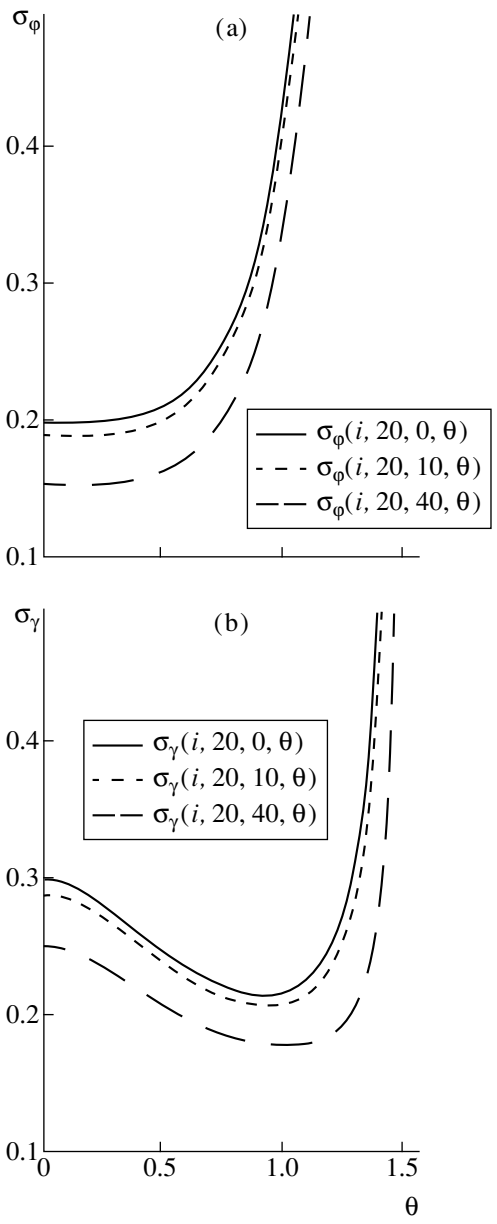

Fig. 1. Measurement errors (a) σ_φ and (b) σ_γ for the parameters $\varphi_{h/v}$ and $\gamma_{h/v}$, respectively, as functions of the angle of incidence θ for $\varepsilon_1 = 20$. Solid, dashed, and broken lines correspond to $\varepsilon_2 = 0$, 10, and 40, respectively.

Analysis of elements (7) of the matrix $\mathbf{B}_\rho^{-1}$ and elements of the matrix $\mathbf{B}_\lambda^{-1}$ make it possible, first, to evaluate the possibility of solving the system of nonlinear equations for the parameters $\boldsymbol{\rho}$ and $\boldsymbol{\lambda}$ at a given set of conditions. Second, it provides a way of finding the conditions under which the measurement errors would be minimal. In particular, for radio waves, the values of the angles of incidence on a surface can be found for which an acceptable or highest accuracy of surface-parameter measurements can be provided.

Figures 1a and 1b show the measurement errors $\sigma_{\varphi_{h/v}}$ and $\sigma_{\gamma_{h/v}}$ for the parameters $\varphi_{h/v}$ and $\gamma_{h/v}$, respectively, as functions of the angle of incidence θ for $\varepsilon_1 = 20$ and $\varepsilon_2 = (0, 10, 40)$.

It is evident that the measurement error $\sigma_{\varphi_{h/v}}$ for the parameter $\varphi_{h/v}$ sharply increases with the ranging angle θ close to 70° but decreases with increasing ε_2. The error $\sigma_{\gamma_{h/v}}$ decreases with increasing the angle θ from 0° to 70° but sharply tends to infinity at the angles of incidence θ close to the slip angle. An increase in the imaginary part ε_2 of the complex-valued permittivity results in a small decrease in the error $\sigma_{\gamma_{h/v}}$.

4. Thus, taking into consideration that the amplitude and phase functions in reception channels for different polarizations are synchronous, we can employ not only information inherent in the moduli of the complex-valued amplitudes observed for waves with different polarizations but also information inherent in phase differences for these waves. This makes it possible to estimate complex parameters of the surface, i.e., both their real and imaginary parts, as well as real parameters and statistical surface characteristics.

REFERENCES

1. A. A. Goncharenko, V. F. Kravchenko, and V. I. Ponomarev, *Remote Probing of Inhomogeneous Media* (Mashinostroenie, Moscow, 1991).
2. V. K. Volosyuk, V. F. Kravchenko, and V. I. Ponomarev, Dokl. Akad. Nauk SSSR **319**, 1120 (1991) [Sov. Phys. Dokl. **36**, 571 (1991)].
3. V. K. Volosyuk and V. F. Kravchenko, Izv. Vyssh. Uchebn. Zaved., Radioélektron. **34** (9), 84 (1991).
4. A. Ishimaru, *Wave Propagation and Scattering in Random Media* (Academic, New York, 1978; Mir, Moscow, 1981), Vol. 2.

Translated by V. Tsarev

Doklady Physics, Vol. 46, No. 3, 2001, pp. 161–162. Translated from Doklady Akademii Nauk, Vol. 377, No. 1, 2001, pp. 38–39.

TECHNICAL PHYSICS

Effect of Activators Evolving Hydrogen Fluoride on Formation of Protective Diffusion Coatings

Corresponding Member of the RAS V. I. Kostikov*, Yu. S. Nechaev, and G. Ya. Kul'ga***

Received September 5, 2000

In various technological conditions of forming protective diffusion coatings on products made of high-melting metals and alloys, diffusion transfer to a metal of saturating elements through the protective coating being formed is a critical stage of the entire process [1]. Therefore, to reduce the time-temperature parameters of the process, acceleration of saturating-element diffusion to the protective coating needs to be provided.

As is shown below, this is achieved by using activating species evolving gaseous hydrogen fluoride (HF) in amounts when HF predominantly affects the boundary grains of the protective coatings being formed and causes an acceleration of the diffusion of saturating elements in them.

For depositing protective diffusion coatings on products made of high-melting metals and alloys [1], equipment and procedures were used which were characterized by introducing activators (e.g., moistened aluminum trifluoride AlF_3 or acid potassium bifluoride KHF_2) into the active volume of a furnace. The amounts of the activators introduced provide a partial HF pressure in the furnace on the order of approximately 10^{-1} bar.

Phase X-ray analysis was used for determination of the coating composition. The coating thickness was determined by optical-microscopy and gravimetry methods; the microstructure was studied by the method of scanning electron-microscopy.

Boriding of Nb and Mo samples was performed at 1073–1373 K for a 2-hour holding. In this case, formation and growth of boride layers (NbB_2 and MoB) with a thickness of several tens of microns occurred. A parabolic time dependence of the boride-layer thickness was observed (at holding for 1 to 5 h), which is characteristic of the case when the total process is limited by diffusion of boron atoms through a boride layer [1]. On the basis of this procedure, the diffusion coefficients D, the entropy factor D_0, and the diffusion-activation energy Q for boron atoms in boride layers were determined (Table 1).

The results obtained show that the employment of an activator (moistened AlF_3) for boriding Nb results in elevation of the effective coefficients of boron-atom diffusion in boride layers by an order of magnitude. This occurs mainly due to the reduction of effective activation energies. Similar results were also obtained for molybdenum.

The effect of a KHF_2 activator on the kinetics of nitriding iodide Ti and Zr samples was studied for holding (from 1 to 5 h) at 870–1070 K and a nitrogen pressure of 1.2 bar. In the presence of the activator, we observed sharp intensification of the nitride layer (TiN and ZrN) formation, the thickness of the layer attaining several hundreds of microns. The kinetics of the nitride-layer growth corresponded to a parabolic dependence. Thus, the characteristics of the diffusion of nitrogen atoms in nitride layers were measured (Table 2).

Table 1. Niobium boriding

T, K	Saturation medium	D, 10^{-11} cm^2 s^{-1}	D_0, cm^2 s^{-1}	Q, kJ mol^{-1}
1173	Boron carbide (B_4C) and carbon	0.7	150	300
1223		2.3		
1273		7.3		
1323		21		
1373		58		
1073	Boron carbide and carbon with AlF_3 activator	0.5	230	280
1123		2.2		
1173		7.8		
1223		25		
1273		75		
1323		200		
1373		510		

* *State Unitary Enterprise "NIIgrafit," Élektrodnaya ul. 2, Moscow, 111524 Russia*

** *Institute of Metal Science and Metal Physics, State Research Center "Bardin Central Research Institute of Ferrous Metals," Vtoraya Baumanskaya 9/23, Moscow, 107005 Russia*

1028-3358/01/4603-0161$21.00

Table 2. Titanium nitriding* (P_{N_2} = 1.2 bar)

Activator	*T*, K	*D*, $cm^2\ s^{-1}$	D_0, $cm^2\ s^{-1}$	*Q*, kJ mol^{-1}
Without activator	870	8.8×10^{-13}	8.5×10^{-5}	133 ± 6
	970	5.8×10^{-12}		
	1070	2.7×10^{-11}		
KHF_2	870	5.8×10^{-8}	6.1×10^{-4}	67 ± 7
	920	9.6×10^{-8}		
	970	1.5×10^{-7}		

* Similar results were also obtained for zirconium.

The diffusion characteristics obtained in the process of nitriding Ti and Zr with the KHF_2 activator at 870–970 K correspond to the characteristics of nitrogen surface diffusion in nitride layers [2], which seem to proceed predominantly along microcracks. Diffusion characteristics for nitriding without an activator at 870–1070 K (Table 2) correspond to characteristics for nitrogen diffusion predominantly along grain boundaries in nitride layers [2]. This can be caused by both the low temperatures employed in the process and the fine-grained structure of the nitride layers being formed.

Grinding of the microstructure and the appearance of microcracks at grain boundaries in nitride layers when nitriding in the presence of an activator are likely caused by local deformations. These occur owing to the energy and excess volume of topochemical reactions associated with the formation of secondary intermetallic compounds (fluorides, etc.) in domains of cosegregations of hydrogen and fluorine at intergrain boundaries. Nitriding Ti and Zr in the presence of an activator occurs at considerably lower time-temperature parameters. In this case, the ratio of the nitride-layer thickness to that of the nitrogen solid-solution layer in a metal increases (by two orders of magnitude) due to an increase (by four orders of magnitude) in the nitrogen effective diffusion coefficient in the nitride layer.

Employment of the KHF_2 activator for oxidation of Ti and Zr, as well as Zr + 1.0% Nb and Zr + 2.5% Nb alloys, also results in a sharp intensification of the entire nitriding process and in a reduction in the time-temperature parameters of the entire process (due to the acceleration of oxygen diffusion in oxide coatings).

In the process of carbidizing treatment of titanium powder at temperatures of 673–1173 K (2-hour holding), formation of the carbide layer in the absence of an activator and in the presence of the KHF_2 activator was studied at 1073–1173 K and 773–1173 K, respectively. It was established that the activator reduced the lowest temperature of the protective-coating formation by 300 K. A similar behavior was also observed in the case of carbidizing a tungsten powder, as well as while obtaining protective coatings (carbide layers) on tantalum plates.

The scientific importance of the results obtained lies in the fact that they introduce significant changes to the existing concept on the interaction mechanism of transition high-melting metals and alloys (Nb, Mo, Zr, Ti, Ta, and W) with metalloids of the III–VI groups of the periodic system of elements (boron, carbon, nitrogen, and oxygen) in the presence of activators. Among these activators, species evolving gaseous HF occupy a specific place. The high efficiency and versatility of the HF action are caused by the extremely high difference in the electronegative properties of fluorine and hydrogen.

The practical importance of these studies consists in the fact that, on this basis, a possibility appears to significantly change the formula of activating additives. Novel technologies for obtaining wear-resistant, heat-protective, and antioxidant coatings on steels, nonferrous and rare metals, and alloys may also be suggested.

REFERENCES

1. G. V. Samsonov and A. P. Épin, *Refractory Coatings* (Metallurgiya, Moscow, 1973).
2. R. B. Kotel'nikov, S. N. Bashlykov, Z. G. Galiakbarov, and A. I. Kashtanov, *Highly Refractory Elements and Their Compounds: Handbook* (Metallurgiya, Moscow, 1969).

Translated by T. Galkina

Doklady Physics, Vol. 46, No. 3, 2001, pp. 163–165. Translated from Doklady Akademii Nauk, Vol. 377, No. 1, 2001, pp. 40–43.

TECHNICAL PHYSICS

Electrodynamic Properties of Simple Bodies Made of Materials with Negative Permeability and Negative Permittivity

Corresponding Member of the RAS A. N. Lagarkov and V. N. Kisel

Received November 1, 2000

Loss-free propagation of an electromagnetic wave in a medium with negative permeability μ and negative permittivity ε) was first considered by V.G. Veselago in 1967 [1]. The possible creation of such materials was repeatedly discussed in the literature both prior to (see [2–4]) and after (see [5–10]) his publication. In particular, Lagarkov and Sarychev [7] derived formulas necessary for developing materials with elongated conducting inclusions (sticks) having $\varepsilon < 0$. Later, Lagarkov *et al.* [10] experimentally studied materials with negative μ and ε and derived corresponding formulas. In all these studies, the attempts to design such materials stemmed from various reasons and, therefore, publication [1] was ignored. It seems that the first materials purposefully synthesized to verify a number of effects predicted in [1] were obtained by J.B. Pendry (see [11, and references therein]). Today, it is possible to state that we possess both technologies for manufacturing such materials and computational methods for predicting and designing materials having negative real parts of permittivity ε' and permeability μ'. In other words, it has become possible to predict such materials also in the case of dissipative media where the equations $\varepsilon = \varepsilon' - i\varepsilon''$ and $\mu = \mu' - i\mu''$ are applicable, the time dependence being chosen as $e^{i\omega t}$.

Below, we describe our study of the interaction of an electromagnetic wave with bodies of a relatively simple shape, which either include such materials or are coated with them. In particular, we consider cylindrical structures, including inhomogeneous structures and those with arbitrary cross sections. We present here, at first glance, the rather surprising field distributions and electrodynamic properties of certain models studied.

The problems were solved by the known methods [12]. We used the technique of matching fields at a half-space interface in the calculation of the Fresnel coefficients. The body excitation was analyzed with the aid of eigenfunctions and volume integral equations. The use of different approaches provided a test of various computational programs, which is of great importance for reliable interpretation of the physical effects under consideration.

The results of our numerical calculations confirm theoretical conclusions [1] on materials with negative permittivity and permeability. In particular, an incident wave refracted by a planar interface propagates along the direction symmetric (with respect to the surface normal) to the propagation direction of the refracted ray in a conventional medium. The phase incursion along the refracted ray is positive, in full accordance with the negative refractive index and the phase velocity. We believe that studying other structures should reveal new specific properties.

We now proceed to interfaces of a more complicated geometry.

Let a plane wave be incident onto a circular dielectric cylinder, as depicted in Fig. 1 but having no internal conducting rod. The effect of field concentration ("focusing") well-known for materials with positive μ' and ε' also arises for negative values of μ' and ε'. However, unlike the usual location of the focal point behind the irradiated surface, in this case, the focal point is located in the front part of the cross section (points F_2

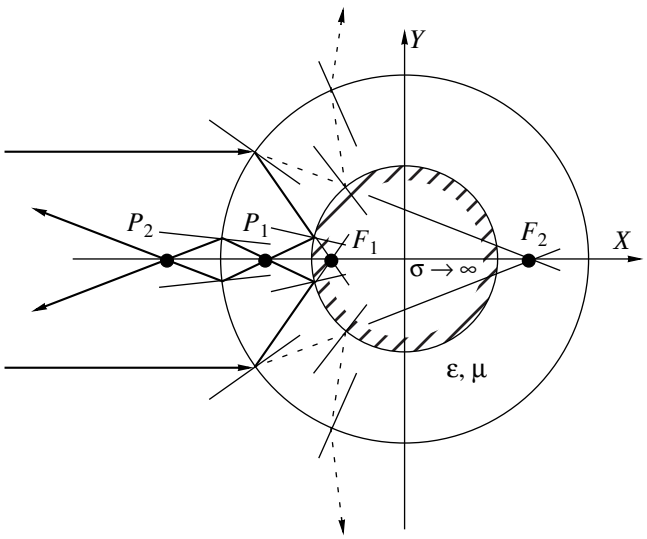

Fig. 1. Ray diagrams for a circular cylinder.

Institute for Theoretical and Applied Electrodynamics,
Joint Institute of High Temperatures,
Russian Academy of Sciences,
Izhorskaya ul. 13/19, Moscow, 127412 Russia

1028-3358/01/4603-0163$21.00

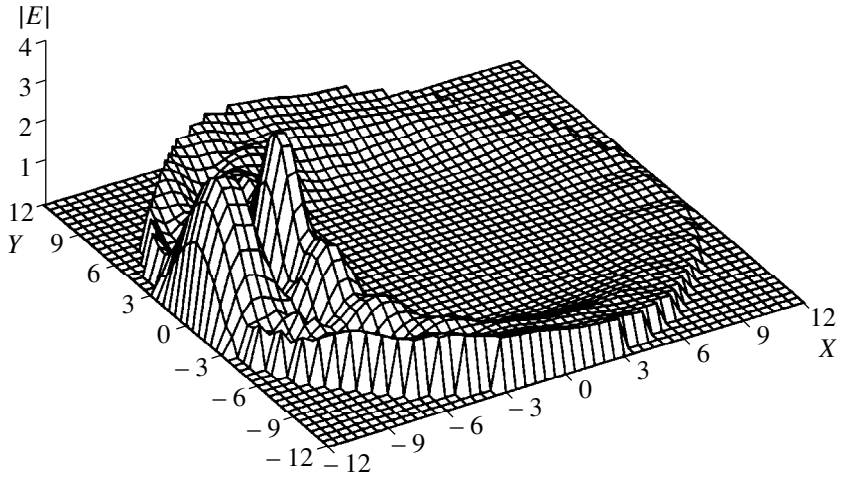

Fig. 2. Field distribution in the transverse cross section of a cylinder with coating and nearby it.

and F_1, respectively). Moreover, the field amplitude at point F_1 can exceed the amplitude at point F_2 because of the shorter path of the corresponding ray and, correspondingly, lower attenuation due to the energy loss always characteristic for dissipative media. This feature allows more efficient field focusing in media with a negative refractive index. We would like to mention that conventional focusing is widely used in reflectors of the Luneberg-lens type [13]. A reflector made of a material with a negative refractive index can have a number of technological and structural advantages. In this case, the reflecting surface does not have the shape of an encircling band as in a Luneberg lens, but is a core in the shape of a metallic conducting cylinder or a sphere (in the three-dimensional case). The core diameter should be chosen in such a manner that the focal point P_1 lies in close vicinity to the conductor (Fig. 1). Obviously, the optimum position of point P_1 in the two-dimensional case also depends on the wave polarization.

Another characteristic feature of such a structure is the existence of a second focal point P_2 lying outside the cylinder (Fig. 1). The dashed lines in Fig. 1 show the ray diagram characteristic of a conventional coating with a positive refractive index. The existence of two field-concentration points is confirmed by the calculations of field amplitudes in the coating bulk and in the medium adjacent to the cylinder. These calculations were performed for *E*-polarized waves (the intensity vector of the electric field being parallel to the cylinder axis), a radius of the internal metal cylinder $kR = 6.0$; a coating thickness $kD = 4.0$; $k = \frac{2\pi}{\lambda}$, where λ is the wavelength in the free space, $\varepsilon = -1.4 - i \times 0.01$; and $\mu = -1.3 - i \times 0.01$. The field distribution (calculated in the Cartesian coordinates) in the transverse cross section is shown in Fig. 2. It should be emphasized that, in accordance with the reciprocity principle, the field source can be placed at point P_2, and then, in accordance with the above ray diagram, we can expect the appearance of directional radiation. The existence of this effect was confirmed by a computational experiment in which the above structure was excited by a current-carrying filament located parallel to the cylinder axis at point P_2 (the distance between the filament and the cylinder axis is $kL = 10.4$). The obtained (not normalized) directivity patterns for three structures with the same geometric dimensions indicated above but having different electrodynamic parameters of the material are shown in Fig. 3. Curve *1* is obtained at $\mu = -1.3 - i \times 0.01$ and $\varepsilon = -1.4 - i \times 0.01$; curve *2*, at $\mu = 1.3 - i \times 0.01$ and $\varepsilon = 1.4 - i \times 0.01$; and curve *3*, at $\mu = 1$ and $\varepsilon = 1$ (i.e., for a cylinder without coating). It is clearly seen that at a negative refractive index (curve *1*), a lobe characteristic of the directional antennas is actually formed. Thus, the reflecting convex surface coated with a layer of a material having a negative refractive index behaves as an analogue of a focusing mirror. In order to

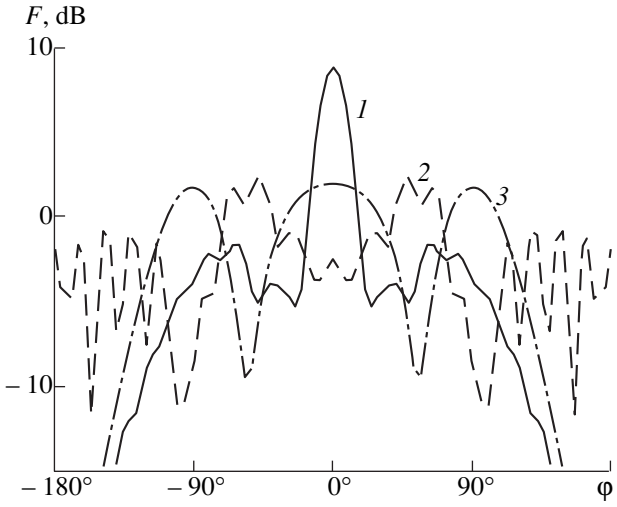

Fig. 3. Directivity patterns for a system including filament with a current and cylinder with a coating.

estimate the effective opening surface (the aperture) of the radiating system, we compared calculated results with the directivity pattern for a cophase strip of the surface electric current. The main lobes of the directivity pattern with an aperture of width $kD = 16.0$ and a uniform current distribution turned out to be almost coincident with those of the structure under consideration. The levels of the first side lobes are also close. Thus, the equivalent aperture size is rather large (equal to the average of the internal and external diameters of the dielectric shell). We can readily explain a relatively high level of side-lobe radiation at the observation angles 45° to 120° (it is formed by the rays indicated by dashed lines in Fig. 1). Obviously, in order to reduce the side-loop radiation and, thus, to increase the antenna efficiency, we should improve the matching between the coating and the outer medium, i.e., increase the transmission coefficient and reduce the reflection coefficient of the wave at the interface. This can be performed, e.g., by application of an additional coating or by making use of a coating with radius-dependent properties (e.g., gradient coating). In this case, the basic focusing element (the circular cylinder) remains an axisymmetric structure, which allows for creation of multibeam or omnidirectional antennas with several radiators or receivers and a common focusing element. It would also be convenient to use such a reflector for designing conformal antenna systems under rigorous constraints for the shape (e.g., only convex) of the reflecting surface.

We should like to emphasize the possible use of materials with a negative refractive index as electromagnetic-wave absorbers. Figure 4 illustrates the calculated bistatic for the effective scattering surface patterns of the above cylinder with different coatings (the angle $\varphi = 180°$ corresponds to the backscattering direction). Curve *1* corresponds to the coating parameters $\mu = -1 - i \times 0.6$ and $\varepsilon = -1 - i \times 1$; curve *2*, to the formal sign reversal for the real parts $\mu = 1 - i \times 0.6$ and $\varepsilon = 1 - i \times 1$. We believe that the first material can be actually obtained, while the development of the second material with the desired parameters is associated with insurmountable difficulties. Curve *3* is calculated for the coating made of a radiation-absorbing foamglass-based material with parameters $\mu = 1$ and $\varepsilon \approx 1 - i \times 0.6$, which is characterized by rather good matching to the free space. And, finally, curve *4* shows scattering from an uncoated cylinder. It is seen that in this case, the use of an absorber based on a material with a negative refractive index is much more advantageous, even when compared to a hypothetical conventional-type absorber. Qualitatively similar curves were also obtained for twice thinner coatings ($kD = 2.0$), i.e., for the case in which the absorber-metal interface produces a stronger effect on the field formation.

Thus, even a few examples of the calculations performed for rather simple structures show that the specific characteristics of the materials with negative μ' and ε' can be advantageous for various practical applications.

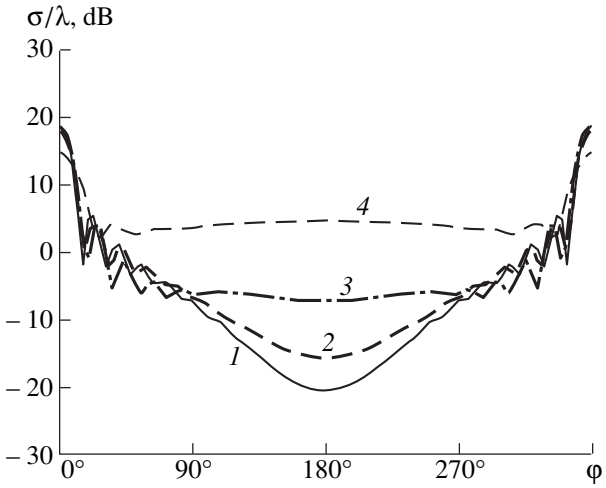

Fig. 4. Scattering patterns for a circular cylinder with a coating.

ACKNOWLEDGMENTS

The authors are grateful to A.I. Fedorenko for valuable remarks and fruitful discussion of the results.

The work was supported in part by the Russian Foundation for Basic Research, project nos. 99-02-16564 and 00-15-96570.

REFERENCES

1. V. G. Veselago, Usp. Fiz. Nauk **92**, 517 (1967) [Sov. Phys. Usp. **10**, 509 (1968)].
2. S. A. Schelkunoff and H. T. Friis, *Antennas: Theory and Practice* (Wiley, New York, 1952).
3. S. B. Cohn, J. Appl. Phys. **22**, 628 (1951).
4. W. E. Kock, Proc. IRE **34**, 828 (1946).
5. A. N. Lagarkov, A. K. Sarychev, and A. P. Vinogradov, Pis'ma Zh. Éksp. Teor. Fiz. **40**, 296 (1984) [JETP Lett. **40**, 1083 (1984)].
6. A. N. Lagarkov, A. K. Sarychev, Y. R. Smychkovich, and A. P. Vinogradov, J. Electromag. Waves Appl. **6**, 1159 (1992).
7. A. N. Lagarkov and A. K. Sarychev, Phys. Rev. B **53**, 6318 (1996).
8. M. V. Kostin and V. V. Shevchenko, Radiotekh. Élektron., No. 11, 1652 (1992).
9. Yu. N. Kazantzev *et al.*, Radiotekh. Élektron., No. 10, 1652 (1994).
10. A. N. Lagarkov *et al.*, Electromagnetics **17**, 213 (1997).
11. J. B. Pendry *et al.*, IEEE Trans. Microwave Theory Tech. **47**, 2075 (1999).
12. G. T. Markov and E. N. Vasil'ev, *Mathematical Methods of Applied Electrodynamics* (Sov. Radio, Moscow, 1970).
13. V. O. Kobak, *Radiolocation Reflectors* (Sov. Radio, Moscow, 1975).

Translated by L. Man

Doklady Physics, Vol. 46, No. 3, 2001, pp. 166–172. Translated from Doklady Akademii Nauk, Vol. 377, No. 2, 2001, pp. 183–189.

TECHNICAL PHYSICS

New Constructions of Weight Windows Based on Atomic Functions in Problems of Speech-Signal Processing

V. F. Kravchenko*, M. A. Basarab,**
Corresponding Member of the RAS V. I. Pustovoĭt*, and H. Pérez-Meana******

Received November 21, 2000

INTRODUCTION

Short-term spectral analysis is a principal method of speech-signal processing [1]. It is a basis for many systems of speech recognition, spectrographs, and vocoders. In turn, short-term spectral analysis is based on the short-term discrete Fourier transform for a speech segment weighted by a special window. Window functions are used for determining vocalized and fricative segments of a speech, its homomorphic processing and linear prediction. A number of weight-window constructions adapted for practical implementations are known. Currently, a new class of windows based on atomic functions (AF) is widely employed in solving problems of signal and image processing [2–9]. In this paper, the implementation of atomic functions for problems of speech-signal processing is considered for the first time.

PROPERTIES OF ATOMIC FUNCTIONS

Atomic functions are finite solutions to functional-differential equations of the form

$$Ly(x) = \sum_{m=1}^{M} c_m y(ax - b_m), \qquad (1)$$

where $|a| > 1$; $L = \frac{d^n}{dx^n} + a_1\frac{d^{n-1}}{dx^{n-1}} + \ldots + a_n$ is the linear differential operator with constant coefficients. The Fourier transform of atomic functions satisfies the following functional equation:

$$P(pa^{-1})Y(p) = T(pa^{-1})Y(pa^{-1}).$$

Here, $P(pa^{-1})$, $T(pa^{-1})$ are algebraic and trigonometric polynomials, respectively. The explicit expression for the Fourier transform of an AF is of the form

$$Y(p) = \prod_{k=1}^{\infty}\frac{T(pa^{-k})}{P(pa^{-k})}.$$

The AF are infinite convolutions of splines with Fourier transforms of the form $\frac{T(pa^{-k})}{P(pa^{-k})}$. Representing them in the form of trigonometric and algebraic polynomials, we can show that the function $Y(p)$ is an integral analytic function on the entire complex plane and has the form

$$Y\left(\frac{p}{a}\right) = \sum_{k=1}^{\infty}\frac{Y^{(k)}(0)}{k!}\left(\frac{p}{a}\right)^k, \quad Y^{(k)}(0) = i^k a_k,$$

where $a_k = \int_{-\infty}^{\infty} x^k y(x)dx$ are AF moments. Since an AF is a finite and infinitely differentiable function, its Fourier transform $Y(p)$ decreases more rapidly than any power p^k as $p \longrightarrow \infty$. All AF are infinitely differentiable but not analytic; i.e., their smoothness is less than that of polynomials but larger than that of splines. Power series cannot be used for calculating AF values, because, at any point, the Taylor series for an AF either has a zero radius of convergence or is represented by a algebraic polynomial and, consequently, does not con-

* *Institute of Radio Engineering and Electronics, Russian Academy of Sciences, ul. Mokhovaya 18, Moscow, 103907 Russia*
** *Bauman State Technical University, Vtoraya Baumanskaya ul. 5, Moscow, 107005 Russia*
*** *Central Design Bureau of Unique Instrumentation, Russian Academy of Sciences, ul. Butlerova 15, Moscow, 117342 Russia*
**** *Instituto Politechnico Nacional, Unidad Culhuacan, av. Santa Ana No. 1000, C. P. 04430, Col. San Francisco Culhuacan, Mexico, D. F. Mexico*

1028-3358/01/4603-0166$21.00

verge to a finite function. The implementation of the rapidly converging Fourier series

$$y(x) = \frac{1}{2}\sum_{k=-\infty}^{\infty} Y\left(\frac{\pi k}{d}\right)\exp\left(\frac{i\pi kx}{d}\right)$$

provides the most universal method for calculating AF when they are periodically continued beyond the finiteness domain $[-d, d]$.

Presently, faster computation methods are being developed for finding certain AF. In the AF class, the function $\mathrm{up}(x)$ with the support $[-1, 1]$ obeying the equation

$$y'(x) = 2y(2x+1) - 2y(2x-1)$$

is the simplest and, at the same time, fundamental function.

Here, $\mathrm{up}(x)$ has the following representation:

$$\mathrm{up}(x) = \frac{1}{2\pi}\int_{-\infty}^{\infty} F(p)\exp(-ipx)dx, \qquad (2)$$

where

$$F(p) = \prod_{k=1}^{\infty}\frac{\sin(p\times 2^{-k})}{p\times 2^{-k}}. \qquad (3)$$

The key feature of the $\mathrm{up}(x)$ lies in the fact that any algebraic polynomial can be represented by translations of this function; namely, there exist c_k, such that the following equality holds true for any n:

$$x^n = \sum_{k=-\infty}^{\infty} c_k \mathrm{up}(x - k\times 2^{-n}). \qquad (4)$$

This implies that all polynomials of powers no higher than n are contained among linear combinations of translations (with the step $k\times 2^{-n}$) of the function $\mathrm{up}(x)$ and a finite number of nonvanishing terms correspond to each fixed x. The function $\varphi(x)$ is the simplest among all finite functions $\varphi(x)$ with the support $[-1, 1]$ for which property (4) holds: either $\varphi(x)$ is proportional to $\mathrm{up}(x)$ or its derivatives increase faster than those of $\mathrm{up}(x)$:

$$\lim_{n\to\infty}\frac{\|\varphi^{(n)}(x)\|_{C[-1,1]}}{\|\mathrm{up}^{(n)}(x)\|_{C[-1,1]}} = \infty$$

$$\text{for } \mathrm{up}(x)\ \|\mathrm{up}^{(n)}(x)\|_{C[-1,1]} = 2^{n(n+1)/2}.$$

If the space of linear combinations of translations $\sum_{k=-\infty}^{\infty} c_k\,\mathrm{up}(x - k\times 2^{-n})$ by $k\times 2^{-n}$ for the function $\mathrm{up}(x)$ is denoted as UP_n, the following statements hold true:

(a) The spaces UP_n are coordinated: $\mathrm{UP}_n \subset \mathrm{UP}_{n+1}$.

(b) The spaces UP_n are the minimum possible modifications of the infinitely-smooth spline spaces.

(c) In the spaces UP_n, there are bases consisting of translations of the atomic function $\mathrm{Fup}_n(x)$ with the support length approaching zero as $n \longrightarrow \infty$.

By definition, $\mathrm{Fup}_n(x)$ is an AF with the support $[-(n+2)\times 2^{-n-1}, (n+2)\times 2^{-n-1} - 1]$ and its Fourier transform is of the form

$$F_n(p) = \left(\frac{\sin(p\times 2^{-n-1})}{p\times 2^{-n-1}}\right)^{n+1}\prod_{k=n+2}^{\infty}\frac{\sin(p\times 2^{-k})}{p\times 2^{-k}}$$

$$= \left(\frac{\sin(p\times 2^{-n-1})}{p\times 2^{-n-1}}\right)^{n} F(2^{n+1}p).$$

$\mathrm{Fup}_n(x)$ obeys the functional-differential equation

$$y'(x) = 2\sum_{k=0}^{n+2}(C_{n+1}^{k} - C_{n+1}^{k-1})y(2x - k\times 2^{-n-1} + (n+2)\times 2^{-n-2},$$

where C_n^k are binomial coefficients. Translations of $\mathrm{Fup}_n(x)$ by $k\times 2^{-n}$ are linearly independent and form a basis in the space UP_n; $\mathrm{Fup}_n(x)$ can be expressed in terms of linear combinations of translations by $k\times 2^{-n}$ for the function $\mathrm{up}(x)$. It is worth noting that $\mathrm{Fup}_0(x) \equiv \mathrm{up}(x)$.

From (2) and (3), it follows that the function $\mathrm{up}(x)$ is produced by an infinite convolution of the simplest perfect spline, whose Fourier transform is $\frac{\sin(2^{-1}x)}{2^{-1}x}$. The AF $\Xi_n(x)$ with the support $[-1, 1]$ $[\Xi_1(x) \equiv \mathrm{up}(x)]$ is the generalization of the function $\mathrm{up}(x)$ as the infinite convolution of higher-order perfect splines. By definition, the Fourier transform for the function $\Xi_n(x)$ has the form

$$K_n(p) = \prod_{k=1}^{\infty}\left(\frac{\sin(p(n+1)^{-k})}{p(n+1)^{-k}}\right)^{n}.$$

The functions $\Xi_n(x)$ obey the equation

$$y'(x) = 2^{-n}(n+1)^{(n+1)}\sum_{k=0}^{n+2}(-1)^k C_n^k y((n+1)x - 2k + n).$$

The AF $h_\alpha(x)$, $\alpha > 1$ have the Fourier transform

$$K_n(p) = \prod_{k=1}^{\infty}\frac{\sin((\alpha-1)\alpha^{-k}p)}{(\alpha-1)\alpha^{-k}p}$$

and satisfy the functional-differential equations of form (1). In his particular case, $h_2(x) \equiv \mathrm{up}(x)$. In prac-

tice, the function $h_{3/2}(x)$ is widely used in addition to up(x).

The efficient employment of the AF is caused by the fact that they are relatively simple for handling (explicit formulas for values, moments, derivatives, and Fourier transform). On the other hand, AF possess adequate (in some cases, the best) approximation properties. These properties are intimately related to the possibility of representing algebraic polynomials in the form of linear combinations of translations for the functions up(x), Fup$_n(x)$, and $\Xi_n(x)$. The spaces UP$_n$ were proved to be, along with polynomials and splines, extreme or asymptotically extreme for classes of finite-smoothness functions like $W_X^r = \{f(x): \|f^{(r)}\|_X \le 1\}$ [2].

WEIGHT WINDOWS IN DIGITAL PROCESSING OF SPEECH SIGNALS

Speech signals are classified into two main categories: vocalized and nonvocalized (fricative). As opposed to fricative speech segments, vocalized ones are characterized by a higher energy level, as well as a quasiperiodic structure. There are also transition segments between vocalized and nonvocalized signals. Short-term spectral analysis is one of the basic means of speech processing in the frequency region. This method is based on the short-term discrete Fourier transform and allows signal properties hard to detect in the time region to be revealed. The short-term discrete Fourier transform for a signal $s(x)$ can be written in the form

$$X_k(e^{j\omega}) = \sum_{n=-\infty}^{\infty} w(k-n)s(n)e^{-j\omega n},$$

where $w(k-n)$ is the weight-window function used for isolating an input-signal segment being processed corresponding to a discrete time moment k. Thus, the window $w(n)$ isolates the speech-signal segment required for processing and turns the signal to zero outside the region of interest. The window shape and width affect the frequency representation of the speech segment. The ideal frequency response of a window must be characterized by a narrow main lobe (providing high resolution) and an absence of side lobes (causing energy leakage). Since such a window cannot be realized, special window types (rectangular, Hemming-type, Gaussian, etc.) are employed in practice for various applications. Owing to the narrow main lobe, the rectangular window has the maximum frequency resolution but, at the same time, a high level of energy leakage through side lobes. On the other hand, the Blackman window features the minimum energy leakage along with low resolution. As a rule, the window functions to be compared must satisfy the normalization conditions

$$w(x) = 0 \text{ for } |x| > 1, \quad w(0) = 1, \quad w(-x) = w(x).$$

The following weight windows originally introduced by V.F. Kravchenko and V.A. Rvachev [2–4] are constructed on the basis of AF:

$$w_1(x) = \text{up}(x),$$

$$w_2(x) = \text{up}(x) + 0.01\text{up}''(x),$$

$$w_3(x) = \frac{\text{fup}_1(3x/2)}{\text{fup}_1(0)},$$

$$w_4(x) = \frac{\text{fup}_1(3x/2) + 0.0036\text{fup}_1''(3x/2)}{\text{fup}_1(0) + 0.0036\text{fup}_1''(0)},$$

$$w_5(x) = h_{3/2}(x),$$

$$w_6(x) = 1.0696\left(h_{3/2}(x) + \frac{h_{3/2}''(x)}{121}\right),$$

$$w_7(x) = \frac{\Xi_2(x)}{\Xi_2(0)}.$$

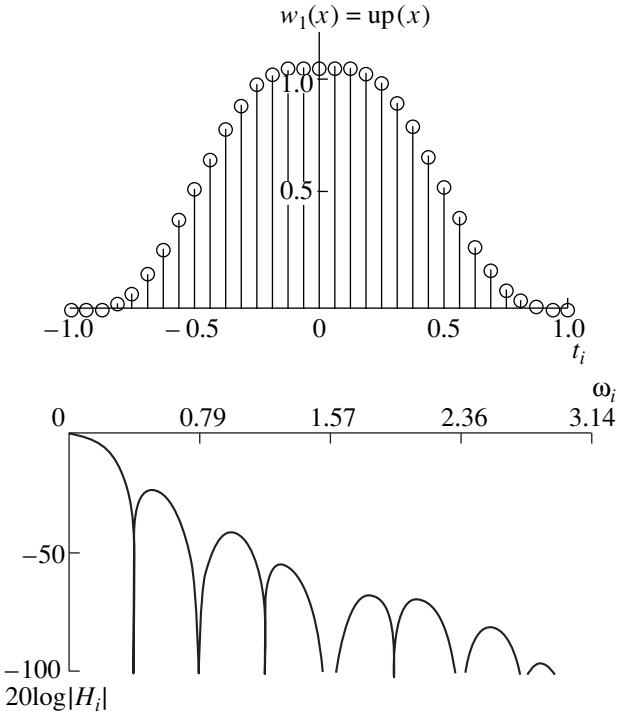

Fig. 1. $w_1(x)$ atomic window [based on the function up(x)] and its logarithmic frequency response.

Figure 1a shows the atomic window $w_1(x)$ and its spectrum. The following system of physical parameters is used for comparing characteristics of various windows:

Characteristics of Kravchenko–Rvachev and classic windows

Window	Parameters							
	b_1	b_2	b_3	b_4	b_5	b_6	b_7	b_8
Kravchenko–Rvachev								
$w_1(x)$	1.6	12	1.2	3.3	−23.3	−∞	2.1	0.5
$w_2(x)$	1.5	17	1.4	3.1	−32.4	−∞	1.9	0.5
$w_3(x)$	1.9	6	0.9	3.6	−37.2	−∞	2.4	0.39
$w_4(x)$	1.8	7	1.1	3.6	−51	−∞	2.3	0.4
$w_5(x)$	1.3	30	0.7	1.7	−36	−∞	2.9	0.52
$w_6(x)$	1.2	32	0.8	1.7	−51	−∞	2.5	0.55
$w_7(x)$	1.9	5	0.9	3.7	−34	−∞	2.4	0.38
Rectangular	1.0	50	3.9	3.9	−13.3	−6	1.2	1
Triangular	1.3	25	1.8	3.1	−26.5	−12	1.7	0.5
Hemming	1.4	23	1.8	3.1	−43	−6	1.8	0.54
Henning	1.5	17	1.4	3.2	−31.5	−18	1.9	0.5
Blackman	1.7	9	1.1	3.5	−58	−18	2.4	0.42
Kaiser–Bessel, $\beta = 3$	1.8	7	1.0	3.6	−69	−6	2.4	0.4
Gaussian, $\alpha = 6.25$	1.5	19	1.6	3.2	−42	−6	1.9	0.49

(1) Equivalent noise band

$$b_1 = 2\frac{\int_{-1}^{1} w^2(x)dx}{\left[\int_{-1}^{1} w(x)dx\right]^2};$$

(2) Correlation of overlapping segments

$$b_2 = \frac{\int_{0}^{1} w(x)w(x-1)dx}{\int_{-1}^{1} w^2(x)dx}100\%;$$

(3) Parasitic modulation amplitude (in decibels)

$$b_3 = -10\log\left|\frac{W(\pi/2)}{W(0)}\right|^2,$$

where $W(p)$ is the Fourier transform for the window function;

(4) Maximum transform loss (in decibels)

$$b_4 = 10\log(b_1) + b_3;$$

(5) Maximum side-lobe level (in decibels)

$$b_5 = 10\log\max_k\left|\frac{W(u_k)}{W(0)}\right|^2,$$

where $\{u_k\}$ are local-maximum points (excluding u_0);

(6) Asymptotic decrease rate for side lobes (in decibels per octave)

$$b_6 = 10\log\lim_{u\to\infty}\left|\frac{W(2u)}{W(u)}\right|^2;$$

(7) The window width at a level of 6 dB $b_7 = 2u$, where u is the highest frequency, such that

$$10\log\left|\frac{W(0)}{W(u)}\right|^2 = 6;$$

(8) Coherent amplification

$$b_8 = \frac{1}{2}\int_{-1}^{1} w(x)dx.$$

The table lists calculated physical characteristics for atomic and classic windows. AF-based windows can be seen to be superior to well-known ones in the b_6-parameter. The simplest atomic $w_1(x)$ window has a relatively high side-lobe level. For its improvement, $w_1(x)$ must be modified, resulting in a $w_2(x)$ window with a lower level of side lobes. This window turns out to be close to a Henning window except for the parameter b_6. Introducing the $w_5(x)$ window makes it possible to significantly reduce the b_3-parameter. The b_5-parameter can be improved using the $w_6(x)$ window. When compared with the $w_5(x)$ and $w_6(x)$ windows, the $w_3(x)$ and $w_4(x)$ windows have an advantage: the function $\mathrm{fup}_n(x)$ and

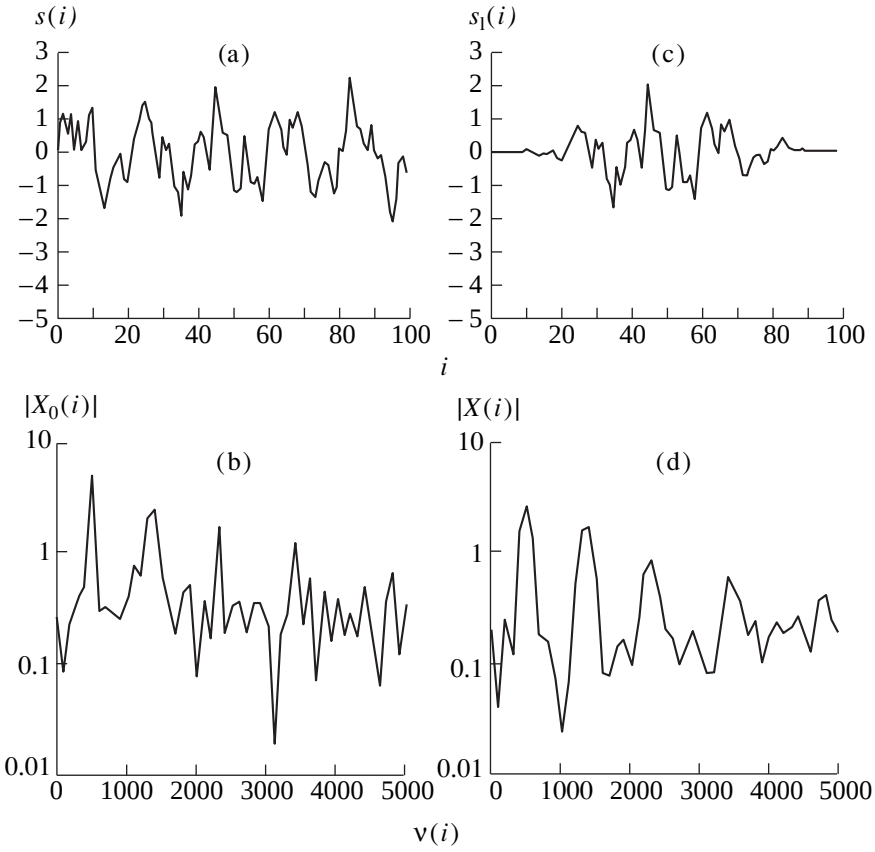

Fig. 2. (a) Initial speech signal; (b) frequency response (dB) of a signal processed with a 10-ms-duration rectangular window; (c) speech signal processed with a 10-ms-duration $w_1(x)$ weight window; (d) frequency response (dB) for a signal processed with a 10-ms-duration $w_1(x)$ window.

its derivatives are easier to calculate compared to $h_{3/2}(x)$.

NUMERICAL EXPERIMENT

We now consider a model of a speech signal composed of four sinusoids with frequencies of 500, 1350, 2300, and 3400 Hz,

$$s(t) = \sin(2\pi \times 500t) + 0.7\sin(2\pi \times 1350t) + 0.3\sin(2\pi \times 2300t) + 0.2\sin(2\pi \times 3400t),$$

which is noise-polluted by a random additive component with a zero mean value and unit amplitude (Fig. 2a). Employing the $w_1(x)$ atomic window, we isolate a signal segment with a duration of 10 ms (Fig. 2c). The digitization was realized with a frequency of 10^4 Hz. Figures 2b and 2d show logarithms of the absolute values for the short-term discrete Fourier transform of a signal weighted with rectangular and $w_1(x)$ atomic windows. This transform can be easily computed for an atomic window since the Fourier transform (3) for the function up(x) is known. It is clearly seen in the case of a rectangular window that the peaks of the frequency response, which correspond to the initial-signal harmonics, are narrower and sharper (high frequency resolution). At the same time, due to the energy leakage caused, in this case, by a high side-lobe level, the short-term spectrum appears more noise-polluted compared to the case of the atomic window. This hinders identifi-

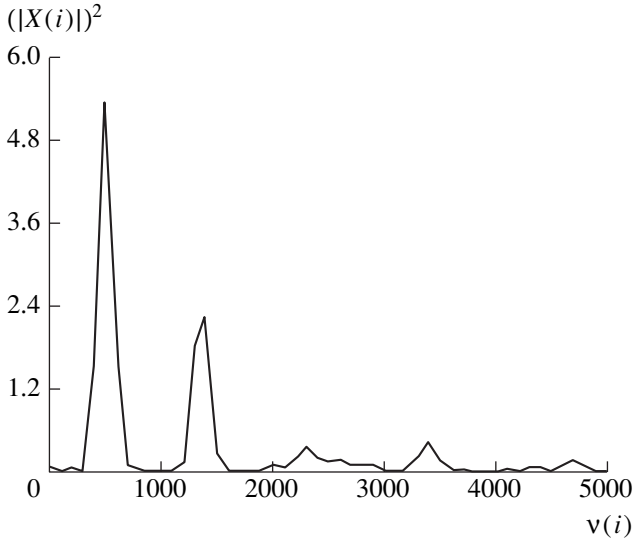

Fig. 3. Power spectrum for a signal processed with a 10-ms-duration $w_1(x)$ window.

cation of the initial harmonics. Figure 3 illustrates the short-term power spectrum for the segment of the signal processed by the $w_1(x)$ window. Here, there are clearly visible peaks corresponding to frequencies of input-sequence harmonic components.

We consider a linear predictive coding employed for finding a fundamental-tone frequency in speech recognition, synthesis, and coding problems [1, 10–12]. Then, a discrete sequence $s[n]$ can be predicted from its preceding values:

$$\tilde{s}[n] = -\sum_{k=1}^{P} a[k]s[n-k],$$

where P is the order of a linear predictor and $a[k]$ are coefficients of the linear prediction. In accordance with the least square technique, we arrive at the system of equations for minimizing the prediction error:

$$\sum_{k=1}^{P} \hat{a}[k]\sum_{n} s[n-k]s[n-m] = -\sum_{n} s[n]s[n-m],$$
$$1 \le m \le P.$$

Here, $\hat{a}[k]$ are estimates for the coefficients $a[k]$. Generally, summation must be taken over all values of n. However, in practice, it is taken over a limited number of readings $s[n]$, so that the steadiness condition for $s[n]$ is met. To this end, $s[n]$ is bounded by the window $w[n]$:

$$s'[n] = \begin{cases} s[n]w[n], & 0 \le n \le N-1 \\ 0 \quad \text{for other } n. \end{cases}$$

Thus, we arrive at the system

$$r[m] = -\sum_{k=1}^{P} \hat{a}[k]r[m-k], \quad 1 \le m \le P,$$

where $r[m] = \dfrac{1}{N-m}\sum_{n=0}^{N-1-m} s'[n]s'[n+m]$ is the autocorrelation function for the sequence $s'[n]$. With allowance made for autocorrelation-function evenness, this system can be solved by the recursive Durbin's algorithm [1]. The linear speech prediction can be used for finding the frequency response of the voice path:

$$H(e^{j\omega}) = \frac{G}{1 + \sum_{k=1}^{P} \hat{a}[k]e^{-jk\omega}},$$

where G is the gain. Figure 4 shows the short-term spectrum for the initial speech signal and amplitude–frequency characteristic for the voice path calculated with the help of the linear prediction. The $w_1(x)$ atomic window was used; the predictor order is $P = 10$. The harmonic-signal formants are clearly seen in Fig. 4.

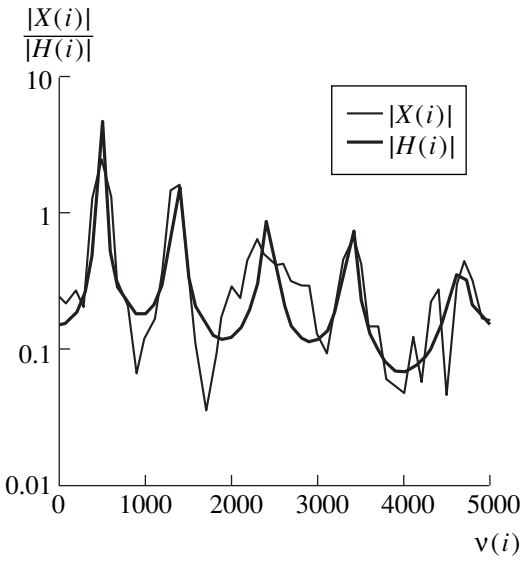

Fig. 4. Short-term spectrum and the amplitude–frequency characteristic of a voice path.

It is worth noting that the $w_1(x)$ window is not optimum in its characteristics (see table). Other atomic-window types can be more efficient in solving more complicated problems of speech-signal processing [10–12].

CONCLUSIONS

On the basis of the proposed and substantiated method, numerical experiments were fulfilled. They confirmed the efficiency of digital signal-processing methods based on atomic functions. Appropriate choice of these functions makes it possible to obtain, on their basis, weight windows comparable in a number of the most important characteristics with other well-known windows. It is shown that the atomic windows are superior to the well-known ones in certain physical characteristics [1]. This allows these windows to be widely used in solving problems of speech digital processing.

ACKNOWLEDGMENTS

The authors are grateful to Academician of the National Academy of Sciences of Ukraine V.L. Rvachev, Dr. Luis Nino-de-Rivera, and Professor V.I. Ponomarev for fruitful discussions of the results.

REFERENCES

1. A. M. Kondoz, *Digital Speech* (Wiley, 2000).
2. V. F. Kravchenko, V. A. Rvachev, and V. L. Rvachev, Radiotekh. Élektron. (Moscow) **40**, 1385 (1995).

3. V. F. Kravchenko, V. A. Rvachev, and V. L. Rvachev, Dokl. Akad. Nauk SSSR **306**, 78 (1989) [Sov. Phys. Dokl. **34**, 430 (1989)].
4. V. F. Kravchenko, M. A. Basarab, and H. Pérez-Meana, Telecommun. Radio Eng. **56** (1) (2001).
5. M. A. Basarab and V. F. Kravchenko, Élektromagn. Volny Élektron. Sist. **5** (4), 4 (2000).
6. Yu. V. Gulyaev, V. F. Kravchenko, and V. A. Rvachev, Dokl. Akad. Nauk **342**, 29 (1995).
7. V. F. Kravchenko and V. A. Rvachev, Zarubezh. Radioélektron. Usp. Sovrem. Radioélektron., Nos. 4, 3 (1996).
8. V. F. Kravchenko, V. A. Rvachev, and V. I. Pustovoĭt, Dokl. Akad. Nauk **351**, 16 (1996).
9. V. F. Kravchenko, V. I. Pustovoĭt, and V. V. Timoshenko, Radiotekhnika, No. 1, 26 (1997).
10. F. Casco, H. Pérez, M. Nakano, and M. López, IEICE Trans. Fundam. Electron. Commun. Comput. Sci. **E-78-A**, 1004 (1995).
11. L. Nino-de-Rivera, H. Pérez-Meana, and E. Sánchez-Sinencio, Analog Integr. Circuits Signal Process. **21**, 127 (1999).
12. L. Nino-de-Rivera, H. Pérez-Meana, and E. Sánchez-Sinencio, J. Signal Process. **2** (4), 309 (1998).

Translated by V. Tsarev

Doklady Physics, Vol. 46, No. 3, 2001, pp. 173–176. Translated from Doklady Akademii Nauk, Vol. 377, No. 2, 2001, pp. 190–193.

TECHNICAL PHYSICS

Amorphization Conditions for Metallic Alloys while Superfast Quenching from the Liquid State and Structural Relaxation by Subsequent Heating

M. Kh. Shorshorov

Presented by Academician N.P. Lyakishev May 29, 2000

Received June 7, 2000

Rigorous theoretical analysis of cluster formation in metallic melts and of nanoamorphous solid phases produced with participation of these clusters is possible only on the basis of thermodynamics of small systems (T. Hill's method) [1, 2]. Indeed, the allowance for the contribution of the surface energy and defects into the energy state and dynamic equilibrium of clusters is impossible in the Gibbs thermodynamics of macroscopic systems. According to the theory of homogeneous nucleation, which was developed in [1], the expression for the work of the cluster nucleation in binary metallic melts has the form

$$\Delta f_n = \frac{\Delta F_n}{kT} = -\alpha n + \beta n^{2/3} - \gamma n^{1/2}. \qquad (1)$$

Here, $\alpha = \dfrac{\mu_c - \mu_m}{kT} = \dfrac{\Delta\mu}{kT}$ is the difference in chemical potentials μ_c and μ_m of the cluster and melt surrounding it; $\beta = \dfrac{\alpha_0 \sigma v_a^{2/3}}{kT}$ is the term responsible for the surface tension σ on the cluster boundary;

$$\gamma = \frac{H_0 n_0 + H_i n_i}{n_0 + n_i}\left(\frac{\kappa}{v_a}\right)^{1/2}(kT)^{-1/2}$$

is the term taking into account fluctuations of the energy and density; v_a is the atomic volume; α_0 is the coefficient allowing for cluster shape; T is temperature; κ is the isothermal compressibility; n_0 is the number of atoms in the alloy base; n_i is the number of impurity atoms in a cluster; $n_0 + n_i = n$; and H is the enthalpy per atom.

In contrast to the well-known equation of the classical theory of homogeneous nucleation, Eq. (1) has an additional term $\gamma n^{1/2}$. For small β (solidification), the maximum of the function Δf_n, which defines the cluster critical size n_j for $\beta > \gamma$, is equal to

$$n_j = \left\{2\left(\frac{2\beta}{9\alpha}\right)^{1/2}\cos\frac{\pi - \phi'}{3}\right\}^6, \qquad (2)$$

where $\phi' = \arccos\dfrac{2.38\alpha^{1/2}\gamma}{\beta^{3/2}}$.

It is well known [1] that the absolute equilibrium concentration of clusters at a temperature T can be written as

$$N_j = N_A \exp[-(-\alpha n_j + \beta n_j^{2/3} - \gamma n_j^{1/2})], \qquad (3)$$

where N_A is the Avogadro's number. Analysis of the clusterized-melt state within the framework of the quasichemical model [3] for a number of binary systems based on Fe, Ni, Cr, Ti, Cu, and Zr and containing metalloid and metallic components was carried out in [1]. It was shown for the Fe–C system, as an example (Fig. 1), that the absolute N_j and the relative $\dfrac{n_c}{N_A}$ concentrations of the clusterized atoms increase with temperature, while the number n_j of atoms in the clusters decreases. With increasing the concentration of the second components (before the eutectic point), the first three parameters decrease and n_j increases. Beyond the eutectic point, all things proceed in the inverse direction. Metalloids clusterize the melts more intensely than metals. It is characteristic that clusters in melts with metallic components have larger sizes, but their concentration is lower than in melts with metalloids. The formation of centers of a solid amorphous phase in the case of superfast quenching from the liquid state occurs on melt clusters with participation of coalescence of neighboring clusters. This fact promotes actual high nucleation rates I_n. The higher the temperature of the melt quenching, the smaller the number of

Baĭkov Institute of Metallurgy and Material Science, Russian Academy of Sciences, Leninskiĭ pr. 49, Moscow, 117911 Russia

1028-3358/01/4603-0173$21.00

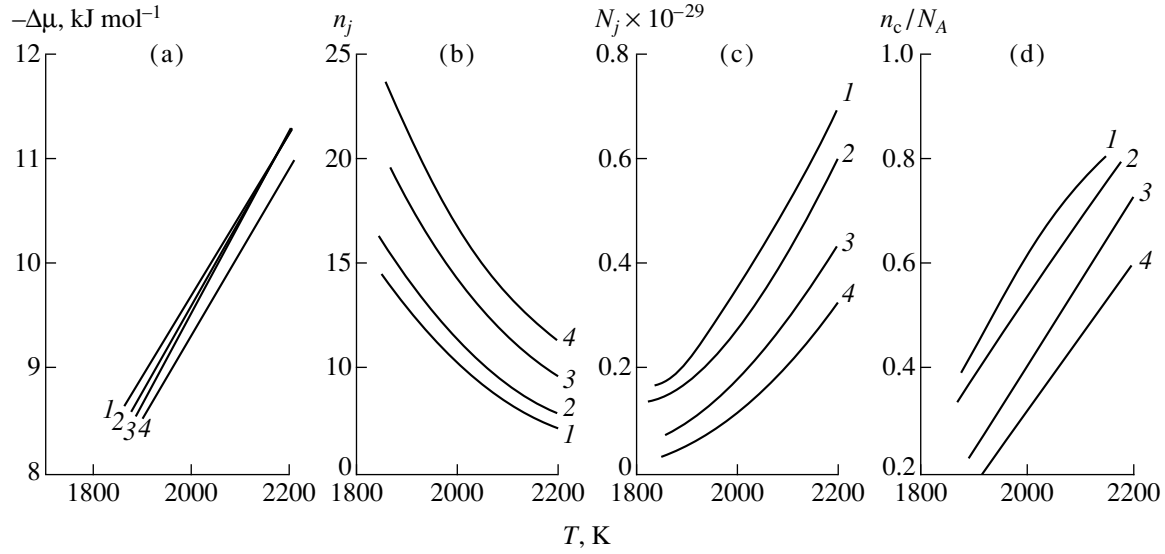

Fig. 1. Polyterms for differences in chemical potentials Δμ; number of atoms n_j in critical-size clusters; cluster concentration N_j; and the relative concentration $\frac{n_c}{N_A}$ of clusterized atoms in melts for alloys of iron with carbon at carbon contents, wt % of (*1*) 0.1; (*2*) 0.3; (*3*) 0.8; and (*4*) 0.23.

atoms in clusters n_j and in solid-phase centers i_{cr}. Therefore, as a consequence, the dispersion of the structure formed is also higher [1]. Comparison of the calculated and experimental results for n_j and i_{cr} confirms the contribution of the coalescence of neighboring clusters into the formation of amorphous phase i_{cr}. For pure metals, this contribution lies within the range 80 to 220, and for alloys, it is from several hundreds up to 600: the ratio i_{cr}/n_j is 4 to 11. In the vicinity of the melting point, the viscosity of metallic melts is high and increases by several orders of magnitude in the case of deep supercooling $\left(\Delta\bar{T} = \frac{T_L - T}{T_L} \geq 0.22\text{–}0.25\right)$. Ultimately, this presents a necessary condition for the formation of the nanoamorphous solid phase based on the cluster structure of melts [1]. These conditions are valid only for high cooling rates exceeding a certain critical value $W_{c,cr}$, which also depends on the thermophysical properties of the melt and the heat-transfer conditions.

Table

Composition, at. %	T_L, K	Phase content	$\frac{T_C}{T_L}$	$W_{c,cr}$, K s^{-1}	n_j	i_{cr}
Cu_{75}–Zr_{25}	1388	Peritectic	0.50	2×10^5	32	221
Cu_{65}–Zr_{35}	1373	Eutectic	0.60	4.5×10^3	58	602
Cu_{56}–Zr_{44}	1163	"	0.64	8×10^4	42	390
Cu_{46}–Zr_{54}	1201	"	0.58	2×10^5	36	280

Solidification kinetics of the two-phase zone in a flat ingot (the case of the melt spinning process) is usually described by the Kolmogorov equation [1, 4]. The cooling rate of the two-phase zone at the solidification boundary is determined by the source method with allowance for the solidification heat ΔH_S [1]. We analyzed the Zr concentration effect on the value of $W_{c,cr}$ for the Cu–Zr system taken as an example. The calculation data within the Zr-concentration range from 25 to 54 at. % practically coincided with the experimental data of [1, 5, 6]. They confirmed that the minimum values of $W_{c,cr}$ correspond to the eutectic concentration of Zr (see the table).

The stability of amorphous-melt properties depends on temperature. For example, while heating, the strength, electrical resistance, and thermal conductivity decrease for Fe and Ni alloys doped with P, B, and C. In this case, internal-friction peaks appear caused by the segregation of metalloids on free surfaces and around submicropores. For example, in alloys of Fe with B and Fe with P, peaks at 317 [7] and 313 K [8] appear, respectively, etc. Sizes of pores (about 10 nm) [9] are close to the mean sizes of fragments of a free volume in melts. The segregation process near the plane boundary is described in [10] (see Fig. 2, curve *1*). The solution to the problem of segregation around the micropores requires analysis of the equation for diffusion of impurity atoms from the volume between the neighboring

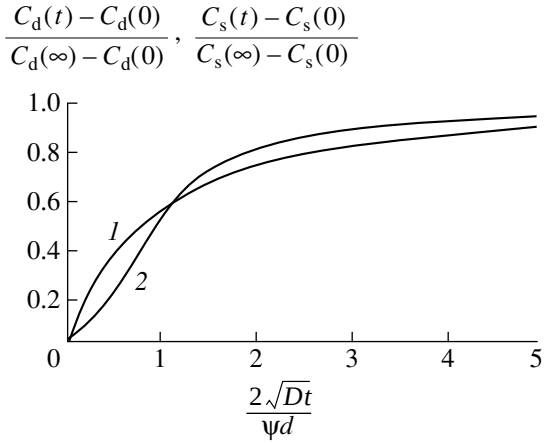

Fig. 2. (*1*) Time variations of the impurity concentration $C_d(t)$ at the body boundary and (*2*) $C_s(t)$ in near-surface layers around the submicropores. D is the diffusion coefficient.

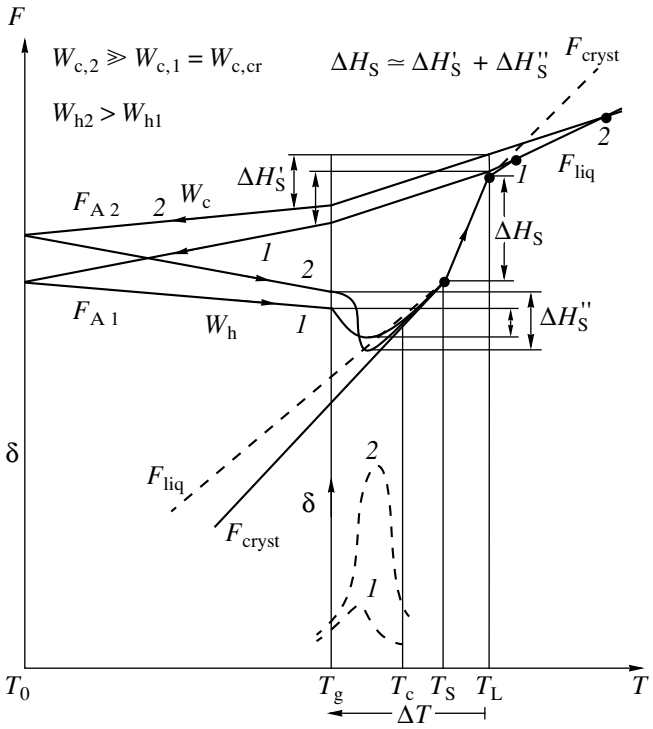

Fig. 3. Character of the variation in the free energy F_A for amorphous alloys in the case of superfast cooling of melts and subsequent continuous heating to the solidus temperature T_S (solid lines) and plasticity δ within the range $T_g - T_c$ (dashed lines) as a function of the cooling rate W_c and heating rate W_h.

submicropores:

$$\frac{dC}{dt} = D\left[\frac{1}{r^2}\frac{d}{dr}\left(r^2\frac{dC}{dr}\right)\right], \quad (4)$$

with complicated initial conditions $C(r, t)|_{t=0} = C(0)$ at $r_p + d < r < L$, $C(r, t)|_{t=0} = \frac{C(0)}{\phi}$ as $r \longrightarrow r_p$ and boundary conditions

$$\left.\frac{dC}{dr}\right|_{r=L} = 0, \quad \left.\left[D\left(\frac{dC}{dr}\right) - d\phi\frac{dC}{dt}\right]\right|_{r=r_p+d} = 0.$$

Here, d is the thickness of the pore near-surface layer; r is the pore radius; L is the half-distance between neighboring pores; $\phi = \frac{C_p(\infty)}{C_p(0)}$ is the equilibrium segregation coefficient; $C_p(\infty)$ is the ultimate concentration of a segregating element in the pore near-surface layer; and $C_p(0)$ is the initial concentration of this element, which coincides with its mean bulk concentration. The distance L changes from 0.1 to 1 μm [8, 9]. Equation (4) is calculated by the finite-difference method for the thickness d equal to six interatomic distances a and for the mean micropore radius $r_p = 5$ nm (see Fig. 2, curve *2*). At the initial stage, the segregation near the plane boundary occurs more rapidly than around submicropores. However, in the second case, the saturation process is shorter. We can estimate it by the time t_r of attaining 90% of the ultimate concentration.

Above the glass-transition temperature T_g, the viscosity of alloys drastically decreases and still below T_c (crystallization), endothermic peaks, as well as plasticity peaks δ, arise (Fig. 3). With elevating the heating rate W_h, δ peaks become more pronounced and shift towards higher temperatures. For strain rates of about 1×10^{-2}–1×10^{-4} s^{-1}, the magnitudes of the δ peaks amount to several hundreds of percents, which is intrinsic to superplasticity [11, 12]. In Fig. 3, the character of the variation of the free energy F_A is also shown as a function of T and W_h for the two states after melt quenching: (*1*) for $W_{c,1} \geq W_{c,cr}$ and (*2*) for $W_{c,2} = W_{c,cr}$. In this case, for the alloy obtained according to mode *2*, W_{h2} is larger than W_{h1} for the alloy obtained according to mode *1*. With the elevation of the quenching temperature T, (dots *1* and *2*) and W_h, the fraction ΔH_S of heat released in the process of crystallization increases.

REFERENCES

1. M. Kh. Shorshorov and A. I. Manokhin, *Theory of Nonequilibrium Crystallization of a Flat-Shaped Ingot* (Nauka, Moscow, 1992).
2. T. L. Hill, *Thermodynamic of Small System* (Benjamin, New York, 1963, 1964), Parts 1, 2.
3. B. A. Baum, *Metallic Liquids: Problems and Hypotheses* (Nauka, Moscow, 1979).
4. A. N. Kolmogorov, Izv. Akad. Nauk SSSR, Ser. Mat. **3**, 355 (1937).

5. A.I. Manokhin, B. S. Mitin, A. V. Revyakin, *et al.*, *Amorphous Alloys* (Metallurgiya, Moscow, 1984).
6. H. A. Davies and B. G. Lewis, Scr. Metall. **9**, 1107 (1975).
7. F. N. Tavadze *et al.*, in *Internal Friction in Metals and Alloys* (Nauka, Moscow, 1966), pp. 37–39.
8. Yu. V. Gridina, E. É. Glikman, and Yu. V. Piguzov, in *Internal Friction in Metals and Alloys* (Nauka, Moscow, 1966), pp. 91–94.
9. A. M. Glezer, B. V. Molotilov, and O. L. Utevskaya, in *Amorphous Metal Alloys* (Metallurgiya, Moscow, 1983), pp. 90–96.
10. M. Kh. Shorshorov, *Physical Metallurgy of Welding of Steel and Titanium Alloys* (Nauka, Moscow, 1965).
11. A. S. Tikhonov and M. Kh. Shorshorov, *Physical Materials Science in USSR* (Naukova Dumka, Kiev, 1986), pp. 240–251.
12. V. A. Khonik and V. A. Zelenskiĭ, Fiz. Met. Metalloved. **61**, 602 (1986).

Translated by T. Galkina

Doklady Physics, Vol. 46, No. 3, 2001, pp. 177–179. Translated from Doklady Akademii Nauk, Vol. 377, No. 3, 2001, pp. 325–327.

TECHNICAL PHYSICS

On Crystallite (Grain) Growth by Recrystallization

V. V. Gubernatorov, L. R. Vladimirov, and Yu. N. Gornostyrev

Presented by Academician N.A. Vatolin August 8, 2000

Received September 5, 2000

The phenomenon of grain growth by recrystallization, i.e., absorption of one kind of crystallite by another crystallite of the same phase, is long and widely employed in metallurgical technology. However, a lot of unsolved questions remain in understanding recrystallization. For example, it is unclear how the residual dislocation density is produced by recrystallization [1], why an unusually high (compared to the calculated rate) crystallite-growth rate occurs in the case of secondary recrystallization (when individual large crystallites suddenly appear in a fine-grained matrix and rapidly grow, with the sizes of the remaining grains being constant) [2].

In this paper, a geometric model of crystallite growth in a three-dimensional structure by secondary recrystallization is proposed. The model makes it possible to explain certain regularities experimentally found in the study of the recrystallization process. The basis of the model is the concept of allowance for the effect of triple, quadruple, and quintuple grain junctions upon the migration of intergrain boundaries. In this case, other modern concepts also are used (see, e.g., [3]). According to these concepts, intergrain boundaries and their junctions are considered as crystal-structure regions (or volumes) in which various defects are present.

It is well known [4] that the front of secondary recrystallization has a peculiar shape: triple junctions of a developing crystallite (TJ_c) are extended along the matrix grain boundaries (B_m); the segments of a developing crystallite boundary (B_c), which connect TJ_c, are bent inward from a large crystallite. This configuration of the recrystallization front implies that in the crystallite development, TJ_c plays a leading role and the crystallite-growth rate V is controlled by the process of straightening of the concave B_c, which depends on their mobility M.

In addition, along with B_m and TJ_c moving over these boundaries, the triple junctions (TJ_m) of the matrix grains and the quadruple junctions ($4QJ_c$) of the growing crystallite moving over them participate in the process of crystallite development (Fig. 1). Therefore, in estimating the secondary-recrystallization rate, we should bear in mind the enhancement of the process driving force owing to the gain P_t in the energy of TJ_m and use the expression $V = M(P_b + P_t)$, where P_b is the grain-boundary energy gain.

We now consider the general case of the development of a crystallite, when it absorbs matrix grains differing from it in orientation. In the growth of a crystallite, TJ_c moving along B_m and colliding with TJ_m produces very defective quadruple grain junctions ($4QJ_{vd}$). They are, at least, more defective than the joining boundaries (Fig. 2a). These junctions, as more defective microvolumes, are incapable of growth and motion and prevent the motion of B_c. Therefore, after their straightening, crystallite development in this segment ceases.

After the crystallite growth has been stopped, small fractions of the matrix grains remain (AA_1B_1 in Fig. 2a). They are absorbed by neighboring matrix grains by breaking-off B_m (AB, AB_1, A_1B_1, and A_1B_2) from $4QJ_{vd}$, by displacement (indicated by dashed lines in Fig. 2b) with formation of new TJ_c (J, J_1, J_2) and B_m (CB, C_1B_1, C_2B_2), and by conservation (complete or partial) of $4QJ_{vd}$. This process is similar to the migration of boundaries in bicrystals of specific geometry (in particular, when one of the crystals has a shape of a small cor-

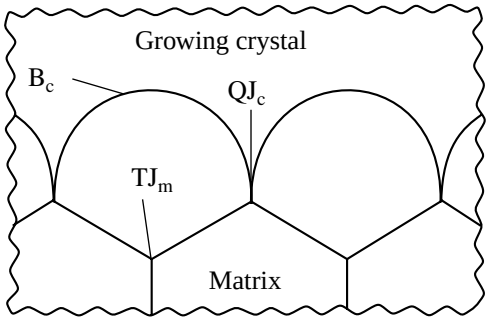

Fig. 1. Schematic diagram for the front of secondary recrystallization.

Institute of Metal Physics, Ural Division,
Russian Academy of Sciences,
ul. S. Kovalevskoĭ 18, Yekaterinburg, 620219 Russia

1028-3358/01/4603-0177$21.00 © 2001 MAIK “Nauka/Interperiodica”

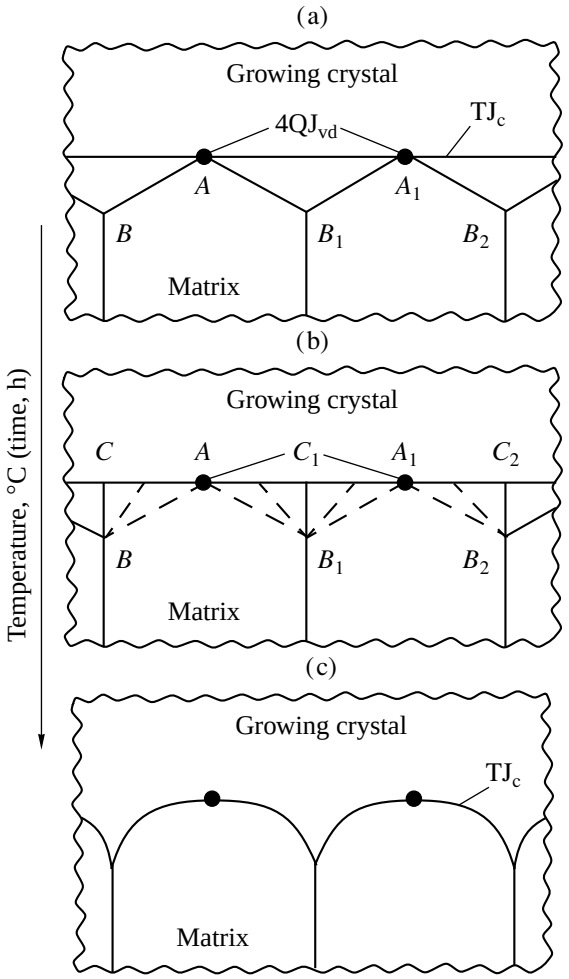

Fig. 2. Model for crystallite-growth by recrystallization.

ner [5]). The size enhancement by a factor of 1.2 to 1.3 of the matrix grains directly surrounding the developing crystallite can be regarded as proof of the development of this process [6].

The newly formed TJ_c immediately begin to move along the newly produced B_m and "pull" the B_c twisting them (Fig. 2c). Then, the concave B_c straighten, and afterwards, the processes listed above are repeated.

Similar processes proceed also by translation of $4QJ_c$ along TJ_c: $4QJ_c$ collide with quadruple junctions of the matrix grains ($4QJ_m$) and produce very defective quintuple grain junctions ($5QJ_{vd}$). The remaining small fractions of matrix grains are absorbed by neighboring matrix grains with the formation of new TJ_m and $4QJ_c$ under the conservation of $5QC_{vd}$.

The growth of crystallites according to the scheme under consideration can have the following specific features:

1. By absorption of the remaining small fractions of matrix grains by neighboring boundary grains of the matrix, B_m, moving over B_c and reprocessing and/or sucking off a fraction of their defects and impurities, make B_c less defective, more pure, and, consequently, more mobile. An unusually high crystallite growth rate by secondary recrystallization is associated with an increase in M (owing to "improving" B_c) and P (owing to the gain in the energy of TJ_m).

2. Crystallite boundary grains can break off from the defective microvolumes (fragments of $4QJ_{vd}$ and $5QJ_{vd}$) or move only after the fragments of $4QJ_{vd}$ and $5QJ_{vd}$ have been reprocessed (or sucked-off) by B_c. In the case of realization of the first variant, the growing crystallite will contain defective microvolumes.

Under secondary recrystallization, as a rule, the large-angle specific (having the definite density of coinciding lattice points) and arbitrary B_c migrate. Due to their different structure, specific B_c break off from the fragments of $4QJ_{vd}$ and $5QJ_{vd}$, while the arbitrary B_c reprocess them. Therefore, a migrating specific B_c leaves behind more defects than an arbitrary one (this is confirmed, e.g., by the defective structure of intergrain regions of recrystallized films [7]).

3. The effect of retardation of the B_c motion by fragments of $4QJ_{vd}$ and $5QJ_{vd}$ depends on the structure of the latter fragments (i.e., on the density of defects in them), which is, to a large extent, set by the structure (imperfection) of the migrating B_c. Under other similar conditions, specific B_c move faster than the arbitrary B_c, as they (owing to their lesser imperfection) form $4QJ_{vd}$ and $5QJ_{vd}$ which possess a less retarding action. An essential contribution of the large-angle specific B_c to the texture formation by secondary recrystallization is induced by this phenomenon.

In particular cases, a developing crystallite can meet both a grain similar to it and a grain slightly differing from it in orientation. In the first variant, similar TJ (or QJ) collide and annihilate; $4QJ_{vd}$ (or $5QJ_{vd}$) do not appear, and this fact does not affect the growth and structure of the crystallite being developed. In the second variant, TJ (or QJ) slightly differing in structure collide and, as a result, low-defective quadruple (or quintuple) junctions of grains are formed, which are less defective than the joining boundaries. $4QJ_{ld}$ (or $5QJ_{ld}$), as low-defective microvolumes capable of growth (developing), become recrystallization nuclei (similar to the transformation of certain segments of the split boundaries near the triple junction or near the sample surface to recrystallization centers [8]) and develop owing to the absorption by them of more defective boundaries. Here, a "critical" recrystallization exists (when the boundary migration is stimulated by the difference in the defect densities on different sides of the boundary [9]). In this case, certain regularities of the critical recrystallization are revealed (accelerated motion of boundaries is observed; the remaining migrating boundaries have an enhanced defect density [9]). This produces the through (in the entire bulk of the crystallite) and wide (up to 0.2 mm) defective interlayer dis-

covered in [10, 11]. The accelerated motion of boundaries in the process of critical recrystallization and production of a defective intergrain structure (substructure) is caused by the intense sink (or sucking off) of defects and impurities from the migrating boundaries into the defect nuclei. Such a mechanism of forming a defective interlayer makes it possible to consider it a defective grain slightly different in orientation from the developing crystallite.

In conclusion, we would like to note that the crystallite-growth model proposed in this paper has the following advantages:

It can be realized in full measure in the case of primary recrystallization (when the developing crystal absorbs subgrains and polygons).

It explains the unusually high rate of the crystallite growth by secondary recrystallization.

It suggests, at least, two mechanisms of substructure formation (defective microvolumes and interlayers) in developing crystallites.

It makes it possible to understand the causes of the effect of large-angle specified boundary migration in the formation of substructure and crystallographic textures by recrystallization.

It takes into account the effect of impurities on the behavior of boundaries, as well as of triple and quadruple junctions.

ACKNOWLEDGMENTS

This work was supported by the Russian Foundation for Basic Research, project no. 99-02-16279.

REFERENCES

1. M. A. Shtremel', *Alloy Strength. Lattice Imperfection* (Metallurgiya, Moscow, 1982).
2. V. Yu. Novikov, *Secondary Recrystallization* (Metallurgiya, Moscow, 1990).
3. O. A. Kaĭbyshev and R. Z. Valiev, *Grain Boundaries and Metal Properties* (Metallurgiya, Moscow, 1987).
4. R. W. Cahn, in *Physical Metallurgy*, Ed. by R. W. Cahn (North-Holland, Amsterdam, 1965; Mir, Moscow, 1968), Vol. 3.
5. M. S. Masteller and C. L. Bauer, *Recrystallization of Metallic Materials*, Ed. by F. Haessner (Riederer-Verlag, Stuttgart, 1971; Metallurgiya, Moscow, 1982).
6. A. K. Sbitnev, B. K. Sokolov, and V. V. Gubernatorov, Fiz. Met. Metalloved. **79** (2), 106 (1995).
7. V. M. Kosevich, in *Proceedings of the III All-Union Conference on Textures and Recrystallization in Metals and Alloys*, Krasnoyarsk, Russia, 1980, pp. 230–232.
8. Ch. V. Kopetskiĭ and L. K. Fionova, Poverkhnost, No. 2, 5 (1984).
9. S. S. Gorelik, *Recrystallization of Metals and Alloys* (Metallurgiya, Moscow, 1978).
10. V. V. Gubernatorov, B. K. Sokolov, N. A. Bryshko, *et al.*, Dokl. Akad. Nauk SSSR **255**, 1367 (1980) [Sov. Phys. Dokl. **25**, 1018 (1980)].
11. V. V. Gubernatorov, G. V. Kurlyandskaya, N. A. Bryshko, and B. K. Sokolov, Izv. Akad. Nauk SSSR, Ser. Fiz. **49**, 1624 (1985).

Translated by T. Galkina

Doklady Physics, Vol. 46, No. 3, 2001, pp. 180–183. From Doklady Akademii Nauk, Vol. 377, No. 3, 2001, pp. 328–331.

ASTRONOMY, ASTROPHYSICS, COSMOLOGY

Dynamic Screening of Gravitational Interaction and the Problem of Ephemeris Time[1]

A. G. Bashkirov, A. V. Vityazev, and G. V. Pechernikova

Presented by Academician T.M. Éneev September 22, 2000

Received September 22, 2000

The density disturbance in a system of gravitating masses, which is induced by a moving isolated body, gives rise to dynamic screening of the Newtonian potential of this body. When applied to the Solar planetary system, this implies that, because of the motion of the Sun in the Galaxy, the solar gravitational potential turns out to be more weak than the Newtonian potential. The relevant modifications of the basic relations of celestial mechanics leads, in particular, to an increase in the estimated period of the revolution of the Earth around the Sun by approximately 1 s. Such an increase in the ephemeris year compensates by an order of magnitude the observable mean difference between ephemeris time and universal time.

1. INTRODUCTION

The problem of consistency of universal time (UT) with ephemeris time (ET) has a long history and is well known in astronomy and geophysics. The first of them, UT, is based on the Earth's rotation rate (spin) with allowance for nonuniformity of this rate and variations of the actual solar day, which are due to the motion of the Earth in its inclined elliptic orbit. Ephemeris time was introduced later, when more sophisticated observatory technology and methods of celestial mechanics became available. It is determined in terms of the observable periodic motion of planets around the Sun or the Moon around the Earth with invoking calculations based on the equations of motion for an observable body in the force field of other gravitating bodies.

At present, the primary time scale is the International atomic time (TAI), which is based on the frequency of atomic oscillations. The second is taken as a time unit in the International System (SI) and is defined through the period of atomic oscillations of caesium. The initial calibration [1] of the SI second was performed by comparing it with the ET second. Therefore, the ET and TAI time scales match very closely.

However, an actually observable discrepancy between the UT and ET time scales exists. The ET time scale appears to run faster then the UT one. As a result, the ephemeris year $T_{\oplus}^{\mathrm{eph}}$ (the period of the Earth's revolution around the Sun) is shorter than the UT year.

As a consequence of the nonuniformity of the Earth's spin, the difference between the UT and ET years fluctuates. This fact forces the International Time Service of the International Astronomical Union to perform permanent observations and to report annually on the difference $\Delta T = \mathrm{UT} - \mathrm{ET}$ (or $\Delta T = \mathrm{UT} - \mathrm{TAI}$) accumulated per year (from 1900 to date). The well-traced systematic difference $\widetilde{\Delta T} \simeq 0.8$ s/year is observed against the fluctuation background.

There were numerous attempts to attribute this difference to different effects, e.g., the slowing down due to tidal friction of the Earth's spin [2] or relativistic effects [3] affecting the Keplerian period of the Earth's revolution around the Sun. Nevertheless, the issue remains open.

Here, we propose a new approach to this problem which is based on the dynamic screening of the Newtonian potential in a system of moving gravitating bodies [4, 5].

2. GRAVITATIONAL SCREENING

In contrast to plasma or electrolyte, the screening of the Coulomb potential of a charge particle is presumably due to the presence of oppositely charged particles and takes place for both a moving test particle (dynamic screening) and a particle at rest (static Debye–Hückel screening). In contrast to this, the screening of the Newtonian potential of a selected test body in a system of gravitating bodies is possible only in the case of its motion among surrounding bodies.

In the model discussed below, the Galaxy is considered (with the dark matter ignored) as an equilibrium

Institute for Dynamics of Geospheres, Russian Academy of Sciences, Leninskiĭ pr. 38, Moscow, 117979 Russia

[1] The article was submitted by the authors in English.

1028-3358/01/4603-0180$21.00

gravitating system of stars having a Maxwellian distribution of their velocities:

$$f_0(\mathbf{v}) = \rho_0(2\pi\tilde{v}^2)^{-3/2}\exp\left\{-\frac{v^2}{2\tilde{v}^2}\right\}.$$

Here, ρ_0 is the density of stellar matter and $\tilde{v}$ is the variance for the velocities. The Sun is excluded from the entire system and considered as an additional gravitating body of mass $M_\odot$, which is inserted at the instant t_0 at the point $\mathbf{r}_0 = 0$ and then moves with constant velocity $\mathbf{u}$. Introduction of a test particle results in a perturbation $f_1(\mathbf{r}, \mathbf{v}, t)$ of the system, so its distribution function takes the form

$$f(\mathbf{r}, \mathbf{v}, t) = f_0(\mathbf{v}) + f_1(\mathbf{r}, \mathbf{v}, t).$$

Then, in the linear approximation in the perturbation, the system is described by the Vlasov equation:

$$\frac{\partial f_1(\mathbf{r}, \mathbf{v}, t)}{\partial t} + \mathbf{v}\frac{\partial f_1(\mathbf{r}, \mathbf{v}, t)}{\partial \mathbf{r}} + \nabla\Phi\frac{\partial f_0(\mathbf{r}, \mathbf{v}, t)}{\partial \mathbf{v}} = 0. \quad (1)$$

This is supplemented by the Poisson equation for the effective potential:

$$\nabla^2\Phi = -4\pi Gm\int d^3v\, f_1(\mathbf{r}, \mathbf{v}, t) - 4\pi GM_\odot\delta(\mathbf{r} - \mathbf{u}(t - t_0)). \quad (2)$$

We are interested in the steady-state behavior of the gravitating system. This implies, physically, that the motion is considered at times $t > \tau$, where $\tau = \dfrac{1}{\sqrt{4\pi G\rho_0}}$ is the characteristic relaxation time. For our Galaxy (where $\rho_0 = 1.9 \times 10^{-2}$ g/cm^3), it is on the order of 10^7 years, i.e., much less than the time of existence of the solar system (in the opposite case, transition processes would be allowed for). To exclude transition processes, we put $t_0 \longrightarrow -\infty$. Then, the formal solution to Eqs. (1) and (2) is

$$\nabla^2\Phi = 4\pi Gm\int d^3v\int_{-\infty}^{t} dt'\nabla\Phi(\mathbf{r} - \mathbf{v}(t - t'), t')\frac{\partial f_0}{\partial \mathbf{v}} - 4\pi GM_\odot\delta(\mathbf{r} - \mathbf{u}t), \quad (3)$$

or, in the Fourier transforms,

$$\left[k^2 - 4\pi Gm\int d^3v\frac{\mathbf{k}\dfrac{\partial f_0}{\partial \mathbf{v}}}{\omega - \mathbf{kv} + i\nu}\right]\Phi(\mathbf{k}, \omega) = 8\pi^2GM_\odot\delta(\omega - \mathbf{ku}). \quad (4)$$

Whence it follows that

$$\Phi(\mathbf{k}, \omega) = \frac{8\pi^2GM_\odot}{k^2\varepsilon_g(\mathbf{k}, \omega)}\delta(\omega - \mathbf{ku}). \quad (5)$$

Here,

$$\varepsilon_g(\mathbf{k}, \omega) = 1 - \frac{4\pi G}{k^2}\int d^3v\frac{\mathbf{k}\dfrac{\partial f_0}{\partial \mathbf{v}}}{\omega - \mathbf{kv} + i\nu} \quad (6)$$

is the gravitational permittivity of the system. This function determines the response of the gravitating system to a gravitational disturbance. The concept of gravitational permittivity is well-known in the theory of gravitating systems (see, e.g., [6–8]). Zeroes of this function define a dispersion equation whose complex roots determine the spectrum of elementary excitations in a gravitational system.

An infinitesimal imaginary quantity $i\nu$ is added to the frequency ω in Eqs. (4) and (6). This corresponds to introduction, into the right-hand side of the Vlasov equation (1), of the term $-\nu f_1$ related to the Boltzmann collision integral. This addition ensures the selection of retarded solutions and allows for the Landau damping in collisionless plasma. For gravitating systems, this problem was discussed in [5, 7, 8]. Then, the permittivity $\varepsilon_g(\mathbf{k}, \omega)$ becomes a complex-valued function and can be written out as

$$\varepsilon_g(\mathbf{k}, \omega) = 1 - \frac{k_J^2}{k^2}W(w), \quad w = \frac{\omega}{\sqrt{2}k\tilde{v}}, \quad (7)$$

where $k_J = \left(\dfrac{4\pi G\rho_0}{\tilde{v}^2}\right)^{1/2}$ is the Jeans wave-number and

$$W(w) = 1 + i(\pi)^{1/2}w\exp\{-z^2\}\mathrm{erfc}(-iw).$$

To calculate the inverse Fourier transform

$$\Phi(\mathbf{r}, t) = \frac{1}{(2\pi)^4}\int_{-\infty}^{\infty} d\omega\int d^3k e^{-i(\omega t - \mathbf{kr})}\Phi(\mathbf{k}, \omega), \quad (8)$$

we put the axis z parallel to $\mathbf{u}$ and introduce the dimensionless variables $Z = (z - ut)k_J$, $X = xk_J$, $\mathbf{K} = \dfrac{\mathbf{k}}{k_J}$, and $V = \dfrac{u}{\sqrt{2}\tilde{v}}$. Taking into account cylindrical symmetry, we arrive at the equation

$$\Phi(\mathbf{r}, t) = \frac{GM_\odot k_J}{2\pi^2}\int_{-\pi}^{\pi} d\phi\int_0^{\pi} d\theta\int dK K^2 \times \sin\theta\frac{\exp\{iK(X\sin\theta\cos\phi + Z\cos\theta)\}}{K^2 - W(V\cos\theta)} = \frac{GM_\odot k_J}{(X^2 + Z^2)^{1/2}}\left[1 + (X^2 + Z^2)^{\frac{1}{2}}I(X, Z, V)\right], \quad (9)$$

where

$$I(X, Z, V) = \frac{1}{2\pi^2}\int_{-\pi}^{\pi} d\phi \int_{0}^{\pi} d\theta \int dK W(V\cos\theta) \times \sin\theta \frac{\exp\{iK(X\sin\theta\cos\phi + Z\cos\theta)\}}{K^2 - W(V\cos\theta)}. \quad (10)$$

This integral determines the deviation of the effective potential from the Newtonian potential described by the first term in the brackets of Eq. (9). After taking the Cauchy integral over K, we have

$$I(X, Z, V) = \frac{1}{4\pi^2}\int_{-\pi}^{\pi} d\phi \int_{0}^{\pi} d\theta \sin\theta \sqrt{-W} \times [-2i\sinh(\Delta\sqrt{-W})\mathrm{Ci}(-i\Delta\sqrt{-W}) + \cosh(\Delta\sqrt{-W})(\pi + 2i\mathrm{Shi}(\Delta\sqrt{-W}))]. \quad (11)$$

Here, $\Delta = X\sin\theta\cos\phi + Z\cos\theta$. The numerical integration of (11) for arbitrary parameters V and Z is quite easy. For the problem under discussion of planetary motion in the solar system, we can restrict ourselves to certain values of these parameters.

For stellar (barionic) matter in the Galaxy, we have $k_J \simeq 2.5 \times 10^{-21}$ cm^{-1}. Thus, the values of Z and X are estimated as $10^{-9} < |Z| < 10^{-6}$, $10^{-9} < |X| < 10^{-6}$ for the planets of the solar system whose orbits are at distances of $10^{12} < r < 10^{15}$ cm from the Sun. Therefore, when analyzing the effective potential of the Sun within the solar system, the values X and Z can be regarded as small parameters. To estimate effective potential (9) for the linear approximation in these parameters, the integral $I(X, Z, V)$ should be evaluated for the zeroth approximation in Δ:

$$I(X, Z, V) = -\frac{1}{4\pi^2}\int_{-\pi}^{\pi} d\phi \int_{0}^{\pi} d\theta \sin\theta \sqrt{-W}[\pi + o(\Delta)]. \quad (12)$$

Because the peculiar velocity of the Sun in the Galaxy is 1.95×10^5 cm s^{-1} and the velocity variance in the Galaxy is $\tilde{v} \simeq 1.55 \times 10^6$ cm s^{-1}, we set $V = 1$.

The calculated value of integral (12) for $V = 1$ is $I = -0.3677$. While increasing V from 0.3 to 3.0, the value I decreases from –0.3 to –0.47.

3. CORRECTION TO THE EPHEMERIS TIME

According to Eq. (9) and the numerical estimate of I obtained for integral (12), the energy of the renormalized gravitational interaction between the Earth and the Sun can be represented as

$$U(R) = U_0 + \delta U, \quad U_0 = -\frac{A}{r}, \quad \delta U = A\gamma, \quad A = GM_\odot M_\oplus, \quad \gamma = -Ik_J. \quad (13)$$

Thus, in this approximation, the correction δU to the Newtonian interaction energy is a constant value independent of r.

Before the influence of this correction on the Keplerian period of the revolution of the Earth has been considered, we should verify whether the finite trajectory of the Earth around the Sun remains closed.

In the classical two-body problem (after reducing it to the central-force problem), the angle $\Delta\varphi$ of the perihelion precession (see, e.g., [9]) is given by

$$\Delta\varphi = 2\int_{r_{\min}}^{r_{\max}} \frac{\frac{M}{r^2}dr}{\sqrt{2m(E - U_0 - \delta U) - \frac{M^2}{r^2}}}. \quad (14)$$

Here, $r_{\max}$ and $r_{\min}$ are the maximum and minimum values of the radius vector r, respectively; $m = \frac{M_\odot M_\oplus}{M_\odot + M_\oplus}$ is the reduced mass;

$$M = mr^2\dot{\varphi}; \text{ and } E = \frac{m\dot{r}^2}{2} + \frac{M^2}{2mr^2} + U.$$

The last two quantities, the moment M and energy E, are integrals of motion.

For a trajectory of finite motion to be closed, the precession angle must have the form $\Delta\varphi = \frac{2\pi k}{n}$, where k and n are integers. For the Newtonian potential, this condition is satisfied ($\Delta\varphi = 2\pi$).

In the expansion of the integrand in (14) in powers of δU, the zeroth-order term yields 2π, while the first-order term determines an additional precession of the perihelion:

$$\delta\varphi = \frac{\partial}{\partial M}\left(\frac{2m}{M}\int_0^\pi r^2 \delta U d\varphi\right)_0. \quad (15)$$

Here, the expression within the parentheses must be estimated for the unperturbed motion and can be expressed in terms of the parameter p and eccentricity e of an elliptic closed orbit:

$$r = \frac{p}{1 + e\cos\varphi}, \quad p = \frac{M^2}{mA}, \quad e = \sqrt{1 + \frac{2EM^2}{mA^2}}. \quad (16)$$

Then,

$$\delta\varphi = \frac{2\gamma}{mA}\frac{\partial}{\partial M}\left(M^3\int_0^\pi \frac{d\varphi}{(1+e\cos\varphi)^2}\right)$$

$$= \frac{2\gamma}{mA}\frac{\partial}{\partial M}\left(\frac{M^3\pi}{(1-e^2)^{3/2}}\right) = \frac{2\gamma\pi}{mA}\frac{\partial}{\partial M}\left(\frac{M^3}{\left(\frac{2|E|M^2}{mA^2}\right)^{3/2}}\right) = 0.$$

Therefore, the perturbed trajectory remains closed.

We now estimate the corresponding correction to the revolution period T. It is easy to prove that all the mathematical calculations leading to the third Kepler law for the undisturbed Newtonian potential,

$$T_0 = \pi A\sqrt{\frac{m}{2|E_0|^3}}, \quad E_0 = \frac{m\dot{r}^2}{2} + \frac{M^2}{2mr^2} + U_0(r), \quad (17)$$

also remain valid for the change of E_0 by $E = E_0 + \delta U$. As a result, we have

$$T = \pi A\sqrt{\frac{m}{-2(E_0+\delta U)^3}} \simeq \pi A m^{1/2}(-2E_0)^{-3/2} \times\left(1-\frac{3A\gamma}{2E_0}\right) = T_0\left(1+\frac{3A\gamma}{2|E_0|}\right); \quad (18)$$

hence,

$$\frac{T-T_0}{T_0} = \frac{3A\gamma}{2|E_0|}. \quad (19)$$

Using the equality

$$|E_0| = \frac{mA^2}{2M^2}(1-e^2) \quad (20)$$

and the numerical values ($e = 0.017$, $M_\odot = 1.99\times 10^{33}$ g, $M_\oplus = 5.98\times 10^{27}$ g, $I = -0.3677$, with an effect of the dark matter ignored), we obtain

$$\frac{T-T_0}{T_0} = -\frac{3Ik_J R^4\dot{\varphi}^2}{GM_\odot} = 3.9\times 10^{-8} \times\left[\frac{I}{-0.3677}\right]\left[\frac{G}{6.7\times 10^{-8}}\right]^{-1/2}\left[\frac{\rho_0}{1.9\times 10^{-23}}\right]^{1/2} \times\left[\frac{\tilde{\nu}}{1.55\times 10^6}\right]^{-1}\left[\frac{M_\odot}{2\times 10^{33}}\right]^{-1}\left[\frac{R}{1.5\times 10^{13}}\right]^4\left[\frac{\dot{\varphi}}{2.1\times 10^{-7}}\right]^2. \quad (21)$$

This estimate corresponds to $\Delta T_\oplus \simeq 1$ s year^{-1} (1 year $T_\oplus \simeq 3.15\times 10^7$ s).

Thus, the effect of screening of the Newtonian potential results in an increase in the ET year by about 1 s. This correction compensates (by an order of magnitude) for the systematic difference $\overline{\Delta T} = \overline{\mathrm{UT}-\mathrm{ET}} = \overline{\mathrm{UT}} - \mathrm{TAI} \simeq 0.8$ s.

In this case, a question may arise on the corresponding renormalization of the TAI scale since it was initially determined just via the ephemeris time.

REFERENCES

1. W. Markowitz, R. Hall, L. Essen, and J. V. L. Parry, Phys. Rev. Lett. **1**, 105 (1958).
2. W. H. Munk, in *The Earth–Moon System*, Ed. by B. G. Mardsen and A. W. Cameron (Plenum Press, New York, 1966), pp. 52–54.
3. J. Lestrade *et al*., *High-Precision Earth Rotation and Earth–Moon Dynamics* (D. Reidel Publishing Co., Dordrecht, 1982), pp. 217–225.
4. A. V. Vityazev, A. G. Bashkirov, and Yu. A. Kukharenko, Dokl. Akad. Nauk **334**, 639 (1994).
5. A. G. Bashkirov and A. V. Vityazev, Astrophys. J. **497**, 10 (1998).
6. L. S. Marochnic, Astron. Zh. **44**, 1087 (1967) [Sov. Astron. **11**, 873 (1968)].
7. J. Binney and S. Tremaine, *Galactic Dynamics* (Princeton, 1987).
8. W. C. Saslaw, *Gravitational Physics of Stellar and Galactic Systems* (Cambridge Univ. Press, Cambridge, 1985).
9. L. D. Landau and E. M. Lifshitz, *Classical Mechanics* (Fizmatgiz, Moscow, 1965; Pergamon Press, New York, 1965).

Doklady Physics, Vol. 46, No. 3, 2001, pp. 184–189. From Doklady Akademii Nauk, Vol. 377, No. 1, 2001, pp. 44–49.

MECHANICS

Overlapping of Frequency Curves in Nonconservative Systems[1]

O. N. Kirillov and A. P. Seyranian

Presented by Academician S.S. Grigoryan July 14, 2000

Received July 18, 2000

The overlapping of characteristic curves often arises in nonconservative systems, depending on the parameters involved [1–4]. The characteristic curves describe the eigenvalues of an operator for a system as functions of a chosen parameter, for example, a parameter of a nonconservative load. The phenomenon consists in the fact that, when varying parameters, the characteristic curves come closer together, merge at a point, and then overlap, forming a "bubble of instability". In this case, the overlapping is accompanied by a discontinuity of the critical load.

In this paper, explicit formulas describing the overlapping in two-parametric nonconservative systems are derived. These formulas use information on a system only at the merging point and allow us to perform qualitative, as well as quantitative, analyses for the behavior of the characteristic curves in the vicinity of this point. A quadratic approximation of the flutter boundary is also obtained. It is shown that the features of the characteristic curves are related to convexity properties of the flutter instability boundary.

1. We consider a linear autonomous nonconservative mechanical system without damping and gyroscopic forces, which is described by the equation

$$\mathbf{M}\ddot{\mathbf{q}} + \mathbf{C}\mathbf{q} = \mathbf{0}. \tag{1}$$

Here, $\mathbf{M} = \mathbf{M}^{\mathrm{T}} > 0$ and $\mathbf{C} \neq \mathbf{C}^{\mathrm{T}}$ are real $m \times m$ matrices of mass and stiffness, $\mathbf{q}$ is the m-dimensional vector of generalized coordinates, and the dots stand for the differentiation with respect to time. System (1) is usually referred to as a circulatory system [5, 6]. Let ω be the frequency of oscillations. Substituting $\mathbf{q} = \mathbf{u}\exp(i\omega t)$ into (1) and introducing the notation $\mathbf{A} = \mathbf{M}^{-1}\mathbf{C}$ and $\lambda = \omega^2$, we arrive at an eigenvalue problem:

$$\mathbf{A}\mathbf{u} = \lambda\mathbf{u}. \tag{2}$$

System (1) is stable if all the eigenvalues of problem (2) are positive and semisimple. If all the eigenvalues λ are real and some of them negative, then system (1) is statically unstable (the case of divergence). If at least one eigenvalue λ is complex-valued, vibrational instability (i.e., flutter) occurs.

2. We suppose that the matrix $\mathbf{A}$ smoothly depends on the two-dimensional vector $\mathbf{p} = (p_1, p_2)$ of real-valued parameters. It is known [7–9] that, in general, the stability boundary of a two-parametric circulatory system consists of smooth curves on which the matrix $\mathbf{A}$ has either a simple zero eigenvalue or a positive double eigenvalue with a Jordan chain of the length of 2. At individual points of the stability boundary, singularities of two types (namely, cusps and nodes) are possible. These singularities correspond to matrices with a more complicated Jordan structure [7, 9].

We first consider a point $\mathbf{p} = \mathbf{p}_0$ on the stability boundary on which the matrix $\mathbf{A}_0 = \mathbf{A}(\mathbf{p}_0)$ has a positive double eigenvalue λ_0 with a Jordan chain of the length of 2. At this point, the eigenvalue λ_0 corresponds to an eigenvector $\mathbf{u}_0$, associated vector $\mathbf{u}_1$, adjoint eigenvector $\mathbf{v}_0$, and adjoint associated vector $\mathbf{v}_1$, which are governed by the equations

$$(\mathbf{A}_0 - \lambda_0\mathbf{I})\mathbf{u}_0 = \mathbf{0}, \quad (\mathbf{A}_0 - \lambda_0\mathbf{I})\mathbf{u}_1 = \mathbf{u}_0, \tag{3}$$

$$(\mathbf{A}_0^{\mathrm{T}} - \lambda_0\mathbf{I})\mathbf{v}_0 = \mathbf{0}, \quad (\mathbf{A}_0^{\mathrm{T}} - \lambda_0\mathbf{I})\mathbf{v}_1 = \mathbf{v}_0, \tag{4}$$

where $\mathbf{I}$ is the identity matrix. The vectors $\mathbf{u}_0$, $\mathbf{u}_1$, $\mathbf{v}_0$, and $\mathbf{v}_1$ are related by conditions of orthogonality and normalization:

$$(\mathbf{u}_0, \mathbf{v}_0) = 0, \quad (\mathbf{u}_1, \mathbf{v}_0) \equiv (\mathbf{u}_0, \mathbf{v}_1) = 1. \tag{5}$$

The parentheses in (5) stand for the Hermitian scalar product $(\mathbf{a}, \mathbf{b}) = \sum_{i=1}^{m} a_i\bar{b}_i$ of the vectors $\mathbf{a}, \mathbf{b} \in C^m$.

We consider smooth variations $\mathbf{p}(\varepsilon) = \mathbf{p}_0 + \varepsilon\mathbf{e} + \varepsilon^2\mathbf{d}$ of the parametric vector in the vicinity of the point $\mathbf{p}_0$. Here, $\mathbf{e}$ and $\mathbf{d} \in R^2$ are variation vectors, $|\mathbf{e}| = 1$, and

Institute of Mechanics, Moscow State University, Michurinskiĭ pr. 1, Moscow, 117192 Russia

[1] This article was submitted by the authors in English.

1028-3358/01/4603-0184$21.00

$\varepsilon > 0$ is a small parameter. As a result of this perturbation, the matrix $\mathbf{A}_0$ takes the increment

$$\mathbf{A}(\mathbf{p}_0 + \varepsilon\mathbf{e} + \varepsilon^2\mathbf{d}) = \mathbf{A}_0 + \varepsilon\mathbf{A}_1 + \varepsilon^2\mathbf{A}_2 + \ldots, \quad (6)$$

where matrices $\mathbf{A}_1$ and $\mathbf{A}_2$ are given by

$$\mathbf{A}_1 = \sum_{s=1}^{2} \frac{\partial \mathbf{A}}{\partial p_s} e_s,$$
$$\mathbf{A}_2 = \sum_{i=1}^{2} \frac{\partial \mathbf{A}}{\partial p_i} d_i + \frac{1}{2} \sum_{s,t=1}^{2} \frac{\partial^2 \mathbf{A}}{\partial p_s \partial p_t} e_s e_t. \quad (7)$$

The derivatives in (7) are taken at the point $\mathbf{p} = \mathbf{p}_0$.

Due to the variation of the vector of parameters, both the eigenvalue λ_0 and the corresponding eigenvector $\mathbf{u}_0$ also take increments. According to the perturbation theory of non-self-adjoint operators [10], in the case of a double eigenvalue with a Jordan chain of the length of 2, the expansions for the eigenvalue and eigenvector contain terms with fractional powers of the small parameter ε:

$$\lambda = \lambda_0 + \varepsilon^{1/2}\lambda_1 + \varepsilon\lambda_2 + \varepsilon^{3/2}\lambda_3 + \ldots,$$
$$\mathbf{u} = \mathbf{u}_0 + \varepsilon^{1/2}\mathbf{w}_1 + \varepsilon\mathbf{w}_2 + \varepsilon^{3/2}\mathbf{w}_3 + \ldots \quad (8)$$

Substituting expansions (6) and (8) into eigenvalue problem (2), we obtain equations for determining the perturbations of λ_0 and $\mathbf{u}_0$. For the first coefficient λ_1, we have

$$\lambda_1 = \pm\sqrt{(\mathbf{A}_1\mathbf{u}_0, \mathbf{v}_0)}. \quad (9)$$

Using expression (7) for the matrix $\mathbf{A}_1$, we introduce a vector $\mathbf{f}$ with the components

$$f^s = \left(\frac{\partial \mathbf{A}}{\partial p_s}\mathbf{u}_0, \mathbf{v}_0\right), \quad s = 1, 2. \quad (10)$$

As λ_0 is a real eigenvalue, the vector $\mathbf{f}$ is also real. With regard to (10), we obtain a formula describing the splitting of the double eigenvalue [9]:

$$\lambda = \lambda_0 \pm \sqrt{\varepsilon\langle \mathbf{f}, \mathbf{e}\rangle} + O(\varepsilon). \quad (11)$$

Here, $\langle \mathbf{a}, \mathbf{b}\rangle = \sum_{s=1}^{2} a_s b_s$ is the scalar product of the vectors $\mathbf{a}, \mathbf{b} \in R^2$ in the parameter space. Formula (11) is valid if the radicand is not zero. If $\langle \mathbf{f}, \mathbf{e}\rangle < 0$, then the double eigenvalue λ_0 splits into a complex-conjugate pair of eigenvalues (flutter instability). If $\langle \mathbf{f}, \mathbf{e}\rangle > 0$, two positive eigenvalues appear (stability). Therefore, the vector $\mathbf{f}$ is a normal to the stability boundary and lies in the stability domain (see Fig. 1a).

We now consider a degenerate case when

$$\langle \mathbf{f}, \mathbf{e}_* \rangle = 0. \quad (12)$$

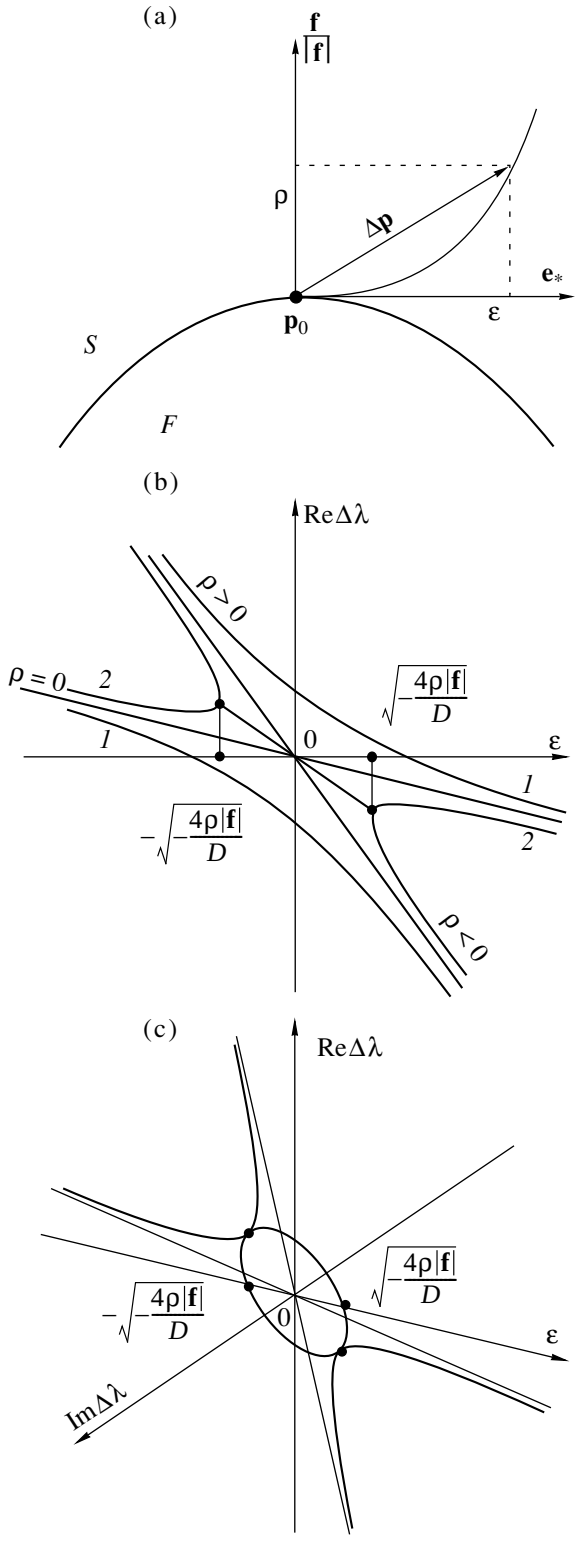

Fig. 1. Transformation of frequency curves near the flutter boundary.

This implies that the curves $\mathbf{p}(\varepsilon) = \mathbf{p}_0 + \varepsilon\mathbf{e}_* + \varepsilon^2\mathbf{d}$ tend to the tangents to the stability boundary as $\varepsilon \longrightarrow 0$. In this case, the terms with fractional powers disappear

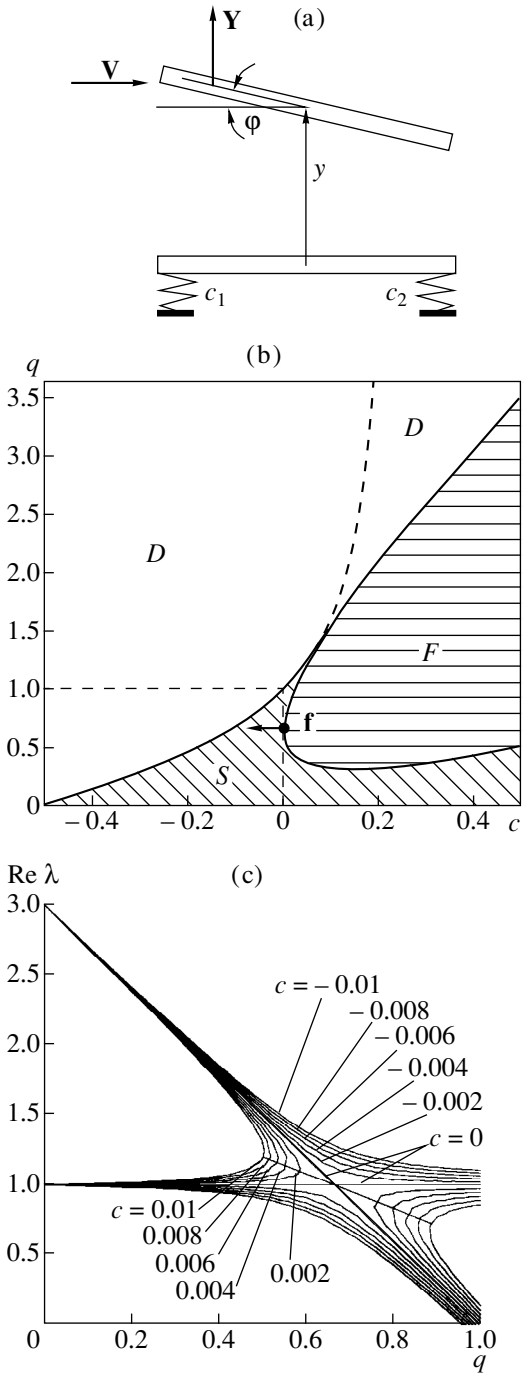

Fig. 2. Stability of vibrations for a plate in a gas flow.

in expansions (8) [10]:

$$\lambda = \lambda_0 + \varepsilon\lambda_2 + \varepsilon^2\lambda_4 + \ldots,$$
$$\mathbf{u} = \mathbf{u}_0 + \varepsilon\mathbf{w}_2 + \varepsilon^2\mathbf{w}_4 + \ldots \quad (13)$$

The coefficient λ_2 is a solution to the quadratic equation [9]

$$\lambda_2^2 + \lambda_2 a_1 + a_2 = 0 \quad (14)$$

with coefficients

$$a_1 = -(\mathbf{A}_1\mathbf{u}_0, \mathbf{v}_1) - (\mathbf{A}_1\mathbf{u}_1, \mathbf{v}_0),$$
$$a_2 = -(\mathbf{A}_2\mathbf{u}_0, \mathbf{v}_0) + (\mathbf{G}_0(\mathbf{A}_1\mathbf{u}_0), \mathbf{A}_1^T\mathbf{v}_0). \quad (15)$$

The operator $\mathbf{G}_0$, inverse to $\mathbf{A}_0 - \lambda_0\mathbf{I}$, is defined by the expressions

$$(\mathbf{A}_0 - \lambda_0\mathbf{I})\psi = \varphi \text{ and } \psi = \mathbf{G}_0\varphi,$$

where φ and $\psi \in C^m$ and the solvability condition $(\varphi, \mathbf{v}_0) = 0$ is assumed to be satisfied. In this case, the solvability condition has the form $(\mathbf{A}_1\mathbf{u}_0, \mathbf{v}_0) = 0$ and is valid for the degenerate directions given by (12) for the vector $\mathbf{e}$. Using expressions (7) for the matrices $\mathbf{A}_1$ and $\mathbf{A}_2$, the coefficients a_1 and a_2 can be written as

$$a_1 = \langle \mathbf{h}, \mathbf{e}_* \rangle, \quad a_2 = \langle \mathbf{H}\mathbf{e}_*, \mathbf{e}_* \rangle - \langle \mathbf{f}, \mathbf{d} \rangle, \quad (16)$$

where the real vector $\mathbf{h}$ and matrix $\mathbf{H}$ are defined by (15).

3. We substitute expressions (16) into Eq. (14) and multiply the result by ε^2. Introducing the notation $\Delta\lambda = \lambda_2\varepsilon$, we have

$$\Delta\lambda^2 + \varepsilon\langle \mathbf{h}, \mathbf{e}_* \rangle\Delta\lambda + \varepsilon^2\langle \mathbf{H}\mathbf{e}_*, \mathbf{e}_* \rangle = \varepsilon^2\langle \mathbf{f}, \mathbf{d} \rangle. \quad (17)$$

It is worth noting that no restrictions were imposed on the vector $\mathbf{d}$. It is convenient to set this vector collinear to the normal $\mathbf{f}$, i.e., to set $\mathbf{d} = \gamma\mathbf{f}$. Denoting $\rho = \gamma|\mathbf{f}|\varepsilon^2$, we see that ε and ρ are coordinates of the vector $\Delta\mathbf{p} = \mathbf{p} - \mathbf{p}_0$ in the orthonormalized basis of the vectors $\mathbf{e}_*$ and $\dfrac{\mathbf{f}}{|\mathbf{f}|}$, which are related by orthogonality condition (12). Indeed,

$$\Delta\mathbf{p} \equiv \varepsilon\mathbf{e}_* + \varepsilon^2\mathbf{d} = \varepsilon\mathbf{e}_* + \rho\frac{\mathbf{f}}{|\mathbf{f}|}.$$

Transforming the right-hand side of Eq. (17), we have

$$\varepsilon^2\langle \mathbf{f}, \mathbf{d} \rangle = \langle \mathbf{f}, \Delta\mathbf{p} \rangle = \rho|\mathbf{f}|. \quad (18)$$

Substituting (18) into (17), we arrive at

$$\Delta\lambda^2 + \varepsilon\langle \mathbf{h}, \mathbf{e}_* \rangle\Delta\lambda + \varepsilon^2\langle \mathbf{H}\mathbf{e}_*, \mathbf{e}_* \rangle = \rho|\mathbf{f}|. \quad (19)$$

This equation describes the splitting of the eigenvalue λ_0, which occurs due to varying the parameters ε and ρ near the stability boundary. In particular, the approximate equation of the stability boundary in the vicinity of the point $\mathbf{p} = \mathbf{p}_0$ follows from (19). Indeed, the boundary between the domains of stability and flutter consists of points that correspond to matrices containing positive double eigenvalues with a Jordan chain of the length of 2. Therefore, the discriminant of quadratic equation (19) has to be zero at the boundary

points. This condition leads to a quadratic approximation for the boundary in the local coordinates ε and ρ:

$$\rho = -\varepsilon^2 \frac{D}{4|\mathbf{f}|}, \tag{20}$$

$$D = \langle \mathbf{h}, \mathbf{e}_* \rangle^2 - 4\langle \mathbf{H}\mathbf{e}_*, \mathbf{e}_* \rangle. \tag{21}$$

Parabola (20) is convex either downward (if $D < 0$) or upward (if $D > 0$). It immediately follows from Eq. (19) that the flutter domain is defined by the inequality

$$\rho < -\varepsilon^2 \frac{D}{4|\mathbf{f}|}. \tag{22}$$

If the double eigenvalue λ_0 at the point $\mathbf{p}_0$ is assumed to be negative, then Eq. (20) describes the boundary between the domains of flutter and divergence and inequality (22) defines the flutter domain as before.

For any fixed value of ρ, Eq. (19) describes the behavior of two eigenvalues λ along a line parallel to the tangent to the boundary at the point $\mathbf{p}_0$. Changing the sign of the parameter ρ implies passage through the flutter boundary (see Fig. 1a). It is natural to expect that qualitative changes in the behavior of the frequency curves $\lambda(\varepsilon)$ would take place in this case. Equation (19) allows us to study the rearrangement of the frequency curves both qualitatively and quantitatively, using only information at the point $\mathbf{p} = \mathbf{p}_0$.

We take a perfect square from the left-hand side of (19) and study the cases of positive and negative values of D defined by (21):

$$\left(\Delta\lambda + \frac{1}{2}\varepsilon\langle \mathbf{h}, \mathbf{e}_* \rangle\right)^2 - \left(\frac{\varepsilon\sqrt{D}}{2}\right)^2 = \rho|\mathbf{f}|, \quad D > 0; \tag{23}$$

$$\left(\Delta\lambda + \frac{1}{2}\varepsilon\langle \mathbf{h}, \mathbf{e}_* \rangle\right)^2 + \left(\frac{\varepsilon\sqrt{-D}}{2}\right)^2 = \rho|\mathbf{f}|, \quad D < 0. \tag{24}$$

We then consider Eq. (23) corresponding to the convex flutter domain $D > 0$ (Fig. 1a). If $\rho > 0$, then, for any ε, the eigenvalues λ are real and placed on hyperbola *1* as shown in Fig. 1b. When the parameter ρ tends to zero, the branches of hyperbola *1* approach each other, so that for $\rho = 0$, the eigenvalues are on two real asymptotes:

$$\mathrm{Re}\Delta\lambda(\varepsilon) = -\frac{1}{2}\varepsilon(\langle \mathbf{h}, \mathbf{e}_* \rangle \pm \sqrt{D}).$$

If $\rho < 0$, the set of real solutions to Eq. (23) consists of two branches of adjacent hyperbola *2* in Fig. 1b; however, for ε satisfying the inequality $\varepsilon^2 < -\frac{4\rho|\mathbf{f}|}{D}$, the eigenvalues λ are complex-valued and belong to an ellipse (a so-called instability bubble). The real and imaginary components of the bubble are governed, respectively, by the equations

$$\mathrm{Re}\Delta\lambda = -\frac{\varepsilon}{2}\langle \mathbf{h}, \mathbf{e}_* \rangle, \tag{25}$$

$$(\mathrm{Im}\Delta\lambda)^2 + \left(\frac{\varepsilon\sqrt{D}}{2}\right)^2 = -\rho|\mathbf{f}|. \tag{26}$$

The ellipse and two branches of hyperbola *2* have common points when $\varepsilon_{1,2} = \pm\sqrt{-\frac{4\rho|\mathbf{f}|}{D}}$ (Fig. 1c), at which the matrix $\mathbf{A}$ has the double real eigenvalues

$$\lambda_{1,2} = \lambda_0 \mp \frac{1}{2}\langle \mathbf{h}, \mathbf{e}_* \rangle\sqrt{-\frac{4\rho|\mathbf{f}|}{D}}.$$

Hyperbola (23) and ellipses (25) and (26) lie on the orthogonal planes since the real component of the ellipse is given by a straight line (Fig. 1b). Therefore, when varying the parameter ε, the eigenvalues bifurcate in the vicinity of the points ε_1 and ε_2. Namely, two eigenvalues, moving on a plane, merge and then come out of the plane in the direction orthogonal to it. Such a behavior of the eigenvalues is referred to as a strong interaction and is typical for passage through the flutter boundary [8]. It is worth noting that the inequality determining the instability bubble exactly coincides with the approximation of flutter domain (22). Thereby, the overlapping is closely related to the convexity properties of the flutter domain.

We now consider the case $D < 0$ when the overlapping of the frequency curves is described by the families of ellipses (24). There are no real solutions for $\Delta\lambda(\varepsilon)$ if $\rho < 0$ (the case of flutter). At $\rho = 0$, the set of real solutions consists of an isolated point. If $\rho > 0$, then the set of real solutions $\Delta\lambda(\varepsilon)$ is ellipse (24), whose boundary is defined by the inequality $\varepsilon^2 < \frac{4\rho|\mathbf{f}|}{(-D)}$. It is easy to see that such a behavior corresponds to concave flutter domain (22).

Remark 1. Similarly, using variations along the curves $\mathbf{p}(\varepsilon) = \mathbf{p}_0 + \varepsilon\mathbf{e} + \varepsilon^2\mathbf{d}$, we can analyze the overlapping of the frequency curves near the boundary between the domains of stability and divergence.

Remark 2. The basic equations describing the bifurcations of eigenvalues, (11) and (17), and the overlapping of frequency curves, (23) and (24), are also valid for the linear differential operators $\mathbf{A}$ under homogeneous linear boundary conditions, depending on the parameters. The difference is that the vectors $\mathbf{f}$ and $\mathbf{h}$ and matrix $\mathbf{H}$ are defined through eigenfunctions and associated functions of the operator and through the derivatives of both the differential expression and the boundary forms with respect to parameters.

4. As an example, we consider a simple problem of stability for a rigid plate in an incident gas flow [11]. The plate is fixed by two elastic supports having stiffness coefficients c_1 and c_2 per unit length and has two

degrees of freedom: the vertical displacement y and the angle φ of deflection (see Fig. 2a). Small vibrations of the plate are described by the following equations in dimensionless variables [9, 11]:

$$\begin{pmatrix} \ddot{y} \\ \ddot{\varphi} \end{pmatrix} + \mathbf{A}\begin{pmatrix} y \\ \varphi \end{pmatrix} = 0, \quad \mathbf{A} = \begin{bmatrix} 1 & c-q \\ 12c & 3-3q \end{bmatrix}. \quad (27)$$

Here, $q = \frac{1}{2} c_y^a \rho v^2 (c_1 + c_2)^{-1}$ is the load parameter proportional to the dynamic pressure of the flow and $c = \frac{1}{2}(c_1 - c_2)(c_1 + c_2)^{-1}$ is the parameter characterizing the relation between the stiffness coefficients. Thus, circulatory system (27) depends on the vector of parameters $\mathbf{p} = (c, q)$. It follows from physical reasons that $q \geq 0$ and $-0.5 \leq c \leq 0.5$.

Seeking the solution to Eq. (27) in the form $\begin{pmatrix} y \\ \varphi \end{pmatrix} = \mathbf{u}e^{i\omega\tau}$, we arrive at eigenvalue problem (2). With $\lambda = \omega^2$, the corresponding characteristic equation has the form

$$\lambda^2 + (3q-4)\lambda + 12cq - 3q - 12c^2 + 3 = 0. \quad (28)$$

Equations of the curves subdividing the plane of the parameters c and q into the domains of stability, flutter, and divergence follow directly from (28) (see Fig. 2b):

$$q_d(c) = \frac{1-4c^2}{1-4c}, \qquad q_f(c) = \frac{2}{3}(1 + 4c \pm 2\sqrt{c(c+2)}). \quad (29)$$

For the point $\left(c = 0, q = \frac{2}{3}\right)$ on the boundary between the domains of stability and flutter, which corresponds to the double eigenvalue $\lambda = 1$ (see Fig. 2b), characteristic equation (28) can be easily transformed into

$$\left(\lambda - 1 + \frac{3}{2}q - 1\right)^2 - \left(-4c + \frac{3}{2}q - 1\right)^2 = -8c - 4c^2. \quad (30)$$

For $c = 0$, Eq. (30) has two solutions:

$$\lambda = 1, \quad \lambda = 3 - 3q. \quad (31)$$

The two lines (31) intersect one another at the point $\left(q = \frac{2}{3}, \lambda = 1\right)$. If $c \neq 0$, then Eq. (30) describes a family of hyperbolas with asymptotes (31). For small $c < 0$ and $0 \leq q \leq 1$, the solutions $\lambda(q)$ to Eq. (30) belong to the real plane. One of the two eigenvalues remains positive for any q, while another eigenvalue changes its sign at a certain $q_d < 1$ (see Figs. 2b, 2c). Thus, for $c < 0$ and sufficiently large q, system (27) loses its static stability (the case of divergence). Changing the sign of the parameter c results in a transformation of the frequency curves, which is accompanied by the origination of a region of complex-valued eigenvalues. In this case, the system loses its stability at the values of q_f, such that two positive eigenvalues λ merge to form a double eigenvalue with a Jordan chain of the length of 2 (flutter).

We now show that Eq. (30) can be approximated by formula (23), whose coefficients are calculated by using only information on the system at the point $\mathbf{p}_0 = \left(0, \frac{2}{3}\right)$. The eigenvectors and associated vectors of the double eigenvalue $\lambda = 1$ are

$$\mathbf{u}_0 = \begin{pmatrix} 1 \\ 0 \end{pmatrix}, \quad \mathbf{v}_0 = \begin{pmatrix} 0 \\ -2/3 \end{pmatrix}, \qquad \mathbf{u}_1 = \begin{pmatrix} 0 \\ -3/2 \end{pmatrix}, \quad \mathbf{v}_1 = \begin{pmatrix} 1 \\ 0 \end{pmatrix}. \quad (32)$$

Formulas (10) and (12) determine the vector $\mathbf{f}$ normal to the flutter boundary at the point $\mathbf{p}_0 = \left(0, \frac{2}{3}\right)$ and, therefore, the tangent vector $\mathbf{e}_*$:

$$\mathbf{f} = \begin{pmatrix} -8 \\ 0 \end{pmatrix}, \quad \mathbf{e}_* = \begin{pmatrix} 0 \\ 1 \end{pmatrix}. \quad (33)$$

Finding the vector $\mathbf{h}$ and matrix $\mathbf{H}$ by formulas (15) and (16), with regard to expression (21), we obtain that $\langle \mathbf{h}, \mathbf{e}_* \rangle = 3$, $D = 9$, and the variation vector is $\Delta\mathbf{p} = \left(c, q - \frac{2}{3}\right)$. Thus, the parameter ρ in Eqs. (23) and (24) is $\frac{\langle \mathbf{f}, \Delta\mathbf{p} \rangle}{|\mathbf{f}|} = -c$. As $D > 0$, the transformation of the frequency curves is described by Eq. (23), which in this case takes the form

$$\left(\lambda - 1 + \frac{3}{2}q - 1\right)^2 - \left(\frac{3}{2}q - 1\right)^2 = -8c. \quad (34)$$

Comparing exact equation (30) with its approximation (34), we see that the asymptotes $\lambda = 1$ and $\lambda = 3 - 3q$ coincide completely in both equations, with the approximations of the frequency curves being rather good for small values of parameter c. The quadratic approximation of the flutter domain in the vicinity of the point $\mathbf{p}_0 = \left(0, \frac{2}{3}\right)$ is given by formula (22):

$$c > \frac{9}{32}\left(q - \frac{2}{3}\right)^2. \quad (35)$$

Approximation (35) implies that the flutter domain is convex (see Fig. 2b), and it is in good agreement with the exact expression $q_f(c)$ for flutter boundary (29).

REFERENCES

1. J. L. Claudon, J. Mech. **14**, 531 (1975).
2. M. Hanaoka and K. Washizu, Comput. Struct. **11**, 473 (1980).
3. A. N. Kounadis and J. T. Katsikadelis, Int. J. Solids Struct. **16**, 375 (1980).
4. M. A. Langthjem and Y. Sugiyama, J. Sound Vib. **226**, 1 (1999).
5. H. Ziegler, *Principles of Structural Stability* (Blaisdell, Waltham, Mass., 1968).
6. V. V. Bolotin, *Nonconservative Problems in Theory of Elastic Stability* (Pergamon Press, Oxford, 1963).
7. V. I. Arnold, *Geometrical Methods in the Theory of Ordinary Differential Equations* (Springer-Verlag, New York and Berlin, 1983).
8. A. P. Seyranian, Izv. Ross. Acad. Nauk, Mekh. Tverd. Tela **29** (1), 142 (1994).
9. O. N. Kirillov and A. P. Seyranian, *On the Stability Boundaries of Circulatory Systems* (Moscow State Univ., Inst. of Mechanics, 1999, Preprint No. 51-99).
10. M. I. Vishik and L. A. Lyusternik, Russ. Math. Surveys **15** (3), 3 (1960).
11. Y. G. Panovko and I. I. Gubanova, *Stability and Oscillations of Elastic Systems* (Consultants Bureau, New York, 1965).

Doklady Physics, Vol. 46, No. 3, 2001, pp. 190–194. Translated from Doklady Akademii Nauk, Vol. 377, No. 1, 2001, pp. 50–54.

MECHANICS

The Structure of a Rarefaction Wave in Gas Suspension

A. V. Fedorov and Corresponding Member of the RAS V. M. Fomin

Received April 7, 2000

In [1], the problem of decaying a particular type of an arbitrary discontinuity in a gas–solid-particle mixture was numerically investigated provided that the high-pressure chamber of a shock tube was filled with a gas suspension at a high pressure. The rarefaction wave propagating into the gas suspension was the principal element of flow in the high-pressure chamber. It was numerically shown that the rarefaction-wave leading edge propagates with a velocity that approaches the equilibrium sound velocity in the course of the process development. It is of interest to analytically investigate the problem on the rarefaction-wave structure in the gas suspension. Below, we find, in particular, an exact value of the propagation velocity for the leading edge of the rarefaction wave and other parameters of the mixture flow at small and large times of the development of this process.

1. PRINCIPAL EQUATIONS AND THE PHYSICOMATHEMATICAL FORMULATION OF THE PROBLEM

We consider a channel with a mixture of gas and fine particles under high pressure. At the initial moment of time, the diaphragm separating the gas suspension and the atmospheric air collapses and the mixture outflows into the ambient medium. In this case, the channel cut collapses and propagates to the right into the high-pressure region. A similar problem was analyzed previously in the mechanics as applied to problems on disastrous ruptures of pipelines. Our purpose is to calculate the mixture parameters in the channel as functions of time. We study this problem within the framework of the model for isothermal gas-suspension flow. This model involves conservation equations for the mass and momentum of each phase:

$$\mathbf{E}\partial_t\Phi + \mathbf{B}\partial_x\Phi = \Psi. \qquad (1)$$

Here, $\Phi(\rho_1, u_1, \rho_2, u_2)$ and $\Psi(0, f_0, -f)$ are the solution vector function and the vector column, respectively; $f = \dfrac{\rho_2(u_2 - u_1)}{\tau}$ is the viscous-friction force between the phases, which is determined by a standard method; and τ is the relaxation time. Furthermore, $\rho_i = m_i\rho_{ii}$ is the mean density; m_i is the volume concentration; ρ_{ii} is the true density; u_i is the velocity of the corresponding phase; p is the pressure, which is common for the mixture as a whole; and the indices $i = 1, 2$ correspond to the gas and the particles, respectively. The equation of state for the mixture is written in the form

$$p = a_0^2\frac{\rho_1}{1 - \rho_2 r} = p(\rho_1, \rho_2),$$

where a_0 is the isothermal sound velocity and $\rho_{22} = r =$ const is the actual density of the second phase. We close (1) by the basic equality of mechanics of heterogeneous media:

$$m_1 + m_2 = 1. \qquad (1')$$

In Eq. (1), **E** is the identity matrix and the matrix **B** (with the notation: $\partial_{\rho_i} p = p_{\rho_i}$) is

$$\mathbf{B} = \begin{pmatrix} u_1 & \rho_1 & 0 & 0 \\ \dfrac{m_1}{\rho_1}p_{\rho_1} & u_1 & \dfrac{m_1}{\rho_1}p_{\rho_2} & 0 \\ 0 & 0 & u_2 & \rho_2 \\ \dfrac{m_2}{\rho_2}p_{\rho_1} & 0 & \dfrac{m_2}{\rho_2}p_{\rho_2} & u_2 \end{pmatrix}.$$

The set of Eqs. (1) and (1') is closed and invariant with respect to the Galilean transformations $u_i = u_i - D$ and $x = x - Dt$. Here, D is the velocity of motion for the left-hand boundary of the one-dimensional channel.

2. SOLVING EQUATIONS OF HETEROGENEOUS-MEDIUM MECHANICS FOR SMALL TIMES OF PROCESS DEVELOPMENT

2.1. Derivation of the set of ordinary differential equations for the zero-order and first approximations. We seek the solution to Eqs. (1) and (1') in the form $\Phi = \Phi_0(\xi) + t\Phi_1(\xi)$, where $\xi = \dfrac{x}{t}$ is the self-simi-

Institute of Theoretical and Applied Mechanics, Siberian Division, Russian Academy of Sciences, Novosibirsk, Russia

1028-3358/01/4603-0190$21.00

lar variable. Making the corresponding change of variables, we obtain the set of partial differential equations in the independent variables (ξ, t):

$$\begin{gathered}(u_i-\xi)\partial_\xi\rho_i + t\partial_t\rho_i + \rho_i\partial_\xi u_i = 0,\\ (u_i-\xi)\rho_i\partial_\xi u_i + t\rho_i\partial_t u_i + m_i\partial_\xi p = tf(-1)^{i+1}, \quad (2)\\ i = 1, 2.\end{gathered}$$

After substituting the linear representation of the solution and dividing the set into two subsets at t^0 and t, we obtain the desired sets of ordinary differential equations for the functions in the zero-order approximation:

$$\begin{gathered}(u_{i0}-\xi)d_\xi\rho_{i0} + \rho_{i0}d_\xi u_{i0} = 0,\\ (u_{i0}-\xi)\rho_{i0}d_\xi u_{i0} + m_{i0}(\partial_{\rho_{10}}p d_\xi\rho_{10} + \partial_{\rho_{20}}p d_\xi\rho_{20}) = 0;\end{gathered} \quad (3)$$

and, in the first approximation,

$$\begin{gathered}(u_{i0}-\xi)d_\xi\rho_{i1} + \rho_{i1}(1 + d_\xi u_{i0})\\ + u_{i1}d_\xi\rho_{i1} + \rho_{i0}du_{i1} = 0,\\ (u_{i0}-\xi)(\rho_{i0}d_\xi u_{i1} + \rho_{i1}d_\xi u_{i0})\\ + m_{i0}(\partial_{\rho_{10}}p d_\xi\rho_{11} + \partial_{\rho_{20}}p d_\xi\rho_{21})\\ + \rho_{i0}u_{i1}(1 + d_\xi u_{i0}) = (-1)^{i+1}f.\end{gathered} \quad (4)$$

Here, the operator d_ξ implies differentiation with respect to the self-similar variable. Set (4) requires that certain transformations be made; as a result, it takes the normal Cauchy form:

$$\frac{d\rho_{11}}{d\xi} = \frac{(U_{20}^2-\alpha\beta)(A_1U_{10}-B_1) + \alpha(A_2U_{20}-B_2)}{U_{10}^2(U_{20}^2-\alpha\beta) - U_{20}^2},$$

$$\frac{du_{11}}{d\xi} = \frac{U_{10}[B_1(U_{20}^2-\alpha\beta) + \alpha(B_2-A_2U_{20})] - A_1U_{20}^2}{U_{10}^2(U_{20}^2-\alpha\beta) - U_{20}^2},$$

$$\frac{d\rho_{21}}{d\xi} = \frac{(U_{10}^2-1)(A_2U_{20}-B_2) + \beta(A_1U_{10}-B_1)}{U_{10}^2(U_{20}^2-\alpha\beta) - U_{20}^2}, \quad (5)$$

$$\frac{du_{21}}{d\xi} = \frac{U_{20}[B_2(U_{10}^2-1) + \beta(B_1-A_1U_{10})] - A_2\alpha\beta U_{10}^2}{U_{10}^2(U_{20}^2-\alpha\beta) - U_{20}^2}.$$

Here,

$$U_{i0} = u_{i0}-\xi, \quad i = 1, 2, \quad \gamma = \left(1 + \frac{\rho_{20}}{r}\right),$$

$$\alpha = -\frac{\rho_{10}}{r}\gamma, \quad \beta = \frac{\rho_{20}}{r}\gamma,$$

$$A_1 = -[u_{11}\partial_\xi\rho_{10} + \rho_{11}(1 + \partial_\xi u_{10})],$$

$$A_2 = -[u_{21}\partial_\xi\rho_{20} + \rho_{21}(1 + \partial_\xi u_{20})],$$

$$B_1 = \left[\frac{\rho_{10}\rho_{21}}{r^2} + \frac{\rho_{11}}{r}\gamma\right]\partial_\xi\rho_{20} - [\rho_{10}u_{11} + (\rho_{10}u_{11} + \rho_{11}U_{10})\partial_\xi u_{10}],$$

$$B_2 = \left[\frac{\rho_{20}\rho_{21}}{r^2} + \frac{\rho_{21}}{r}\gamma\right]\left(\frac{\rho_{10}\partial_\xi\rho_{20}}{r}\gamma - \partial_\xi\rho_{10}\right) - \left(\frac{\rho_{10}\rho_{21}}{r^2} + \frac{\rho_{11}}{r}\gamma\right)\frac{\rho_{20}\partial_\xi\rho_{20}}{r}\gamma - u_{21}\rho_{20} - (\rho_{21}U_{20} + \rho_{20}u_{21})\partial_\xi u_{20} - \frac{\rho_{20}(u_{20}-u_{10})}{\tau}.$$

2.2. Solution to the set of equations for the zero-order and first approximations. In order for homogeneous set (3) of the zero-order approximation to have a nontrivial solution, its determinant must be equal to zero:

$$\rho_{10}\rho_{20}[(u_{10}-\xi)^2(u_{20}-\xi)^2 - m_{20}p_{\rho_{20}}(u_{10}-\xi)^2 - m_{10}p_{\rho_{10}}(u_{20}-\xi)^2] = 0.$$

Using the notation $m_{10}p_{\rho_{10}} = a_0^2$ and $m_{20}p_{\rho_{20}} = a_0^2\theta$, where $\theta = \dfrac{m_{20}^2\rho_{10}}{m_{10}^2\rho_{20}} = \rho_{10}\varphi(\rho_{20})$, we take the quantities a_0, ρ_{110}, and $\rho_{110}a_0^2$ as normalized units for the velocity, density, and pressure, respectively, and rewrite resolvability condition (3) in the form

$$\rho_{10}\rho_{20}[(u_{10}-\xi)^2(u_{20}-\xi)^2 - \theta(u_{10}-\xi)^2 - (u_{20}-\xi)^2] = 0. \quad (6)$$

From (6), we can express one of the desired functions, for example, ρ_{10}, through the remaining functions; thus, $\rho_{10} = \dfrac{U_{20}^2(U_{10}^2-1)}{U_{10}^2\varphi(\rho_{20})}$. Using the three first equations of zero-order approximation (3), we obtain the set of ordinary differential equations for the three desired functions:

$$\begin{gathered}\frac{du_{10}}{d\xi} = 2U_{10}\frac{m_2}{m_1}F(U_{10}, \rho_{20}, U_{20}),\\ \frac{d\rho_{20}}{d\xi} = -2\rho_2(U_{10}^2-1)F(U_{10}, \rho_{20}, U_{20}),\\ \frac{du_{20}}{d\xi} = 2U_{20}(U_{10}^2-1)F(U_{10}, \rho_{20}, U_{20}).\end{gathered} \quad (7)$$

Here,

$$F(U_{10}, \rho_{20}, U_{20}) = \frac{U_{10}(U_{20}^2 - \theta) + U_{20}(U_{10}^2 - 1)}{U_{20}^2\left(\frac{m_2}{m_1}(U_{10}^2 + 1) + \left(1 + \frac{2}{m_1}\right)(U_{10}^2 - 1)^2\right)}.$$

For the given set of equations, the following nonlinear boundary condition is well-posed at $\xi = \xi^*$:

$$\begin{aligned} &\rho_{10}\rho_{20}[(u_{10} - \xi)^2(u_{20} - \xi)^2 \\ &- \theta(u_{10} - \xi)^2 - (u_{20} - \xi)^2] = 0, \\ &u_{10} = u_{20} = 0, \quad \rho_i = \rho_{i0}, \end{aligned} \tag{8}$$

where ξ^* is the desired quantity.

The quantity ξ^* is determined from boundary condition (8):

$$\xi^* = \sqrt{1 + \theta} = \sqrt{1 + \frac{\rho_{10}\rho_{20}}{(r - \rho_{20})^2}}.$$

From here, it is seen that, in the zero-order approximation, the leading edge of the rarefaction wave propagates with a velocity slightly differing from the frozen velocity of sound. This fact also enables us to numerically solve the newly arisen Cauchy well-posed problem by the Runge–Kutta method with the fifth order of accuracy. It is of interest to determine the type of a set of partial differential equations for this solution. Indeed, this is either a hyperbolic set $\left[\text{for } \frac{(1 + \sqrt[3]{\theta})^3}{(u_1 - u_2)^2} \le 1\right]$ or a mixed set $\left[\text{for } \frac{(1 + \sqrt[3]{\theta})^3}{(u_1 - u_2)^2} > 1\right]$. The calculations showed that the set was of the hyperbolic type only in the case of its approaching the point $\xi = 0$, after the gas has nearly attained the velocity of sound.

3. SOLUTIONS TO EQUATIONS OF HETEROGENEOUS-MEDIUM MECHANICS FOR LARGE TIMES

In accordance with [2], we take that the following conditions are fulfilled as $t \longrightarrow \infty$:

(*1*) All the desired functions have finite limits.

(*2*) The limits of $t\partial_t\Phi$ are finite values; this implies that the derivatives of the desired functions with respect to time tend to zero for constant ξ.

(*3*) The limits of $\partial_\xi\Phi$ are finite values.

Combining the two last equations in (*2*), we obtain the conservation equation for momentum of the mixture as a whole. Dividing the first equation of (*2*) by t, we rewrite it in the form

$$\rho_1\left(\partial_t u_1 + \frac{(u_1 - \xi)\partial_\xi u_1}{t}\right) + m_1\frac{\partial_\xi p}{t} = \frac{\rho_2}{\tau}(u_1 - u_2).$$

From here and by virtue of assumptions (*1*)–(*3*), we obtain that $u_1 = u_2$ as $t \longrightarrow \infty$ and the conservation equation for momentum of the mixture takes the known form

$$\rho(t\partial_t u + (u - \xi)\partial_\xi u) + \partial_\xi p = 0. \tag{9}$$

Combining two continuity equations for the phases, we find the conservation equation for the mass of the mixture:

$$t\partial_t\rho - \xi\partial_\xi\rho + \partial_\xi p = 0. \tag{10}$$

After expressing the mean densities of the phases through their relative mass concentrations and the mixture density $\rho_i = \xi_i\rho$, the equation of state can be written as $p = \frac{a_0^2\xi_1}{v - \frac{\xi_2}{r}}$, where $v = \frac{1}{\rho}$. Thus, as $t \longrightarrow \infty$, the velocity-nonequilibrium flow of the mixture can be described on the basis of the model for the velocity-equilibrium flow expressed by Eqs. (9) and (10).

4. DISCUSSION OF NUMERICAL RESULTS IN TERMS OF THE ZERO-ORDER AND FIRST-ORDER APPROXIMATIONS

In the process of numerical calculations, we investigated the effect of the initial particle concentration on the flow pattern. For this purpose, we found the flow parameters in the zero-order and the first-order approximations while varying the initial volume concentration of the particles. The results of the calculations, namely, the values of the desired functions at the channel cut, i.e., at the point $\xi = 0$ (or close to it), are given in the table. The velocity of motion of the left-hand boundary for the one-dimensional channel was equal to $D = 0.01$ in all variants, while the velocity of both the particles and the gas vanished at the point ξ^*.

The second and third lines of the table contain the initial values of the flow parameters, while the zero-approximation parameters and the complete values of the corresponding functions are presented in the subsequent lines. As we expected, the sonic flow is realized at the channel cut with a high degree of accuracy. This result follows from the generalized-action law: the friction in a subsonic gas flow accelerates the gas. In addition, it can be seen that the lower the particle concentration, the closer the flow velocity at the channel cut to the sonic velocity.

In Fig. 1, as an illustration of the weak effect of the particle concentration on the nearly linear profile of the

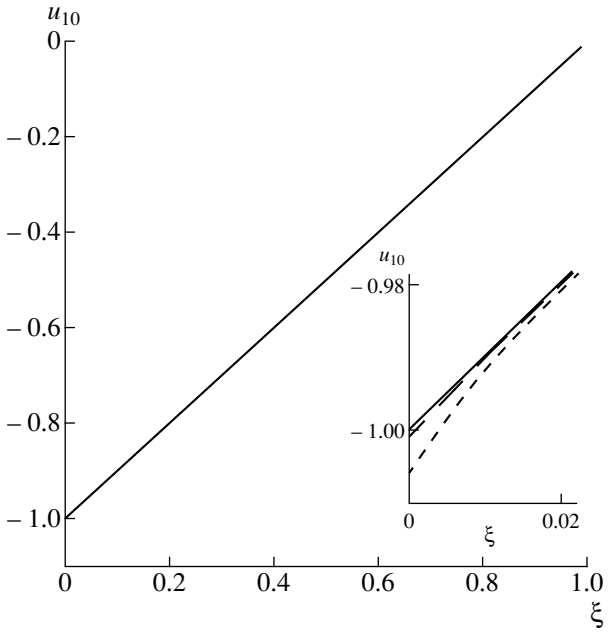

Fig. 1. Gas velocity in the zero-order approximation as a function of the self-similar variable ξ for various initial volume concentrations of particles. In the inset, solid, broken, and dashed curves correspond to $m_{20} = 10^{-4}$, 10^{-3}, and 10^{-2}, respectively.

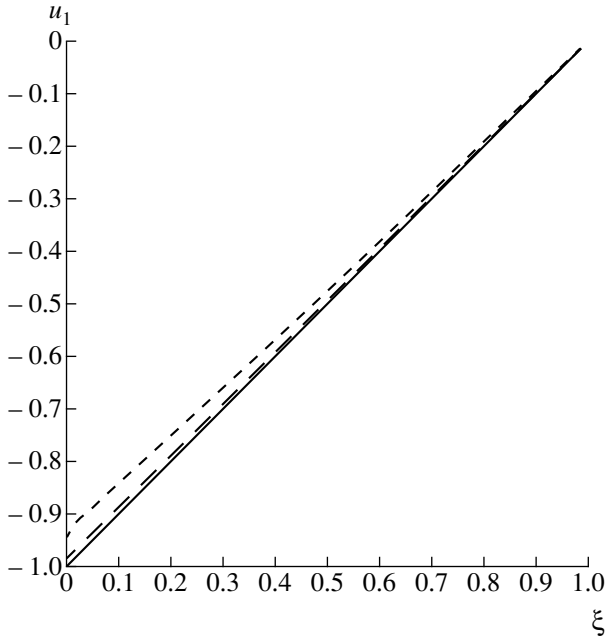

Fig. 2. Total gas velocity as a function of the self-similar variable ξ for various initial volume concentrations of particles. Solid, broken, and dashed curves correspond to $m_{20} = 10^{-4}$, 10^{-3}, and 10^{-2}, respectively.

gas velocity in the zero-order approximation, we show this velocity as a function of the self-similar variable for $m_{20} = 10^{-4}$, 10^{-3}, and 10^{-2}. For these values of m_{20}, the gas-velocity curves, in the first-order approximation, are already markedly different in amplitude. Lastly, in Fig. 2, we show the gas velocity $u_1(\xi, t^*) = u_{10}(\xi) + t^* u_{11}(\xi)$, where t^* is fitted in such a manner that $\rho_i(\xi, t)$ is positive and finite, while $t\rho_{i1}(\xi, t) \ll \rho_{i0}(\xi, t)$. As can be seen, with an increase in m_{20}, the gas velocity in the vicinity of the channel cut is slightly different from the sound velocity and the linearity condition for the velocity profile is violated. However, with further decreasing ξ, it is possible to attain the velocity of sound. Physically, this corresponds to the fact that the sonic velocity is attained in a channel of sightly larger length. The calculations show that, in the case of varying m_{20}, the particle velocity in the zero-order and first approximations, as well as the total velocity of particles, vary nonlinearly. The particles are accelerated from the zero velocity to that equal approximately to

Values of the flow parameters at the channel cut for various volume concentrations of particles

Parameter	$m_{20} = 0.01$	$m_{20} = 0.001$	$m_{20} = 0.0001$
ξ^*	1.000001889	1.000000186	1.000000019
$\rho_2(\xi^*)$	27	2.7	0.27
u_{10}	–1.005869910	–1.000583987	–1.000059497
u_{20}	–0.01085444072	–0.01080436506	–0.01081764804
ρ_{10}	0.3693449512	0.3722505916	0.3811389960
ρ_{20}	26.55015378	2.663420219	0.2663495078
u_1	–0.9507967278	–0.9937236306	–0.9993609239
u_2	–0.01423633305	–0.01407942092	–0.01408944370
ρ_1	0.3748279416	0.3733083333	0.3812540796
ρ_2	26.13981477	2.635482528	0.2635928975

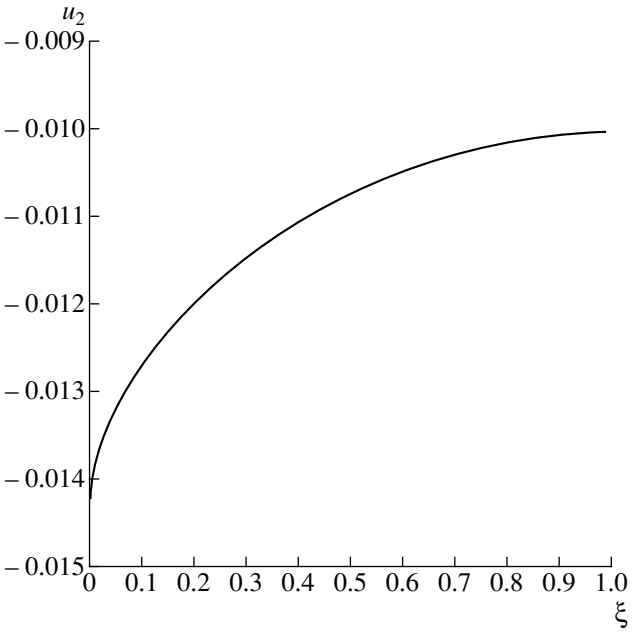

Fig. 3. Total velocity of particles as a function of the self-similar variable ξ for various initial volume concentrations of particles ($m_{20} = 10^{-4}$, 10^{-3}, and 10^{-2}).

5 m/s at a given velocity of the channel-cut propagation. In Fig. 3, we show the total velocity of particles for three values of their volume concentration. As is clearly seen, the curves are not distinguished in the plot scale used.

Thus, in this paper, we proved analytically that, for small times of rarefaction processes in a gas suspension, the leading edge of the rarefaction wave propagates with a velocity close to the frozen sound velocity in this gas. As the process develops, i.e., for large times, the edge moves with the equilibrium sound velocity. The calculations were carried out by E.V. Ogurtsov.

REFERENCES

1. Yu. V. Kazakov, A. V. Fedorov, and V. M. Fomin, Prikl. Mekh. Tekh. Fiz. **28** (5), 139 (1987).
2. W. W. Wood and F. R. Parker, Phys. Fluids **1**, 230 (1958).

Translated by V. Bukhanov

Doklady Physics, Vol. 46, No. 3, 2001, pp. 195–198. Translated from Doklady Akademii Nauk, Vol. 377, No. 2, 2001, pp. 194–197.

MECHANICS

The Instability of the Working Process in the Combustion Chamber of a Solid-Propellant Rocket Engine

Yu. M. Davydov* and M. Yu. Egorov**

Presented by Academician G.G. Chernyĭ August 1, 2000

Received August 10, 2000

Investigation of working-process dynamics is one of the most important problems in developing modern and promising solid-propellant rocket engines. This urgent trend is considered in the fundamental monographs [1–3] of A.M. Lipanov and other authors. The problem of working-process instability arose in its various manifestations simultaneously with the onset of the development and use of the first solid-propellant rocket engines (SPREs) [4, 5], liquid-propellant rocket engines [5, 6], and rocket engines using other forms of propellants [7]. At present, in connection with the development of a new generation of rocket engines with high power–mass characteristics, the urgency of the problem gained momentum. In the general case, the working-process instability in SPREs can be of acoustic and nonacoustic deeply nonlinear nature [1, 5, 7]. The acoustic instability (this kind of instability is considered in our paper) is associated with the appearance of periodic low-frequency and high-frequency pressure oscillations in the engine combustion chamber. Low-frequency pressure oscillations with an approximate frequency range f from ≈50 to 2500 Hz manifest themselves mainly in the longitudinal direction of the combustion chamber. The high-frequency pressure oscillations in the frequency region $f > 2500$ Hz manifest themselves in the transverse and tangential directions of the combustion chamber.

Analysis of experimental and theoretical investigations [8, 9] leads us to the conclusion that the low-frequency acoustic working-process instability in the SPRE is of a hydrodynamic nature; however, there is no conclusive confirmation of this fact in [8, 9] or other papers. High-frequency instability is most often a consequence of interaction of resonance waves generated in the rocket-engine combustion chamber with the combustion surface of the solid-propellant charge [5, 7].

The most dangerous instability is the low-frequency acoustic working-process instability in a SPRE. This type of instability is characterized by a significant deviation of the working pressure in the combustion chamber from its mean value. Such an instability violates the expected regime of the nozzle operation and initiates a periodic vibrational-load transfer from the engine to the rocket system as a whole, etc.

To date, the appearance of low-frequency acoustic instability in SPREs has been poorly predicted and is unaffected by direct numerical calculation, which fails to reproduce the actual oscillation process. There are only indirect rather approximate methods available for estimating the possibility of initiating pressure oscillations in engines of a certain typical construction [9]. Rocket engineers are forced to eliminate this type of instability by experimental optimization of the engine design using the trial-and-error procedure.

In the paper proposed, we pioneer the reproduction of an actual oscillation process in a direct numerical experiment and investigate the mechanism of initiation and feed of the low-frequency acoustic instability in a SPRE combustion chamber.

We carried out the direct numerical simulation of the low-frequency acoustic instability in SPREs by the coarse-particle method (see, e.g., [10]), which successfully manifested itself while solving many nonlinear problems of continuum mechanics (see, e.g., [11]). In these calculations, both explicit and implicit parametric totally conservative finite-difference schemes inherent in this method were used. For describing the flow process in a SPRE combustion chamber and a nozzle, we employed approaches of multiphase-medium mechanics [12]. As the basic physicomathematical model, the total unsteady set of gas-dynamic eddy differential equations written in the divergent form for a heterogeneous medium (gas + solid particles) was used. From the spatial point of view, the problem was studied in an axially symmetric formulation. A uniform orthogonal computational mesh was used. At irregular boundaries (not coinciding with the computational mesh) of the calculation region, the fractional-mesh technique [13]

** Institute of Mechanics and Ecology, Moscow, Russia*
*** Perm State Technical University, Komsomol'skiĭ pr. 29a, Perm, 614600 Russia*

1028-3358/01/4603-0195$21.00

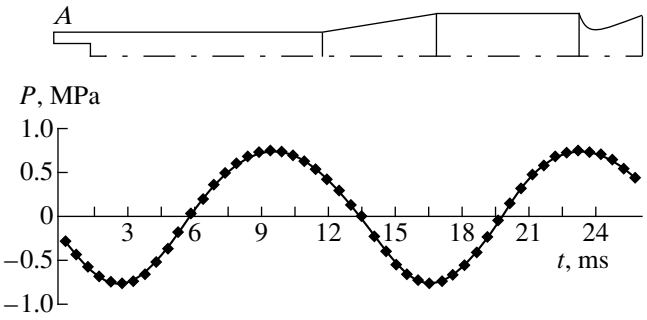

Fig. 1. Schematic diagram of a SPRE combustion chamber according to Variant no. 1 and time variation of pressure in the combustion chamber.

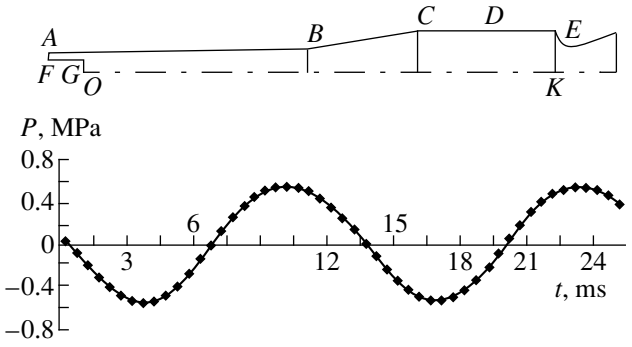

Fig. 2. Schematic diagram of a SPRE combustion chamber according to Variant no. 2 and time variation of pressure in the combustion chamber.

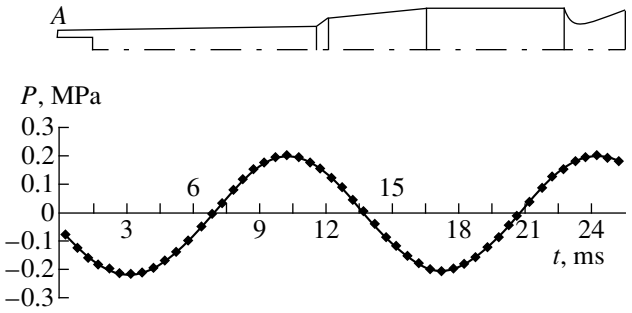

Fig. 3. Schematic diagram of a SPRE combustion chamber according to Variant no. 3 and time variation of pressure in the combustion chamber.

was applied. The yield from the surface of combustion of the solid-propellant charge was calculated by "injecting" the combustion products with given fixed parameters into the computational meshes arranged in a certain geometric order on the combustion surface.

We now consider certain results of these calculations.

Figure 1 shows a schematic diagram for the free volume of the SPRE combustion chamber according to Variant no. 1 and the pressure in the combustion chamber (deviation from the mean value at a given point) as a function of time for several periods of oscillations. The pressure is fixed in the region of the engine forepart bottom (position *A*). The pressure-oscillation amplitude and frequency amount to $A_P = 0.75$ MPa and $f = 77$ Hz, respectively, the oscillation process being stable. In the process of attaining the steady-flow regime in the engine combustion chamber, the pressure-oscillation amplitude is invariable.

Figure 2 shows the schematic diagram for the free volume of the SPRE combustion chamber according to Variant no. 2 and the pressure in the combustion chamber as a function of time. The parameters measured are similar to those presented in Fig. 1. The pressure-oscillation amplitude and frequency amount to $A_P = 0.55$ MPa and $f = 77$ Hz, respectively. The oscillation process remains stable. The pressure-oscillation amplitude in the process of attaining the steady-flow regime in the engine combustion chamber is also invariable.

Figure 3 shows the schematic diagram for the free volume of the SPRE combustion chamber according to Variant no. 3 and the time dependence of pressure in the combustion chamber. The measured parameters are also similar to those in Fig. 1. The pressure-oscillation amplitude and frequency amount to $A_P = 0.21$ MPa and $f = 76$ Hz, respectively. The oscillation process remains stable. The pressure-oscillation amplitude in the process of attaining the steady-flow regime in the engine combustion chamber is, again, invariable.

On the basis of the data presented, we can conclude that the geometric shape of the combustion-chamber essentially affects the pressure-oscillation amplitude in the SPRE combustion chamber. In the case of purposeful modification of the combustion-chamber configuration, the pressure-oscillation amplitude decreases by a factor of 0.75 MPa/0.21 MPa = 3.57. In this case, the pressure-oscillation frequency in the engine combustion chamber varies negligibly.

We consider, in more detail, the dynamics of the distribution of flow gas-dynamic parameters over the free volume of the SPRE combustion chamber before the flow enters the nozzle. The schematic diagram for the free volume of the engine combustion chamber is given in Fig. 2. We compare the flow parameters for combustion products at various moments of time (within a single pressure-oscillation period) along the combustion-chamber length in the following cross sections of the conic-cylindrical chamber (Fig. 2): (*1*) near the symmetry axis *OK* and near the igniter surface *FGO* (below, for brevity, this cross section is termed the symmetry axis) and (*2*) near the combustion surface of the solid-propellant charge *ABCD* and the combustion-chamber wall *DE* (below, for brevity, this cross section is termed a wall).

In Fig. 4, the distribution for the velocity longitudinal component u_1 for gaseous combustion products along the SPRE combustion-chamber length in the two

fixed cross sections (of the conic-cylindrical chamber) defined above is shown for various moments of time. The distribution of the transverse velocity component v_1 for gaseous combustion products is virtually uniform and essentially invariable in time. The only exception is the local zone in the nozzle region of the rocket engine, which is outside the scope of our consideration.

At the time moment t = 2.5 ms (Fig. 4), an increase in the velocity of motion of the combustion products along the symmetry axis from the forepart bottom (position *AF* in Fig. 2) to the onset of the region of large inverse conicity (position *B)* up to $u_{1max} \approx 182$ m/s takes place. Upon deeper entering into the region of large inverse conicity, the flow is slightly damped. Furthermore, passing by the cylindrical section and entering into the nozzle, the flow is intensely accelerated. At a given time moment, a considerable variation in the velocity longitudinal component of gaseous combustion products along the combustion chamber radius is observed, this variation being the most prominent near the combustion surface of the solid-propellant charge (*ABCD* surface, Fig. 2) and near the lateral wall of the combustion chamber (*DE* surface, Fig. 2). Against the background of the general direction of motion of the combustion-product flow from the forepart bottom to the nozzle, a pronounced counterflow is observed near the combustion surface of the solid-propellant charge. Here, the combustion products move from the nozzle to the forepart bottom. The longitudinal component of the counterflow velocity attains $u_{1max} \approx -13$ m/s. In the region of the rear bottom, an enormous zone of damping of the combustion-product flow is formed near the wall of the combustion chamber (position *E* in Fig. 2).

At the time moment t = 7.5 m/s (Fig. 4), an increase in the velocity of combustion products up to $u_{1max} \approx$ 199 m/s occurs along the symmetry axis from the forepart bottom to the onset of the region of large inverse conicity. Upon entering into this region and further into the rear-bottom region, the flow is slightly damped. Entering into the nozzle, the combustion-product flow is intensely accelerated. At a given time moment, we also observe variation in the longitudinal velocity component of the combustion products along the combustion-chamber radius. However, in this case, there is no counterflow zone along the combustion surface of the solid-propellant charge. The velocity longitudinal component of the combustion-product flow along the combustion surface gradually increases and attains a velocity $u_{1max} \approx 72$ m/s. Furthermore, upon entering into the region of the large inverse conicity, the near-wall flow velocity drops to a value $u_{1min} \approx 5$ m/s. In the rear-bottom region near the combustion-chamber wall, an enormous damping zone for combustion-product flow is retained.

At the time moment t = 12.5 m/s (Fig. 4), against the background of the general direction of motion of combustion-product flow from the forepart bottom to the nozzle, local zones of the counterflow again begin to

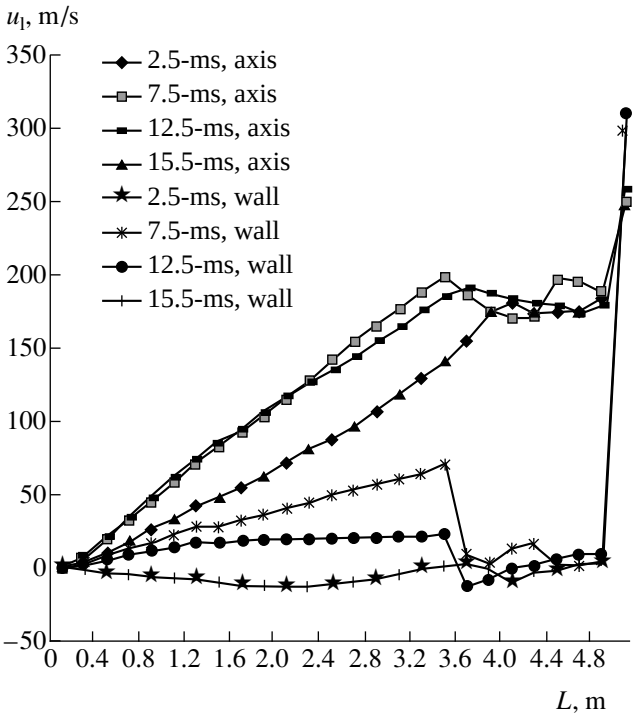

Fig. 4. Distribution of the velocity longitudinal component for combustion products along the length of the SPRE combustion chamber at various time moments.

arise near the combustion surface of the solid-propellant charge in the forepart-bottom region and in the region of large inverse conicity. The velocity longitudinal component of the combustion-product flow along the charge combustion surface decreases, attaining extreme values $u_{1max} \approx 24$ m/s and $u_{1min} \approx -12$ m/s. Gradually, the conditions for the formation of an extensive counterflow region along the combustion surface of the solid-propellant charge are prepared.

Furthermore, for the oscillation period $\tau \approx 13$ m/s, from the time moment t = 15.5 ms (Fig. 4), the flow pattern in the SPRE combustion chamber begins to be cyclically repeated (the lines denoted as 2.5-ms, axis and 15.5-ms, axis and 2.5-ms, wall and 15.5-ms, wall virtually coincide).

Thus, the causes for the initiation (excitation and feed) of the oscillation process in the SPRE combustion chamber should be sought in the structure and nature of the combustion-product flow in itself. Here, the oscillations are of a hydrodynamic (gas-dynamic) deeply nonlinear nature. The frequency and the amplitude of oscillations (especially, the amplitude) depend on a number of factors. The main factor is the significant combustion-product flow stratification over the flow parameters (mainly, over the velocity) along the combustion-chamber radius. The flow of such a complicated structure upon entering into the nozzle irregularly interacts with the engine rear-bottom wall and is, in part, reflected from it. In the rear-bottom region near the lat-

eral wall of the combustion chamber, a flow (counterflow) either is formed opposite to the basic flow or is considerably damped. Thus, an unsteady low-frequency acoustic pulsatory flow is excited (due to the finite size of the combustion chamber) and cyclically fed into the SPRE combustion chamber.

REFERENCES

1. B. T. Erokhin and A. M. Lipanov, *Nonsteady and Quasisteady Operation Conditions of Solid-Propellant Rocket Engines* (Mashinostroenie, Moscow, 1977).
2. A. M. Lipanov and A. V. Aliev, *Designing of Solid-Propellant Rocket Engines* (Mashinostroenie, Moscow, 1995).
3. A. M. Lipanov, V. P. Bobryshev, A. V. Aliev, *et al.*, in *Numerical Experiment in Theory of Solid-Propellant Rocket Engines*, Ed. by A. M. Lipanov (Nauka, Yekaterinburg, 1994).
4. *Studies of Solid-Propellant Rocket Engines*, Ed. by M. Summerfield (Academic, New York, 1960; Inostrannaya Literatura, Moscow, 1963).
5. T. M. Mel'kumov, N. I. Melik-Pashaev, P. G. Chistyakov, and A. G. Shiutov, *Rocket Engines* (Mashinostroenie, Moscow, 1976).
6. K. S. Kolesnikov, *Longitudinal Oscillations of Rockets with Liquid-Fuel Engines* (Mashinostroenie, Moscow, 1971).
7. V. E. Alemasov, A. F. Dregalin, and A. P. Tishin, *Theory of Rocket Engines* (Mashinostroenie, Moscow, 1980).
8. D. I. Blokhintsev, *Acoustics of an Inhomogeneous Moving Medium* (Nauka, Moscow, 1981).
9. S. V. Sukhinin and V. F. Akhmadeev, Fiz. Goreniya Vzryva **29** (6), 38 (1993).
10. Yu. M. Davydov, in *Mathematical Encyclopaedia* (Sov. Éntsiklopediya, Moscow, 1982), Vol. 3, pp. 125–129.
11. Yu. M. Davydov, M. Yu. Egorov, A. M. Lipanov, *et al.*, in *Computational Investigation of Urgent Problems in Machine Building and Mechanics of Continuous and Free-Flowing Media by Coarse-Grain Method*, Ed. by Yu. M. Davydov (Moscow, 1995), Vols. 1–5.
12. R. I. Nigmatulin, *Foundations of Mechanics of Heterogeneous Media* (Nauka, Moscow, 1978).
13. Yu. M. Davydov, Zh. Vychisl. Mat. Mat. Fiz. **11**, 1056 (1971).

Translated by V. Bukhanov

Doklady Physics, Vol. 46, No. 3, 2001, pp. 199–201. Translated from Doklady Akademii Nauk, Vol. 377, No. 2, 2001, pp. 198–200.

MECHANICS

Effect of Supercirculation in a Flow around a Thick Airfoil with Vortex Cells

S. A. Isaev, A. G. Sudakov, P. A. Baranov, and Yu. S. Prigorodov

Presented by Academician G.G. Chernyĭ August 28, 2000

Received August 30, 2000

Development of flow-control systems using vortex cells with internal flow intensification by pulses generated in a certain way represents one of the urgent fields of modern aerohydrodynamics. An example for design realization of this idea is the promising project of the "ÉKIP" aircraft with a thick-wing shape and an engine which brings into operation a system of suction out of vortex cells situated along its contour [1].

Recent numerical investigations [2–5] validate the method for controlling a flow around different objects, which is based on flow intensification in vortex cells situated along the object contour. This method is realized by causing either rotation of central bodies or suction through their surfaces. As examples, laminar and turbulent flows around both a circular cylinder with vortex cells and an airfoil whose shape is similar to the simplified form of the integral-layout aircraft "ÉKIP" capable of changing in wide limits its angle of attack are considered. The results obtained show that, in principle, by affecting flows within small-size vortex cells, we can change the large-scale vortex structure of the airfoil wake. In this case, we can remove flow separation, decrease the drag, and considerably increase the lift-to-drag ratio at acceptable energy expenditures and with a relatively simple realization of the method in practice.

To solve these problems, we have developed an original computational algorithm. This algorithm makes it possible to simulate detached flows in multiply connected regions and is based on both using multiblock intersecting computational meshes and solving Reynolds equations closed by a Menter zonal SST-model of turbulence [6]. With the help of an implicit factorized finite-volume procedure, the computational complex was verified, in particular, by solving the problem of a flow in a channel with a circular vortex cell [7].

In this paper, we investigate a thick airfoil. Its upper part represents a circular arc, while both segments of small-radius circular arcs and a plane form its bottom. As a linear (one-dimensional) scale, we take the size of the airfoil chord. A series of four elliptic vortex cells with central bodies of the same shape is embedded into the airfoil under consideration. Figure 1 shows a pattern of the airfoil with the vortex cells. The velocity component V_n satisfying the suction condition is given on the surfaces of the central bodies. The model of the vortex-flow intensification in the cells under consideration reflects, to a certain extent, the intake of air which was injected by the engine through a porous insertion. Such action on the flow inside the cells brings a momentum into the outside flow through the cuts made in a thick airfoil; this significantly changes the flow around it. When the model of viscous fluid is used, the airfoil angle of attack is set equal to zero.

The algebraic nonorthogonal O-type mesh is constructed around the airfoil. Its first tier adjacent to the airfoil contains 41×520 nodes situated in the dimensionless band with a thickness of 0.1 and crowded toward the wall. The near-wall step is set equal to

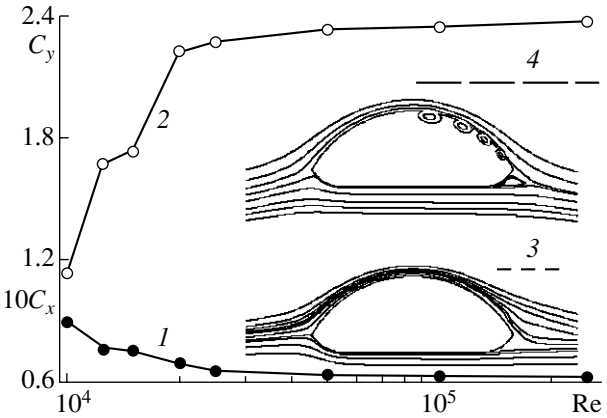

Fig. 1. Dependence of the (*1*) drag coefficient and (*2*) lift coefficients on the Reynolds number. Calculated values of C_y for the airfoils with (*3*) equivalent suction ($\mathrm{Re} = 10^5$) and (*4*) imposed circulation, which is generated by the cells and is determined by the method of discrete vortices. Comparison of flow fields arising around airfoils with vortex cells and with the equivalent suction at $\mathrm{Re} = 10^5$.

Academy of Civil Aviation, St. Petersburg, Russia

1028-3358/01/4603-0199$21.00

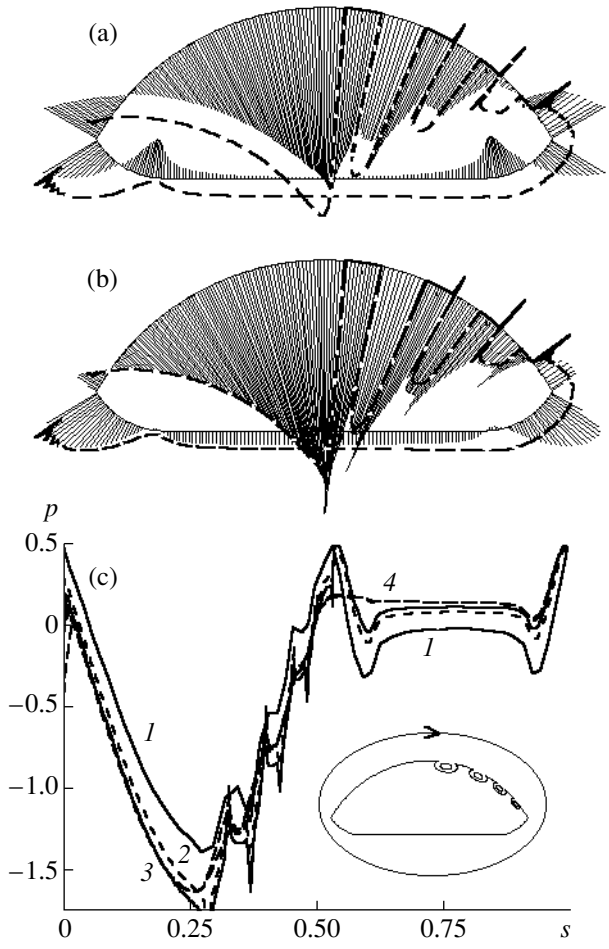

Fig. 2. Comparison of pressure distributions along the airfoil, which are calculated by the method of discrete vortices (solid line) within the framework of the viscous model (dashed line) for (a) $\Gamma = 0$; (b) $\Gamma = 0.5$; (c) (*1*) $\Gamma = 0$, (*2*) 0.375, and (*3*) 0.5. Curve (*4*) describes the function $p(s)$ calculated according to the viscous model for $\mathrm{Re} = 10^5$.

0.0005. The second tier consisting of 80×250 cells covers the space around the airfoil at a distance of 40 chords. The vortex cells are partitioned by an O-type mesh in which, in radial direction, 51 to 41 nodes are disposed crowding toward the central bodies. The mesh is uniform in the circumferential direction and contains 23 to 17 nodes (whose number decreases with diminishing cell size) in the region of the airfoil cut.

According to Fig. 1, for the airfoil with vortex cells, inside which the flow is intensified by suction (V_n is set equal to 0.05 in each cell), the effect of viscosity on the flow around it manifests itself in an abrupt increase in lift coefficient C_y for Reynolds numbers ranging from 10^4 to 2×10^4. In this case, C_x does not vary strongly within the range of Re compared to C_y. The preliminary calculations [5] showed that such a behavior of the lift and drag coefficients is associated with a decrease in flow separation from the airfoil with increasing Re. According to the results presented here, the process under discussion is caused by a growth of flow turbulization in the vortex cells with increasing the flow velocity therein. It is noteworthy that the function $C_y(\mathrm{Re})$ exhibits asymptotic features as $\mathrm{Re} \longrightarrow \infty$.

In this paper, we compare and analyze integral aerodynamic forces and pressure distributions along the airfoil, which are calculated by the method of discrete vortices [7] and the finite-volume procedure of solving Reynolds equations. Within the framework of the method of discrete vortices, the steady-state separation-free flow around the airfoil is calculated with substitution of the cells by suction, where suction rates are such that flow rates through both airfoil elements and surfaces of the interior bodies are equal to each other. It is postulated that the flow smoothly leaves the airfoil at its trailing edge.

At $\mathrm{Re} = 10^5$, we discovered a substantial difference in the values of the lift force acting on the airfoil: $C_y = 1.27$ in the method of discrete vortices and $C_y = 1.8$ in the viscous model (in the latter case, the coefficient of total lift is equal to 2.34). The models also yield essentially different incoming-stream angles (Fig. 2a).

If the turbulent flow around the airfoil is formed at the zero angle of attack, the results of calculation by the method of discrete vortices are close to those obtained according to the viscous model ($C_y = 1.11$). These results are obtained by replacement of the vortex cells by suction through airfoil elements. As is seen in Fig. 1, the flow fields arising here and in the case of the airfoil with vortex cells are extremely different. For the airfoil with vortex cells, the front stagnation point is situated at the bottom generatrix of the airfoil contour, while, in the absence of the cells, the attachment of the incident flow occurs in the vicinity of the airfoil front edge. Thus, the vortex cells not only promote separation-free flow from the airfoil, but also make the flow incident at a certain effective angle of attack. Apparently, the cause of this effect lies in the generation of additional circulation inside the vortex cells. The total vortex power in the cells is estimated as $\Gamma = 0.38$.

To take into account the additional circulation generated inside the cells, the solution obtained by the method of discrete vortices is modified by adding the given value of the obtained circulation to it. In this case, the flow leaves the airfoil at a point not coinciding with its trailing edge. Figure 2b shows that, at the total vortex strength $\Gamma = 0.5$, the model under consideration and the viscous model predict pressure distributions along the airfoil which are very close to each other. As a whole, the lift coefficients $C_y = 2.28$ and 2.03 calculated for $\Gamma = 0.5$ and 0.375, respectively, agree satisfactorily with the prediction of the viscous model ($C_y = 2.34$).

ACKNOWLEDGMENTS

The work was supported by the Russian Foundation for Basic Research, projects nos. 99-01-01115 and 99-01-00722.

REFERENCES

1. A. I. Savitsky *et al.*, US Patent No. 5417391 (1995).
2. P. A. Baranov, S. A. Isaev, Yu. S. Prigorodov, and A. G. Sudakov, Pis'ma Zh. Tekh. Fiz. **24** (17), 16 (1998) [Tech. Phys. Lett. **24**, 671 (1998)].
3. P. A. Baranov, S. A. Isaev, Yu. S. Prigorodov, and A. G. Sudakov, Izv. Vyssh. Uchebn. Zaved., Aviats. Tekh., No. 3, 30 (1999).
4. P. A. Baranov, S. A. Isaev, Yu. S. Prigorodov, and A. G. Sudakov, Pis'ma Zh. Tekh. Fiz. **24** (8), 33 (1998) [Tech. Phys. Lett. **24**, 301 (1998)].
5. P. A. Baranov, S. A. Isaev, Yu. S. Prigorodov, and A. G. Sudakov, Inzh.-Fiz. Zh. **72**, 572 (1999).
6. F. Menter, AIAA J. **32**, 1598 (1994).
7. S. A. Isaev, S. V. Guvernyuk, M. A. Zubin, and Yu. S. Prigorodov, Inzh.-Fiz. Zh. **73**, 220 (2000).
8. S. M. Belotserkovskiĭ and M. I. Nisht, *Separation and Separation-Free Flows of Ideal Fluids around Thin Wings* (Nauka, Moscow, 1978).

Translated by Yu. Verevochkin

Doklady Physics, Vol. 46, No. 3, 2001, pp. 202–206. Translated from Doklady Akademii Nauk, Vol. 377, No. 2, 2001, pp. 201–205.

MECHANICS

Mirror and Diffuse Sound Scattering by a Two-Dimensional Wake in a Continuously Stratified Fluid

V. V. Mitkin, V. E. Prokhorov, and Yu. D. Chashechkin

Presented by Academician A.Yu. Ishlinskiĭ August 9, 2000

Received August 11, 2000

Remote acoustic methods play a key role in studying the dynamics of the atmosphere and ocean. This fact is explained by the low attenuation of sound in sea water and the strong dependence of the sound refractive index on both the atmosphere temperature and humidity [1]. In stratified media free of admixtures, turbulence is believed to be the primary cause of sound scattering. This fact has been confirmed by numerous atmosphere sounding experiments carried out according to a bistatic configuration (i.e., with a remote static emitter and receiver). This method made it possible to identify microstructural bulk fluctuations by measuring scattering angular distributions [1]. However, there are many cases when acoustic-sounding data strongly differ from the results of contact measurements (e.g., in the case of structural-constant measurements). These discrepancies may be caused by the sound reflection from thin high-gradient layers, which is beyond the scope of the bulk scattering model [2].

The construction of a stable bistatic array in the open ocean is a rather complicated engineering task. Therefore, the greater part of relevant data was obtained by means of the acoustic-radar method, i.e., by measuring the backscattering of sound. The character of this scattering can be well established only for bioaggregations according to catching data or to the characteristic migration of sound-scattering water layers. When these bioaggregations are absent, the sound scattering is associated with either the turbulence (this conclusion is based on the characteristic frequency dependence of signals [3]) or the reflection of sound from thin water layers (in the case of the observed anomalous dependence of signals on small vertical deviations of the sonar ray [4–6]). Laboratory-scale experiments on vertical echo sounding of a wake behind a cylinder moving in a stratified fluid [6, 7] also testify to the latter effect. However, comparative analysis of the efficiency of these scattering mechanisms has not yet been fulfilled.

The wake behind a horizontal cylinder uniformly moving in a continuously stratified fluid is an adequate object for implementation of such an analysis. In a wide range of flow regimes, this wake contains mixed nonuniformities, namely, a bulk structure of turbulent spots and thin high-gradient interlayers. Studying the scattering angular distributions makes it possible to distinguish the contributions of separate structural flow components. In this paper, we present, for the first time, our experimental data on the ultrasound scattering by the wake behind a two-dimensional cylinder. These data were obtained by means of a bistatic array that allowed visualization of the flow pattern to be simultaneously performed.

Our experiment was carried out in a tank $200 \times 40 \times 60$ cm^3 in size which was filled with a water solution stratified with respect to the salt concentration. The tank was equipped with a high-frequency sonar, an IAB–458 shadow device (with a visual-field diameter of 23 cm), and an automatic camera. The optical axis of the shadow device passed through the tank center perpendicularly to the vertical plane.

The sonar had identical transmitting and receiving antennas (piezoelectric-ceramics disks with a diameter a = 2.5 cm). Its carrier frequency, transmitted-pulse duration τ, and pulse-transmission period were, respectively, 1 MHz (a sound wavelength λ = 0.15 cm), 40 μs, and 0.16 s. The axes of the directivity patterns for the transmitting and receiving antennas lay in the vertical plane. The antennas' configuration is represented by the shadowgraph of the sound beams (see Fig. 1), which was obtained in the regime of continuously radiating antennas. The opening angle of both sound beams is $2\alpha = 4°$. The angle between the wave vectors $\mathbf{k}_0$ and $\mathbf{k}_s$ for the incident and scattered sound waves, respectively, is denoted by θ. The position of the bistatic configuration with respect to the horizontal reflecting surface is defined by the angle φ between the difference vector $\mathbf{k} = \mathbf{k}_s - \mathbf{k}_0$ and the vertical axis. In our experiments, the angles θ and φ varied from 39° to 88° and

Institute of Problems in Mechanics,
Russian Academy of Sciences,
pr. Vernadskogo 101, Moscow, 117526 Russia

1028-3358/01/4603-0202$21.00

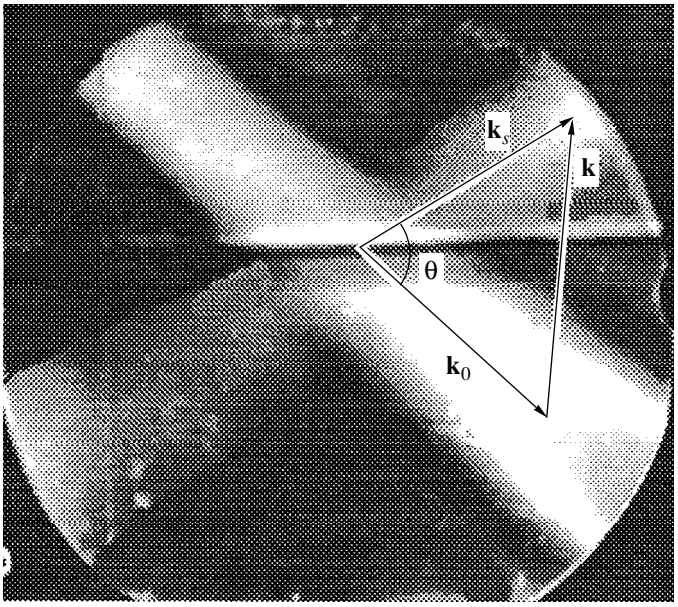

Fig. 1. Shadowgraph of intersecting sound beams and configuration of the bistatic sounding array. The arrows show the wave vectors for incident ($\mathbf{k}_0$) and scattered ($\mathbf{k}_s$) sound waves. The central horizontal strip shows the interface in the wake behind the cylinder for the wake age $t = 50T_b$.

from –11° to 15°, respectively. These ranges were provided by rotating and vertically translating the antennas, with the fixed horizontal distance D = 36 cm between them.

Using a ladle device, we filled the tank (by the method of continuous displacement) with a solution of sodium chloride. In several hours, a linear density distribution $\rho(z)$ over the depth z was set in a tank with an almost constant buoyancy period $T_b = 2\pi\left(g\rho^{-1}\frac{d\rho}{dz}\right)^{-1/2}$ = 6 s (g is the gravitational acceleration). The kinematic viscosity (ν = 0.01 cm^2 s^{-1}) and temperature were assumed to be constant. A horizontal cylinder with diameter d = 1.5 m was towed with a velocity U = 3 cm s^{-1} along the middle plane of the tank. In the chosen regime of motion $\left(\text{the Froude number Fr} = \frac{U}{Nd} = 1.7\right.$ and the Reynolds number Re = $\frac{Ud}{\nu}$ = 430, with $N = \left.\frac{2\pi}{T_b}\right)$, a relation between the inertial forces, buoyancy, and dissipation effects was provided such that a well-developed bulk microstructure with a thin central interface coexisted in the wake behind the cylinder.

The microstructural nonuniformities with the wave number $k = 2k_0\sin\frac{\theta}{2}$ mostly contribute to the bulk scattering. In this case, the scattering cross section m_V for a unit volume per unit solid angle is expressed in terms of the three-dimensional spectrum $\Phi_r(k)$ for fluctuations of the sound refractive index [9]:

$$m_V = 2\pi k_0^4 \Phi_r(k). \quad (1)$$

Assuming the microstructural fluctuations to be locally isotropic, we have

$$\Phi_r(k) = -(2\pi k)^{-1}\frac{dF_r(k)}{dk}, \quad (2)$$

where $F_r(k)$ is the one-dimensional spectrum for fluctuations of the refractive index. This spectrum can be evaluated with an accuracy to a constant factor according to the spectrum $Y(k)$ of microstructural nonuniformities on the shadowgraph of the scattering region. The result desired follows from linear relations between the shadowgraph blackness density, the beam deflection in the shadow device, and the fluctuations of gradients for the density, sound velocity, and light refractive index [8, 11]. Whence it follows, finally, that the spectrum $Y(k)$ is proportional to the one-dimensional spectrum $F_r'(k)$ for the local gradient of the sound refractive index. With regard to expression (2) and the equality $F_r'(k) = kF_r(k)$, cross section (1) is reduced to the form $m_V = A\Phi(k)$, where $\Phi(k) = k^{-3}\left(Y(k) - k\frac{dY(k)}{dk}\right)$ and A is a constant. The normalization of the quantity m_V to

its maximum value Φ_m within the range of k under consideration allows us to exclude the constant A:

$$m_n = \frac{\Phi(k)}{\Phi_m}. \quad (3)$$

In order to find $Y(k)$, we scanned the shadowgraphs along a straight line parallel to the vector **k** and passing through the center of the visual field for the shadow device. We then transformed the obtained numerical arrays into spectra, and, in each of them, only the domain of $k > 2k_0\sin\frac{\theta_0}{2}$ was subsequently analyzed. This domain corresponds to microstructural nonuniformities, with $\theta_0 = 39°$ being the minimum value of the angle θ. The experimental value m_V of the cross section was calculated by the formula $m_V = \frac{P_s}{V\Omega I_i}$. Here, $P_s = \frac{U_s^2}{R}$ is the scattering power at the reception point, R is the equivalent input resistance of the receiver, U_s is the voltage at the receiver input, I_i is the intensity of the incident sound beam, and $\Omega = 2\pi(1 - \cos\alpha)$ is the solid angle of the directivity pattern for the receiving antenna [9]. The intensity of the incident sound beam was evaluated by the formula $I_i = \frac{I_c}{n_c^2}$, where $I_c = \frac{U_c^2}{S_a R}$ is the measured intensity of sound reflected from the cylinder (U_c is the voltage at the receiver input, and $S_a = \frac{\pi a^2}{4}$ is the antenna area) and n_c is the reflection coefficient for the short-wave region of sound waves ($\lambda \ll d$) [12]:

$$n_c^2 = \frac{I_c}{I_i} \approx \frac{d}{2r}\sin\frac{\theta}{2} + \frac{1}{\pi k_0 r}\cot^2\frac{\theta}{2}\sin^2\left(\frac{k_0 d}{2}\sin\theta\right).$$

Here, $r = \frac{D}{2\cos(\theta/2 - \varphi)}$ is the distance from the cylinder reflecting surface element to the reception point with $D \gg d$ and $r \gg d$.

Since the minimum length of a transmitted pulse $l = c\tau\sin\theta = 6$ cm (where $c \approx 1500$ m s^{-1} is the sound velocity) exceeds the sound-beam width of the receiving antenna, the scattering region coincides with the intersection zone for the directivity patterns, which can be approximated in this case by an ellipsoid with volume [13]

$$V = \frac{\pi}{6}\frac{(\alpha D_e)^3}{\cos^4\left(\frac{\theta}{2}\right)\sin\left(\frac{\theta}{2}\right)}.$$

Here, $D_e = D + \frac{a}{2\alpha}\cos\left(\frac{\theta}{2} - \varphi\right)$ is the base width of an equivalent bistatic configuration with dummy point antennas placed on the directivity-pattern axes at distances $\frac{a}{2\alpha}$ from the plane containing the actual antennas.

To compare the results obtained with the data of spectral analysis performed according to (3), we normalized the parameter m_V to its maximum value m_m:

$$m_e = \frac{m_V}{m_m}. \quad (4)$$

For checking the consistency of this parameter to the actual measurements, we transformed it into the dimensionless scattering cross section

$$\sigma = m_V\lambda, \quad (5)$$

which can serve as a similarity criterion for the bulk scattering.

The sonar was switched on immediately before the cylinder was placed into the sound-beam zone. Each transmitted acoustic pulse was accompanied by a consecutive choice of an 8-bit sound-scattering signal within the time interval $\Delta t = 2.2$ μs. This corresponded to a 85-cm-length section of the sound path with a resolution better than 0.2 cm. Our distance selector specified the position of this section, such that it contained the cylinder and the interface region behind it. When the cylinder moved in the sound-field region, the receiver amplification factor was set equal to 1 and the reference signal U_c was registered during this time. After removing the cylinder from the sound-field region, the amplification factor was fixed within the range from 2×10^3 to 4×10^3 depending on the sound-scattering intensity level.

Wake shadowgraphs are shown in Fig. 2. The cylinder moves in the tank along its longitudinal axis from the right to the left. At the initial stage, the cylinder is close to the left boundary of the visual field (Fig. 2a). In this regime, there exists a chain of large-scale vortices in the vicinity of the body which is accompanied by attached inner waves (their ridges and troughs are seen in Fig. 2 as dark arched open strips diverging up and down). The distance between neighboring strips is equal to half the wavelength $\frac{\lambda_i}{2} = \frac{UT_b}{2} = 9$ cm for these waves. The dark horizontal strip to the right from the wake axis, i.e., the central interface separating layers of different density, is hidden inside the intense vortices formed in the wake segment adjacent to the body. The vortices disappear with time, and the central interface evidently manifests itself against a background of less-contrasting concentration interlayers and microstructural nonuniformities (Fig. 2b).

In the course of repeated towages with a constant velocity, cocurrent flows with the same structure were reproduced (Fig. 2). Before each towage, we set a new

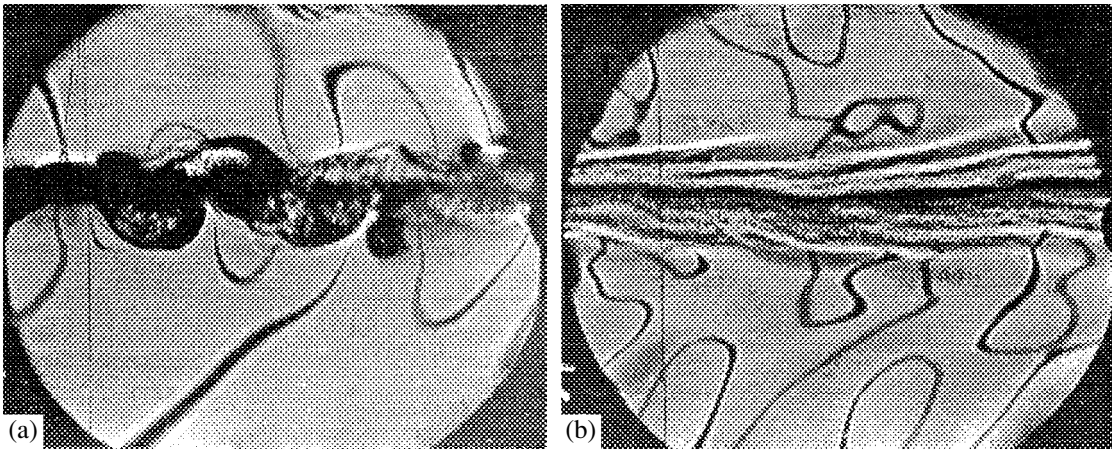

Fig. 2. Shadowgraph of the flow behind the cylinder d = 1.5 cm, U = 3 cm s^{-1}, Re = 430, Fr =1.7): (a) $t = 0.3T_b$; (b) $3T_b$.

angular disposition for the receiving and transmitting antennas and took shadowgraphs of the sound beams, which were then used to refine the angles θ and φ.

The normalized scattering cross sections are shown in Fig. 3 as functions of the resonance wave number $k = 2k_0\sin\frac{\theta}{2}$. All the data were obtained for the wake age $t = 3T_b$, i.e., when the central interface became virtually horizontal. In the case of the mirror reflection being absent, the experimental and calculated points are grouped near the curve $m_V \sim k^{-7}$. For a fixed angle θ, the variation of the angle φ (i.e., in the case of the rotation of the bistatic array as a whole) weakly affects the sound-scattering intensity for $\varphi \geqslant 0$ (points *5–7* for $k \approx 36$ cm^{-1}, i.e., for $\theta \approx 51°$). However, for $\varphi \approx 0°$, the same rotation results in a sharp decrease in the reflections (points *1* and *4* for $k = 42$ cm^{-1}, i.e., for $\theta = 60°$). Provided that the mirror reflection occurs, the experimental cross section, i.e., the ordinates of the points *1–3* ($\varphi \approx 0°$), exceed the cross section (3) calculated for the diffuse scattering by microstructural nonuniformities by a factor of about 50.

In our experiments, dimensionless cross section (5) for the diffuse bulk scattering ranges from 3×10^{-8} to 8×10^{-7} (see Fig. 4) and corresponds to the measured scattering by bioaggregations in the ocean [6]. For the mirror reflection, the cross section σ exceeds 2.5×10^{-6}. This lies far outside of actual measurement data, because the other effect, namely, the reflection from a thin layer, becomes most important. In such a situation, the dimensionless thickness $\xi = \frac{\delta}{\lambda}$ (δ is the absolute thickness) of a layer serves as a criterion for the consistency of laboratory-scale and natural-scale sea data. In our experiments and in [7], $\xi = 0.7$ ($\lambda = 0.15$ cm and $\delta \approx 0.1$ cm). However, in sea experiments, the reflecting layers with thickness δ from 1 to 20 cm were observed by acoustic sounding with a wavelength of $5 < \lambda <$ 20 cm. Therefore, the parameter ξ was within the range from 0.2 to 1 [3–5], i.e., close to the values obtained in the course of laboratory-scale measurements.

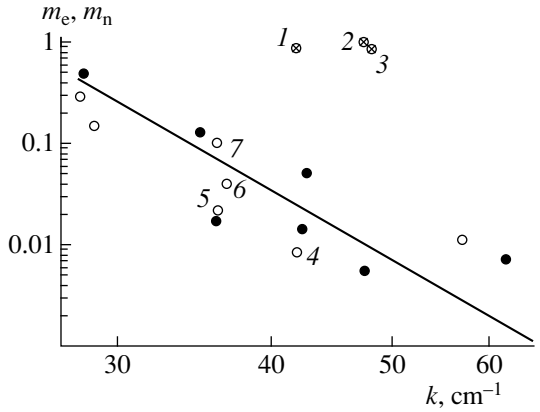

Fig. 3. Normalized scattering cross sections: (○) experimental data for m_e; (⊗ the case of mirror reflection; (●) calculation data for m_n obtained by formula (3); and (–) the dependence k^{-7} (solid line). The angle φ at the points *1* to *7* is equal, respectively, to 2°, 3°, 0°, 7°, 8°, 12°, and 13°.

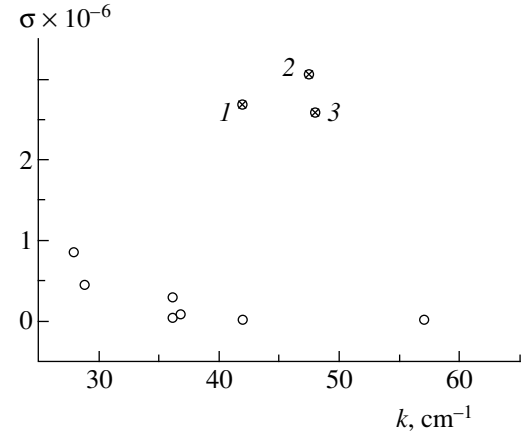

Fig. 4. Dimensionless cross section $\sigma = m_V\lambda$ in the case of bulk scattering.

ACKNOWLEDGMENTS

This work was supported in part by the Russian Foundation for Basic Research, projects nos. 97-01-01013 and 99-05-64980, and the Ministry of Science and Technology of the Russian Federation, Program of Supporting Unique Facilities and Equipment, project no. 02-01.

REFERENCES

1. M. A. Kallistratova and A. I. Kon, *Radio Acoustical Sounding of Atmosphere* (Nauka, Moscow, 1985).
2. D. W. Beran, W. H. Hooke, and S. F. Clifford, Boundary-Layer Meteorol. **4**, 133 (1973).
3. T. K. Stanton, P. H. Wiebe, D. Chu, and L. Goodman, ICES J. Mar. Sci. **51**, 469 (1994).
4. N. I. Sviridov and A. F. Kuleshov, Okeanologiya **16**, 529 (1996).
5. G. T. Kaye and V. C. Anderson, J. Acoust. Soc. Am. **66**, 842 (1979).
6. A. S. Salomatin, V. P. Shevtsov, and V. I. Yusupov, Akust. Zh. **31**, 768 (1985) [Sov. Phys. Acoust. **31**, 467 (1985)].
7. V. V. Mitkin, V. E. Prokhorov, and Yu. D. Chashechkin, Akust. Zh. **45**, 380 (1999) [Acoust. Phys. **45**, 336 (1999)].
8. V. E. Prokhorov and Yu. D. Chashechkin, Akust. Zh. **41**, 908 (1995) [Acoust. Phys. **41**, 804 (1995)].
9. L. M. Brekhovskikh and Yu. P. Lysanov, *Fundamentals of Ocean Acoustics* (Gidrometeoizdat, Leningrad, 1982; Springer-Verlag, New York, 1991).
10. A. S. Monin and A. M. Yaglom, *Statistical Hydromechanics* (Nauka, Moscow, 1967; MIT Press, Cambridge, 1975), Part 2.
11. D. E. Mowbray, J. Fluid Mech. **27**, 595 (1967).
12. P. Morse and K. Ingard, *Theoretical Acoustics* (McGraw-Hill, New York, 1968).
13. M. A. Kallistratova, Tr. Inst. Fiz. Atmos. Akad. Nauk SSSR, No. 4, 203 (1962).

Translated by V. Chechin

Doklady Physics, Vol. 46, No. 3, 2001, pp. 207–209. Translated from Doklady Akademii Nauk, Vol. 377, No. 3, 2001, pp. 332–334.

MECHANICS

Conditional Asymptotic Stability in the Joukowski Sense for a Periodic Orbit of a Nonlinear Differential Equation

O. V. Druzhinina

Presented by Academician V.V. Rumyantsev September 3, 2000

Received September 15, 2000

In this paper, we prove a theorem on the conditional asymptotic stability in the Joukowski sense for a periodic orbit of the nonlinear steady-state differential equation

$$\dot{x} = g(x), \quad g \in C^2(R^n \to R^n), \tag{1}$$

provided that the characteristic exponents of the corresponding variational equation have both negative and positive real parts. In this case, the structure of the periodic-orbit neighborhood for Eq. (1) is also clarified.

The semitrajectory $C^+(p)$ of the solution $\varphi(t, p)$ to Eq. (1) is referred to as stable in the Joukowski sense [1, 2] if, for every number $\varepsilon > 0$, a number $\delta = \delta(\varepsilon)$ can be found so that, for an arbitrary vector q, $|p - q| > \delta$, there exists a function $\sigma(t)$ for which the following inequality is valid:

$$|\varphi(t, p) - \varphi(\sigma(t), q)| \le \varepsilon \quad \forall t \in R^+.$$

Here, σ: $R^+ \longrightarrow R^+$ is the one-to-one continuous mapping (homeomorphism) of R^+ onto R^+, with $\sigma(0) = 0$.

If for a certain number $\Delta > 0$ and at every point q of the sphere $|p - q| > \Delta$, there exists the homeomorphism σ: $R^+ \longrightarrow R^+$ for which

$$\lim_{t \to +\infty} |\varphi(t, p) - \varphi(\sigma(t), q)| = 0,$$

then the semitrajectory $C^+(p)$ of the solution $\varphi(t, p)$ is referred to as asymptotically stable in the Joukowski sense [1, 2].

In [3–5], problems on the asymptotic orbital stability of a periodic trajectory for Eq. (1) were considered in the case when, along a periodic solution $\gamma(t)$ to Eq. (1), the variational equation

$$\dot{z} = g_x(\gamma(t))z \tag{2}$$

has one zeroth characteristic exponent and $n - 1$ characteristic exponents with negative real parts.

Russian Open State Technical University of Railway Communication, ul. Chasovaya 22/2, Moscow, 125808 Russia

It is evident that, for the state of equilibrium of Eq. (1), the notions of the stability in the Lyapunov sense and of the orbital stability and strength in the Joukowski sense are equivalent.

We show that, in the case of a periodic trajectory $C(p)$ of the solution $\gamma(t) \not\equiv$ const, the notions of the orbital stability and stability in the Joukowski sense are equivalent. Indeed, the orbital stability of the periodic trajectory $C(p)$ follows from its stability in the Joukowski sense. Inversely, we assume that the periodic trajectory $C(p)$ of the periodic motion $\gamma(t, p)$ is orbitally stable; i.e., the following inequality is fulfilled:

$$\rho(\gamma(t, q), C(p)) < \varepsilon \quad \forall t \in R^+.$$

Here, ρ is the distance between the periodic trajectory $C(p)$ of the motion $\gamma(t, p)$ and the point $\gamma(t, q)$, with $q \ne p$.

Because the function $\gamma(t, p)$ is continuous and the set $C(p)$ is compact, the value $\rho[\gamma(t, q), C(p)]$ is always achieved at a certain vector $\gamma(t, q) - \gamma(\sigma, p)$, where $\sigma \in R$, with σ depending on t. Thereby, the mapping $t \longrightarrow \sigma = \sigma(t)$ is defined. If the number $\varepsilon > 0$ is chosen to be sufficiently small, the ε-neighborhood of $C(p)$ has no self-intersections; i.e.,

$$U_{t_1} \cap U_{t_2} = \emptyset \ \forall t_1 \ne t_2, \quad t_1, t_2 \in [0, \omega],$$

$$U_t = \{y: |y - \gamma(t, p)| < \varepsilon, (y - \gamma(t, p))^* g(\gamma(t, p)) = 0\}.$$

Here, the asterisk is the transposition. In this case, the mapping $t \longrightarrow \sigma(t)$ determines reparametrization of the trajectory $C(p)$ and, consequently, the inequality $|\gamma(\sigma(t), p) - \gamma(t, q)| < \varepsilon$ is fulfilled; this implies that the periodic trajectory $C(p)$ is stable in the Joukowski sense. In the general case, the notions of orbital stability and stability in the Joukowski sense are not equivalent for trajectories differing from the equilibrium state and the periodic trajectory.

The following theorem is valid.

Theorem. *Let $\gamma(t)$ be a periodic solution with period ω to nonlinear steady-state equation* (1)*, and let the*

1028-3358/01/4603-0207$21.00

real parts α_s, $s = 1, \ldots, k$ *of the characteristic exponents of Eq.* (2) *be arranged in increasing order,*

$$\alpha_1 < \ldots < \alpha_k, \tag{3}$$

and have multiplicities $n_1, n_2, \ldots, n_k$, *respectively, with* $\alpha_i = 0$ for $i = n_1 + n_2 + \ldots + n_k + 1$.

In this case, there exist the manifolds M_s ($s = 1, 2, \ldots, k$) *having dimensions* $n_1 + n_2 + \ldots + n_s$, *respectively, and the number* $\mu > 0$, *such that, if there exists a number* t_1: $|p - \gamma(t_1)| < \mu$, $p \in M_s$, *the following asymptotic representation is valid*:

$$|\varphi(t, t_0, p) - \gamma(t - t_0)| = o(e^{(\alpha_s + \varepsilon)t}), \quad \varepsilon > 0, \quad s = 1, 2, \ldots, k. \tag{4}$$

If there exists $t_1 \in R$: $|p - \gamma(t_1)| < \mu$, $x_0 \neq M_s$, *the following asymptotic representation is valid*:

$$|\varphi(t, t_0, p) - \gamma(t - t_0)| \neq O(e^{(\alpha_s - \varepsilon)t}), \quad \varepsilon > 0, \quad s = 1, 2, \ldots, k. \tag{5}$$

Furthermore, if there exists $t_1 \in R$: $|p - \gamma(t_1)| < \mu$, $p \in M_i$, *then*

$$\exists \Delta \in R\colon |\varphi(t, t_0, p) - \gamma(t - \Delta)| = o(e^{(\alpha_{i-1} + \varepsilon)t}), \quad \varepsilon > 0. \tag{6}$$

Proof. Let $\varphi(t, t_0, p)$ be the solution to Eq. (1), such that $\varphi(t, t_0, p) = p$ and $\gamma(t)$ are the periodic solution to Eq. (1) with a shortest period ω. The trajectory C passing through the point $\gamma(0)$ is a simple closed curve. For any $h > 0$, the function $\gamma(t + h)$ is the solution to Eq. (1) and the quantity $|\gamma(t + h) - \gamma(t)|$ does not tend to zero as $t \longrightarrow +\infty$; hence, the solution $\gamma(t)$ to Eq. (1) cannot be asymptotically stable in the Lyapunov sense [5]. Assuming that $y(t) = x(t) - \gamma(t)$ and using the Taylor formula, we obtain

$$g(x(t)) = g(\gamma(t)) + g_x(\gamma(t))y(t) + G(t, y(t)), \tag{7}$$

where $G(x(t)) = o(|y|)$. By virtue of (1), we have

$$\dot{y} = g_x(\gamma(t))y + G(t, y). \tag{8}$$

The matrix $A(t) \equiv g_x\{\gamma(t)\}$ is periodic with period ω. Since

$$\frac{d}{dt}(\dot{\gamma}(t)) = g_x(\dot{\gamma}(t))\dot{\gamma}(t),$$

the derivative $\dot{\gamma}(t)$ is the periodic solution to variational equation (2) in $\gamma(t)$.

The term $G(t, y)$ in Eq. (8) has the properties

$$G(t, y) = o(|y|), \quad G(t, 0) \equiv 0, \tag{9.1}$$

$$\exists c_1 > 0, \quad \exists \mu\colon |y| < \mu \Rightarrow |G(t, y_1) - G(t, y_2)| < c_1|y_1 - y_2|. \tag{9.2}$$

For further proof of the theorem, we use the following proposition.

Proposition [6, 7]. *Let variational equation* (2) *have characteristic exponents with real parts* α_s, $s = 1, 2, \ldots, k$, *with* $\alpha_1 < \ldots < \alpha_k$ *and satisfy the conditions of exponential dichotomy; i.e., for a fundamental matrix* $X(t)$ *of Eq.* (2), *the following inequalities are fulfilled*:

$$|X(t)PX^{-1}(s)| \leq c_3 \exp\{-a(t - s)\}, \quad t \geq s,$$

$$|X(t)QX^{-1}(s)| \leq c_4 \exp\{b(t - s)\}, \quad t \leq s.$$

Here, c_3, c_4, a, *and* b *are positive constants and* P *and* Q *are the additional projections onto* R_n. *Let the function* $f(t)$ *be such that*

$$|G(t, y)| \leq f(t) \ \forall y \in R^n$$

and the integral

$$F(t) = \int_t^{t+1} f(t)dt$$

be a bounded function. In this case, there exists a manifold $M(t_0)$, *with its dimension equal to the rank of the matrix* P, *such that the solution* $y(t, t_0, p)$ *to Eq.* (8) *is bounded in* R^+ *if and only if* $p \in M(t_0)$.

By virtue of this proposition, there exist manifolds $M_s(0)$ and numbers μ_s, $s = 1, 2, \ldots, k$, such that

$$|q| < \mu_s \Rightarrow \lim_{t \to +\infty} \sup t^{-1} \log|y(t, 0, q)| \leq \alpha_s \ \forall q \in M_s,$$

$$|q| < \mu_s \Rightarrow \lim_{t \to +\infty} \sup t^{-1} \log|y(t, 0, q)| \geq \alpha_{s+1} \ \forall q \notin M_s.$$

We define the manifolds:

$$M_s = \gamma(0) + M_s(0), \quad s = 1, 2, \ldots, k. \tag{10}$$

It follows from (10) that if $|p - \gamma(t_1)| < \mu_s$, $p \in M_s$, then

$$|\varphi(t, t_0, p) - \gamma(t - t_0)| = |y(t, 0, q)| = o(e^{(\alpha_s + \varepsilon)t}), \quad \varepsilon > 0, \tag{11}$$

if $|p - \gamma(t_1)| < \mu_s$, $p \notin M_s$.

If $|p - \gamma(t_1)| < \mu_s$, $p \notin M_s$, then

$$|\varphi(t, t_0, p) - \gamma(t - t_0)| = |y(t, 0, q)| \neq O(e^{(\alpha_s - \varepsilon)t}), \quad \varepsilon > 0. \tag{12}$$

It follows from (11) and (12) that asymptotic representations (4) and (5) are valid. Now, we prove statement (6). With this purpose, the coordinates are changed, so that the matrix R in the representation

$X(t) = P(t)\exp\{Rt\}$ [where $P(t)$ is a periodic matrix and R is a constant matrix] takes the form

$$R = \begin{Vmatrix} R_1 & \dots \\ \dots\ 0 & \dots \\ \dots & R_2 \end{Vmatrix}.$$

Here, the matrices R_1 and R_2 have eigenvalues with positive and negative real parts, respectively, and the $(m + 1)$th diagonal element is zero. It is evident that $\dot{\gamma}(0) = e_{m+1}$ is the $(m + 1)$th column of the unit matrix E_n having dimension $n \times n$.

The tangential space $T_{i-1}(p)$ of the manifold M_{i-1} at the point p is a null-space for $d_q\Pi(q + h(0, q))|_{p-\gamma(0)}$, where Π is the natural projection onto the last $n - m$ coordinates of the space R^n and the function $h(t_0, q)$ is determined by the formula [4]

$$h(t_0, q) = -\int_{-\infty}^{t_0} X(t_0)PX^{-1}(s)G(s, \varphi(s, t_0, q))ds + \int_{t_0}^{+\infty} X(t_0)QX^{-1}(s)G(s, \varphi(s, t_0, q))ds.$$

It is evident that $y(\tau, 0, q) \equiv 0$ for $q = 0$ because $d_yG(\tau, y(\tau, 0, 0)) = 0$ [4, 5].

It is also easy to verify that $d_qh(0, q)|_0 = 0$, and, therefore, $T_{i-1}(\gamma(0))$ is the null-space for $[O_{(n-m)\times m}E_{n-m}]$ [4]. Because $\dot{\gamma}(0) \notin T_{i-1}(\gamma(0))$, the solution $\gamma(t)$ transversely intersects the manifold M_{i-1} at the points $\varphi(0)$, $\varphi(\pm\omega)$, $\varphi(\pm 2\omega)$, …. If there exists t_1: $|p - \gamma(t_1)| < \mu$, with $p \in M_i$, then $\varphi(t, t_1, p) \in M_i$ for all t; i.e., the difference $\varphi(t, t_1, p) - \varphi(t - t_1)$ increases exponentially. By virtue of (4), this is impossible for $\alpha_s = 0$.

It is easy to prove that the manifolds M_{i-1} and M_i are separated from one another.

There is a moment in the time interval $[t_1, t_1 + \omega]$ at which the trajectory $\gamma(t - t_1)$ transversely intersects the manifold M_{i-1}. Because the solution to Eq. (7) and $T_{i-1}(p)$ continuously depend, respectively, on the totality (t, t_0, p) and on p, the number μ can be chosen so small that

$$\exists t_2 \in R \quad \varphi(t_2, t_1, p) \in M_i.$$

It follows from (4) and (5) that

$$|\varphi(t, t_2, \varphi(t_2, t_1, p)) - \gamma(t - t_2)| = o(e^{(\alpha_{i-1}+\varepsilon)t}), \quad \varepsilon > 0.$$

Substituting t by $t + t_1 - t_0$ and denoting $\Delta = t_0 - t_1 + t_2$, we arrive at statement (6).

The theorem is a generalization and an extension of the results of [6, 7].

ACKNOWLEDGMENTS

The author is sincerely grateful to A.A. Shestakov and V.V. Rumyantsev for their attention to this work.

REFERENCES

1. O. V. Dunaeva and A. A. Shestakov, *Stability of Mechanical-System Motion* (RUDN–PAIMS, Moscow, 1996).
2. O. V. Dunaeva, Dokl. Akad. Nauk **362**, 198 (1998) [Dokl. Phys. **43**, 583 (1998)].
3. P. Hartman, *Ordinary Differential Equations* (Wiley, New York, 1964; Mir, Moscow, 1970).
4. W. A. Coppel, *Stability and Asymptotic Behavior of Differential Equations* (Heath, Boston, 1965).
5. E. A. Coddington and N. Levinson, *Theory of Ordinary Differential Equations* (McGraw-Hill, New York, 1955; Inostrannaya Literatura, Moscow, 1958).
6. W. A. Coppel, J. Diff. Eqns. **3**, 500 (1967).
7. W. A. Coppel, J. Diff. Eqns. **4**, 386 (1968).

Translated by V. Bukhanov

Doklady Physics, Vol. 46, No. 3, 2001, pp. 210–214. Translated from Doklady Akademii Nauk, Vol. 377, No. 3, 2001, pp. 335–339.

MECHANICS

On the Asymmetry of Kirkwood Gaps in the Asteroid Belt

A. P. Markeev

Presented by Academician V.V. Rumyantsev September 14, 2000

Received September 19, 2000

1. INTRODUCTION

For Kirkwood gaps, there exists a commensurability between the mean motions n and n' of an asteroid and Jupiter, respectively: namely, the ratio $\frac{n}{n'}$ is close to a rational number $\frac{l}{s}$. The number $l - s$ is referred to as the order of commensurability or the resonance order.

At the same time, there exists an asymmetry in the positions of Kirkwood gaps. Indeed, the centers of the gaps observed are displaced towards Jupiter with respect to exactly commensurate positions. A number of studies were devoted to the problem of this asymmetry (see, e.g., [1]).

In this paper, based on a two-dimensional circular bounded three-body problem, we indicate possible dynamic causes for the asymmetry in positions of Kirkwood gaps. In doing so, we simulate asteroid orbits with the help of periodic solutions of the first kind.

2. PERIODIC MOTIONS

Let two material points S and J (the Sun and Jupiter) move in circular orbits around their center of mass O with an angular velocity n'. Let a negligibly small mass point P move in the orbital plane of the mass points S and J and be attracted by them according to the Newtonian law of universal gravitation. We take the polar coordinates r and φ as generalized coordinates of the point P. Here, r is the distance OP from the point P toward the center of mass for the points S and J and φ is the angle between the vector $\overline{OP}$ and the vector $\overline{SJ}$ rotating with angular velocity n'. The corresponding generalized momenta are denoted by p_r and p_φ. We take the total mass of the points S and J and the distance between them to be unity. We denote the mass of the point J by μ ($0 < \mu \ll 1$) and take the dimensionless quantity $\nu = n't$ as an independent variable. In this case, the Hamiltonian has the form

$$H = \frac{1}{2}\left(p_r^2 + \frac{p_\varphi^2}{r^2}\right) - p_\varphi - \frac{1-\mu}{r_1} - \frac{\mu}{r_2},$$

$$r_1 = \sqrt{r^2 + 2\mu r\cos\varphi + \mu^2}, \qquad (1)$$

$$r_2 = \sqrt{r^2 - 2(1-\mu)r\cos\varphi + (1-\mu)^2}.$$

For $\mu = 0$, the equations of motion admit a partial solution corresponding to circular motion of the point P around the point S:

$$r = R, \quad \varphi(\nu) = \Omega\nu + \varphi(0), \quad p_r = 0,$$
$$p_\varphi = \sqrt{R}, \quad \Omega = R^{-3/2} - 1, \quad R = \left(\frac{n}{n'}\right)^{-2/3}. \qquad (2)$$

Here, R is a constant. We assume that $0 < R < 1$. For solution (2), we have

$$H = h_0 = \text{const}, \quad h_0 = -\frac{2R^{3/2} + 1}{2R}.$$

For small but nonzero μ, we take solution (2) as a generating solution. In the case of the bounded three-body problem, a lot of studies are devoted to finding periodic solutions that, for $\mu = 0$, transform into a generating circular solution and to using these solutions for analyzing asteroid dynamics [2]. We construct these solutions (the Poincaré solutions of the first kind) in the following manner. We express the energy-integral constant $H = h$ = const as a power series $h = h_0 + \mu h_1 + \mu^2 h_2 + \ldots$ and resolve the equality $H = h$ with respect to p_φ. As a result, we have

$$p_\varphi = -K = r^2 + r\sqrt{F} + \mu r\frac{V(r,\varphi) + h_1}{\sqrt{F}} + \ldots, \qquad (3)$$

Institute of Problems in Mechanics,
Russian Academy of Sciences,
pr. Vernadskogo 101, Moscow, 117526 Russia

1028-3358/01/4603-0210$21.00

$$F = 2h_0 + r^2 - p_r^2 + \frac{2}{r},$$
$$V(r, \varphi) = \frac{1}{\sqrt{1 - 2r\cos\varphi + r^2}} - \frac{1}{r} - \frac{\cos\varphi}{r^2}. \quad (4)$$

For the isoenergetic level $H = h$, the equations of motion take the Hamiltonian form (Whittaker equations [3]):

$$\frac{dr}{d\varphi} = \frac{\partial K}{\partial p_r}, \quad \frac{dp_r}{d\varphi} = -\frac{\partial K}{\partial r}. \quad (5)$$

We seek the solutions $r^*(\varphi)$ and $p_r^*(\varphi)$ to set (5), which are analytical with respect to μ and 2π-periodic in φ, as the series

$$r = r^* = R + \mu f(\varphi) + \ldots,$$
$$p_r = p_r^* = \mu g(\varphi) + \ldots \quad (6)$$

The functions f and g satisfy the equations

$$\frac{df}{d\varphi} = \frac{1}{\Omega} g,$$
$$\frac{dg}{d\varphi} = -\Omega\omega^2 f + \frac{2(\Omega + 1)(V_0 + h_1)}{\Omega^2 R} + \frac{1}{\Omega}\frac{\partial V_0}{\partial R}, \quad (7)$$

where

$$\omega = \omega(R) = \frac{\Omega + 1}{\Omega} = \frac{1}{1 - R^{3/2}}. \quad (8)$$

Here, V_0 is the function $V(r, \varphi)$ from (4) evaluated at $r = R$, which can be expressed as a Fourier series [4]:

$$V_0 = \left(\frac{1}{2}L_1^{(0)} - \frac{1}{R}\right) + \left(L_1^{(1)} - \frac{1}{R^2}\right)\cos\varphi + \sum_{n=2}^{\infty} L_1^{(n)}\cos n\varphi,$$

where $L_1^{(n)} = L_1^{(n)}(R)$ are the Laplace coefficients.

If ω is not an integer (i.e., there exists no resonance of the first order), the periodic solution to Eq. (7) takes the form of a Fourier series:

$$f = \sum_{n=0}^{\infty} f_n \cos n\varphi, \quad g = -\Omega\sum_{n=1}^{\infty} n f_n \sin n\varphi, \quad (9)$$

$$f_0 = -\frac{(\Omega + 2)}{\Omega(\Omega + 1)^2 R^2} + \frac{1}{(\Omega + 1)^2}\left[\frac{(\Omega + 1)(L_1^{(0)} + 2h_1)}{\Omega R} + \frac{1}{2}\frac{dL_1^{(0)}}{dR}\right],$$

$$f_1 = -\frac{2}{(2\Omega + 1)\Omega R^3} + \frac{1}{2\Omega + 1}\left[\frac{2(\Omega + 1)L_1^{(1)}}{\Omega R} + \frac{dL_1^{(1)}}{dR}\right],$$

$$f_n = \frac{1}{\Omega^2(\omega^2 - n^2)}\left[\frac{2(\Omega + 1)L_1^{(n)}}{\Omega R} + \frac{dL_1^{(n)}}{dR}\right].$$

The dependence of the momentum p_φ on φ is determined from (3), (4), and (6):

$$p_\varphi = p_\varphi^* = \sqrt{R} + \mu\frac{V_0 + h_1}{\Omega} + \ldots \quad (10)$$

Functions (6) and (10) are 2π-periodic in the angle φ. The dependence of this angle on the dimensionless "time" ν is determined by the equation

$$\frac{d\varphi}{d\nu} = \frac{\partial H}{\partial p_\varphi} = \frac{p_\varphi}{r^2} - 1.$$

Substituting r and p_φ from (6) and (10) into this equation, we have

$$\frac{d\varphi}{d\nu} = \Omega + \mu G(\varphi) + \ldots, \quad (11)$$

where

$$G(\varphi) = -\frac{2(\Omega + 1)}{R} f + \frac{V_0 + h_1}{\Omega R^2}. \quad (12)$$

The period in terms of ν is equal to the time interval T for which the angle φ takes the increment of 2π. From (9), (11), and (12), we find that $T = \frac{2\pi}{\Omega_1}$, where $\Omega_1 = \Omega + \mu\bar{G} + O(\mu^2)$ and

$$\bar{G} = \frac{1}{2\pi}\int_0^{2\pi} G(\varphi)d\varphi$$
$$= \frac{(\Omega + 1)(\Omega + 3)}{\Omega} - \frac{3(L_1^{(0)} + 2h_1)}{2\Omega R^2} - \frac{1}{(\Omega + 1)R}\frac{dL_1^{(0)}}{dR}.$$

The energy-integral constant is a significant parameter determining the periodic solution obtained. In particular, it is possible to choose $h_1, h_2, \ldots$ such that the period of the solution is equal to that of the generating circular motion.

3. THE HAMILTONIAN OF THE PERTURBED MOTION

In the vicinity of the periodic solution, we introduce the perturbances q, p, and I with the help of the canonical transformation

$$r = r^* + q, \quad p_r = p_r^* + p, \quad \varphi = w,$$
$$p_\varphi = p_\varphi^* + q\frac{dp_r^*}{d\varphi} - p\frac{dr^*}{d\varphi} + I.$$

In the expansion of Hamiltonian (1) in a power series of q, p, and I, the factor standing at the term I

coincides with the right-hand side of Eq. (11). Instead of the variables φ and I, we introduce the new canonically conjugate variables φ_1 and I_1 using the generating function

$$S(\varphi, I_1) = I_1\left(\varphi - \frac{\mu}{\Omega}\int\tilde{G}(\varphi)d\varphi - \ldots\right),$$

$$\tilde{G}(\varphi) = G(\varphi) - \bar{G}.$$

In this case, in the series expansion of the Hamiltonian for the perturbed motion, the factor multiplying I_1 coincides with the frequency Ω_1 of the unperturbed periodic motion. We then make the change of variables

$$q = (\Omega + 1)^{-1/2}q_2, \quad p = (\Omega + 1)^{1/2}p_2$$

and introduce the new independent variable $\tau = \Omega_1\nu$. As a result, the Hamiltonian of the perturbed motion is rewritten as the following series (with the above denotation φ retained for the new angular variable φ_1):

$$H = H_2 + H_3 + H_4 + \ldots + H_m + \ldots. \tag{13}$$

Here, H_m is a form of the mth degree with respect to $|I_1|^{1/2}$, q_2, and p_2, with

$$H_2 = I_1 + \frac{1}{2}\omega(q_2^2 + p_2^2)$$

$$+ \mu(h_{20}q_2^2 + h_{11}q_2p_2 + h_{02}p_2^2) + O(\mu^2),$$

$$h_{20} = \frac{3(V_0 + h_1)}{\Omega^2R^2} - \frac{3(\Omega + 1)}{\Omega R}f$$

$$- \frac{2}{\Omega R}\frac{dg}{d\varphi} - \frac{\Omega + 1}{2\Omega^2}\bar{G} - \frac{1}{2\Omega(\Omega + 1)}\frac{\partial^2V_0}{\partial R^2},$$

$$h_{11} = \frac{2(\Omega + 1)}{\Omega^2R}g, \quad h_{02} = -\frac{\Omega + 1}{2\Omega^2}\bar{G},$$

$$H_3 = -2\frac{\sqrt{\Omega + 1}}{\Omega R}I_1q_2 - \frac{\sqrt{\Omega + 1}}{\Omega R}q_2^3 + O(\mu),$$

$$H_4 = \frac{1}{2\Omega R^2}I_1^2 + \frac{3}{\Omega R^2}I_1q_2^2 + \frac{3}{2\Omega R^2}q_2^4 + O(\mu).$$

4. CHARACTERISTIC EXPONENTS AND DISPLACEMENT OF THE KIRKWOOD-GAP CENTERS

The term H_2 in Hamiltonian (13) corresponds to a linearized set of equations for a perturbed motion. Two characteristic exponents for this set vanish. Two other exponents, $\pm i \times 2\pi\lambda$, become purely imaginary for sufficiently small μ provided that resonance of the second order (parametric resonance) does not exist. The quantity λ can be treated (if the quantity $\tau = \Omega_1 n' t$ serves as the time) as one of the frequencies of small-amplitude oscillations in the vicinity of the periodic motion under consideration.

If μ is sufficiently small, then λ is an analytical function of μ and can be expanded into a series:

$$\lambda = \lambda_0 + \mu\lambda_1 + \ldots, \tag{14}$$

where $\lambda_0 = \omega$ and λ_1 is determined by the formula

$$\lambda_1 = \frac{1}{2\pi}\int_0^{2\pi}(h_{20} + h_{02})d\varphi = -\frac{(\Omega + 1)R^3}{4\Omega}\frac{d^2L_1^{(0)}}{dR^2}$$

$$+ \frac{(\Omega + 1)(2 - \Omega)R^2}{2\Omega^2}\frac{dL_1^{(0)}}{dR} \tag{15}$$

$$+ \frac{3(\Omega + 1)^2R}{2\Omega^3}(L_1^{(0)} + 2h_1) - \frac{(\Omega + 1)(\Omega + 3)}{\Omega^3}.$$

Let the exact commensurability $\frac{n}{n'} = \frac{k}{k - m}$ take place for $R = R_0$. In this case, resonance of the mth order occurs; i.e., $m\omega_0 = k$, where $\omega_0 = \omega(R_0)$. However, for $\mu \neq 0$, the value of $R = R_\mu$ distinct from R_0 corresponds to resonance of the mth order. This value must obey the resonance relationship

$$m\lambda = k. \tag{16}$$

Here, λ is determined by formula (14). From (8) and (16), we arrive at the following expression for the quantity $\delta = R_\mu - R_0$:

$$\delta = -\mu\frac{\lambda_1(R_0, h_1)}{\omega_0'} + O(\mu^2),$$

$$\omega_0' = \frac{d\omega_0}{dR_0} = \frac{3\omega_0^2\sqrt{R_0}}{2}. \tag{17}$$

With the parameter μ known and the given commensurability of $\frac{n}{n'}$, formula (17) determines the displacements of the Kirkwood-gap centers. We now consider the concrete periodic motions with a period equal to that of the generating circular motion. Then,

$$h_1 = \frac{1}{3}(\Omega + 1)(\Omega + 3)R^2 - \frac{1}{2}L_1^{(0)} - \frac{\Omega R}{3(\Omega + 1)}\frac{dL_1^{(0)}}{dR}.$$

Taking into account the equality $L_1^{(0)} = \frac{4K(R)}{\pi}$, where $K(R)$ is the complete elliptic integral of the first kind,

we obtain from (15) and (17) the following expression for the quantity δ:

$$\delta = \mu\frac{2R_0^{3/2}}{3\pi\omega_0}\left[R_0\frac{d^2K(R_0)}{dR_0^2} + 2\frac{dK(R_0)}{dR_0}\right] + O(\mu^2).$$

For sufficiently small μ, δ is positive; i.e., for small μ, the gap centers are displaced from the position R_0 towards greater R (i.e., towards Jupiter).

5. ON THE STABILITY OF PERIODIC MOTIONS AT THE BOUNDARIES OF PARAMETRIC-RESONANCE DOMAINS

We assume that the value of 2ω is close to an odd number $2N + 1$; i.e., the ratio $\frac{n}{n'}$ is close to a rational number $\frac{2N+1}{2N-1}$, with $N = 1, 2, 3, \ldots$ The stability of periodic solutions to the bounded three-body problem under such a commensurability has been studied for many years [5, 6] (see the corresponding review in monograph [2]).

Let the equality $2\omega_0 = 2\omega(R_0) = 2N + 1$ be valid for $R = R_0$. For values of R close to R_0, we assume that $R = R_0 + \Delta$, with $|\Delta| \ll 1$. Then,

$$2N + 1 - 2\omega = 2\mu\alpha, \quad (18)$$

where, according to (18) and (8),

$$\alpha = -\frac{\omega_0'}{\mu}\Delta + O(\Delta^2). \quad (19)$$

Using the algorithm given in paper [7], we can make the change of variables $q_2, p_2, \varphi_1, I_1 \longrightarrow \xi_2, \eta_2, \xi_1, \eta_1$ (which is canonical and analytical with respect to μ, ξ_2, η_2, and η_1, and 2π-periodic in ξ_1) such that the Hamiltonian of the perturbed motion is reduced to the form

$$\Gamma = \Gamma_2 + \Gamma_4 + \ldots + \Gamma_m + \ldots$$

Here, the term Γ_m is a form of the mth degree with respect to $|\eta_1|^{1/2}$, ξ_2, and η_2, with its coefficients being 2π-periodic in ξ_1 and

$$\Gamma_2 = \eta_1 + \frac{1}{2}\lambda(\xi_2^2 + \eta_2^2) + \sigma\left[-\frac{1}{2}(\xi_2^2 - \eta_2^2)\cos k\xi_1 + \xi_2\eta_2\sin k\xi_1\right],$$

$$\Gamma_4 = c_{20}\eta_1^2 + \frac{1}{2}c_{11}(\xi_2^2 + \eta_2^2)\eta_1 + \frac{1}{4}c_{02}(\xi_2^2 + \eta_2^2)^2 + O(\mu).$$

In these formulas,

$$k = 2N + 1, \quad \lambda = N + \frac{1}{2} - \mu(\alpha - \lambda_1) + O(\mu^2),$$
$$\sigma = \mu\chi + O(\mu^2),$$

where λ_1 and α are given by (15) and (19) and χ is found from the relationship

$$\chi = \chi(R) = \frac{1}{2\pi}\int_0^{2\pi}[h_{11}\sin k\varphi + (h_{02} - h_{20})\cos k\varphi]d\varphi.$$

The coefficients c_{ij} in the function Γ_4 are determined by the equalities

$$c_{20} = \frac{1}{2}c_{11} = c_{02} = -\frac{3}{2\Omega R^2}. \quad (20)$$

For small μ, the parametric-resonance domains (i.e., the orbital-instability domains for the periodic solution under consideration) are defined by the inequality $|\alpha - \lambda_1| < |\chi|$. They are wedge domains on the R, μ plane starting from the points $R = R_0$ in the axis $\mu = 0$. The boundaries γ_+ and γ_- of these domains are defined, respectively, by the equations

$$R = R_0 + \mu a + O(\mu^2), \quad R = R_0 + \mu b + O(\mu^2), \quad (21)$$

where $a = \frac{|\chi| - \lambda_1}{\omega_0'}$ and $b = -\frac{|\chi| + \lambda_1}{\omega_0'}$.

For sufficiently small μ, there is either orbital stability or instability on the boundary of the parametric-resonance domain, depending on whether the signs of the quantities $a_{02} = c_{20}\left(N + \frac{1}{2}\right)^2 - c_{11}\left(N + \frac{1}{2}\right) + c_{02}$ and $\alpha - \lambda_1$ are, respectively, distinct or equal [7].

However, it follows from (20) that

$$a_{02} = -\frac{3(2N-1)^2}{8\Omega R^2} < 0.$$

From (19) and (21), we can prove that the inequalities $\alpha < \lambda_1$ and $\alpha > \lambda_1$ are satisfied, respectively, on the boundaries γ_+ and γ_-. Therefore, for sufficiently small μ, the Poincaré periodic solution under consideration is orbitally stable on γ_- and unstable on γ_+. This is one more of the possible dynamic causes $\left(\text{corresponding to the commensurability of } \frac{n}{n'} = \frac{2N+1}{2N-1}\right)$ for the asymmetry of positions of gap centers in the asteroid belt,

because, with μ given, the points on the boundary γ_+ are located closer to Jupiter than those on the boundary γ_-.

ACKNOWLEDGMENTS

This work was supported in part by the Russian Foundation for Basic Research, project no. 99-01-00405, and the Federal Purposeful Program "Integratsiya," project no. A0097.

REFERENCES

1. V. G. Demin and S. G. Zhuravlev, Itogi Nauki Tekh., Ser. Astron. **15**, 2 (1979).
2. A. D. Bryuno, *The Limited Three-Body Problem* (Nauka, Moscow, 1990).
3. A. P. Markeev, *Theoretical Mechanics* (CheRo, Moscow, 1999).
4. E. P. Aksenov, *Special Functions in Celestial Mechanics* (Nauka, Moscow, 1986).
5. W. W. Heinrich, Astron. Nachr. **192** (20), 325 (1912).
6. H. Zeipel, Ark. Mat., Astron. Fys. **10** (30), 1 (1915).
7. A. P. Markeev, Prikl. Mat. Mekh. **64** (5), 833 (2000).

Translated by V. Chechin

Doklady Physics, Vol. 46, No. 3, 2001, pp. 215–218. Translated from Doklady Akademii Nauk, Vol. 377, No. 3, 2001, pp. 340–343.

MECHANICS

Cross Transport Phenomena in Disperse Systems Interacting with a High-Frequency Electromagnetic Field

R. I. Nigmatulin, F. L. Sayakhov, and L. A. Kovaleva

Presented by Academician G.G. Chernyĭ October 17, 2000

Received September 11, 2000

Conventional (so-called direct) transport phenomena are described by the empirical Fick law, Fourier law, Newton's law, Ohm's law, etc. However, the presence in a medium of external physical fields gives rise to the appearance of a large number of cross effects resulting from interaction between the medium and the fields. The well-known Soret effect, Dufour effect, Peltier effect, etc. are among them. To date, cross effects have been thoroughly studied only in the case of steady electromagnetic fields [1–3]. The action of a high-frequency electromagnetic field was mainly considered in the case of homogeneous systems with primary attention aimed at obtaining averaged relationships for linearly polarizable media in the case of a high-frequency electromagnetic field which is close to monochromatic [4].

BASIC NOTIONS AND ADMISSIONS

Studying transport phenomena in disperse multicomponent systems subjected to the action of an electromagnetic field is of interest from the applied point of view. We imply the high-frequency range, since for many media (in particular, for those employed in oil technology), it is this range that corresponds to the maximum dissipation of electromagnetic energy and its transformation into heat. While considering a high-frequency electromagnetic field in continua, we assume that it represents a quasi-monochromatic field [5]. We also suppose that there are no chemical reactions in the medium under consideration and that external bulk forces are absent. Then, in the case of a polarizable nonmagnetic dielectric, the following equations of state are valid:

$$\dot{\mathbf{D}} = \varepsilon_0 \dot{\varepsilon}(\omega, \rho, T)\dot{\mathbf{E}}, \quad \dot{\mathbf{B}} = \mu_0 \dot{\mathbf{H}}. \tag{1}$$

We assume also that in the case of an isotropic and homogeneous medium, the additivity condition for the permittivity of each component is fulfilled:

$$\dot{\varepsilon}(\omega, \rho, T) = \frac{1}{\rho}\sum_k \rho_k \dot{\varepsilon}_k = \sum_k C_k \dot{\varepsilon}_k, \tag{2}$$

where the dielectric constant of the kth component depends, in general, on the field frequency ω, the density ρ, and the ambient temperature T of the medium and

$$\dot{\varepsilon}_k = \varepsilon_k'(\omega, \rho, T) - i\varepsilon_k''(\omega, \rho, T). \tag{3}$$

Here, ρ_k and $C_k = \dfrac{\rho_k}{\rho}$ are the density and the mass concentration of the kth component; ε_0 and μ_0 are dielectric and magnetic constants; and ε_k' and ε_k'' are the real and imaginary parts of the permittivity for the kth component, respectively. The complex nature of $\dot{\varepsilon}$ indicates that the processes occurring in the medium are dissipative. This is explained by the fact that in high-frequency fields, the relaxation of polarization processes is delayed with respect to variation of the electromagnetic field and, as a result, they are nonequilibrium. The inertial properties of thermodynamic and hydrodynamic processes compared to electrodynamic processes make it possible to characterize the state of a medium by parameters averaged over the field period.

The mass-conservation law for the kth component and the system as a whole has the form [6]

$$\rho\frac{dC_k}{dt} = \rho\left(\frac{\partial C_k}{\partial t} + (\mathbf{u}\cdot\nabla)C_k\right) = -\operatorname{div}\mathbf{J}_k,$$
$$\frac{d\rho}{dt} = -\rho\operatorname{div}\mathbf{u}, \tag{4}$$

where $\mathbf{J}_k$ is the diffusion-flow density for the kth component and $\mathbf{u}$ is the averaged mass velocity:

$$\mathbf{J}_k = \rho(\mathbf{u}_k - \mathbf{u}); \quad \mathbf{u} = \rho^{-1}\sum_k \rho_k \mathbf{u}_k = \sum_k C_k \mathbf{u}_k;$$

$$\rho = \sum_k^n \rho_k, \quad \sum_k C_k = 1.$$

Bashkortostan State University,
ul. Frunze 32, Ufa, Bashkortostan, 450074 Russia

1028-3358/01/4603-0215$21.00

THERMODYNAMIC SUBSTANTIATION

To construct a phenomenological theory [7] of interaction between a multicomponent medium and a high-frequency electromagnetic field on the basis of the technique described in [8], we, using equations (1)–(4), derived expressions for both the entropy and thermodynamic flows. In the particular case of a two-component system, while ignoring the pressure-diffusion term and the dependence of the permittivity on the temperature and the field frequency, the diffusion flow and the heat flow take the form

$$\mathbf{J}_1 = -\mathbf{J}_2 = -\frac{L_{11}}{T}\left\{\frac{1}{1-C_1}\left(\frac{\partial \eta_1}{\partial C_1}\right)_{T,p,E,H}\nabla C_1\right.$$
$$+\left[\left(h_2 - h_1 + \frac{L_{q1}}{L_{11}}\right) + \frac{1}{2\rho}\varepsilon_0(\varepsilon_2' - \varepsilon_1')(\dot{E}\cdot\dot{E}^*)\right]\nabla T \quad (5)$$
$$\left.+\frac{\varepsilon_0(\varepsilon_2' - \varepsilon_1')}{2\rho}\nabla(\dot{\mathbf{E}}\cdot\dot{\mathbf{E}}^*)\right\},$$

$$\mathbf{J}_q = -\frac{L_{qq}}{T^2}\nabla T$$
$$-L_{q1}\left[(h_2 - h_1) + \frac{1}{2\rho}\varepsilon_0(\varepsilon_2' - \varepsilon_1')(\dot{\mathbf{E}}\cdot\dot{\mathbf{E}}^*)\right]\frac{\nabla T}{T^2} \quad (6)$$
$$-\frac{L_{q1}}{T}\left[\frac{1}{1-C_1}\left(\frac{\partial \eta_1}{\partial C_1}\right)_{T,p,E,H}\nabla C_1 + \frac{\varepsilon_0(\varepsilon_2' - \varepsilon_1')}{2\rho}\nabla(\dot{\mathbf{E}}\cdot\dot{\mathbf{E}}^*)\right].$$

Here, $\eta_k^{(\mathrm{em})}$ is the chemical potential of the system in the electromagnetic field with allowance for the equations of state (1),

$$\eta_k^{(\mathrm{em})} = \eta_k(T, \rho, C_1, \ldots, C_n) - \frac{1}{2\rho}(\varepsilon_0\varepsilon_k'(\dot{\mathbf{E}}\cdot\dot{\mathbf{E}}^*)),$$

and h_k is the enthalpy,

$$h_k = h_k - T\frac{\partial \eta_k}{\partial T},$$

for the kth component.

Omitting the terms associated with quantities of electric nature in expressions (5) and (6), we obtain the well-known equations for thermodynamic flows including, in addition to the terms of interdiffusion and heat conductivity [the first terms in (5) and (6), respectively], the cross Soret and Dufour terms [the second term in (5) and the third in (6), respectively]. In the case of a nonhomogeneous high-frequency electromagnetic field, the effects of electric diffusion and heat transfer under the action of the field take place [the last terms in (5) and (6), respectively]. As is seen from these expressions, the field action manifests itself in additional terms characterizing an increase in both the direct heat transfer and the cross thermal-diffusion transfer in thermal and diffusion flows, respectively, with a diffusion coefficient and a thermal-diffusion coefficient of

$$D = -\frac{L_{11}}{\rho T}\frac{1}{1-C_1}\left(\frac{\partial \eta_1}{\partial C_1}\right),$$
$$D_T = -\frac{L_{11}}{\rho T^2}\left(h_2 - h_1 + \frac{L_{q1}}{L_{11}}\right), \quad (7)$$

respectively, as well as an electric-thermal diffusion coefficient

$$D_T^E = -L_{11}\frac{1}{2\rho^2 T^2}\varepsilon_0(\varepsilon_2' - \varepsilon_1')(\dot{\mathbf{E}}\cdot\dot{\mathbf{E}}^*). \quad (8)$$

It is worth noting a feature of the transport phenomena associated with an effect of the high-frequency electromagnetic field. They occur only in the case of nonzero difference in the component's permittivity, as well as nonzero enthalpy difference in the case of a temperature gradient. The same result was obtained in [2] for polarizable media in the electrohydrodynamic approximation.

Thus, the microwave electromagnetic field manifests itself in two ways. On one hand, it acts directly via the effects of both the electric diffusion (with coefficient D^E) and the electromagnetic heat conduction (with coefficient λ^E) in the presence of a field-strength gradient. On the other hand, it acts latently, manifesting itself indirectly as a component of thermal-diffusion and thermal flows. Thus, in the case of the action of a high-frequency electromagnetic field, the total thermal-diffusion coefficient consists of two parts, namely, D_T and D_T^E, which correspond to the thermal diffusion in itself and the electric-thermal diffusion, respectively.

COMPARISON WITH THE EXPERIMENTAL DATA

The validity of the above theoretical conclusions was experimentally confirmed in studying the filtration of convection-diffusion flows of two-component hydrocarbon systems in a homogeneous high-frequency electromagnetic field [9]. As saturating fluids, we used high-viscous oil from the Igrinsk deposit (200 mPa s at 20°C) with a high content of polar components including asphaltenes (8.45%), resins (50%), and paraffins (4%), as well as purified kerosene. The processes of oil replacement by a solvent under the action of a high-frequency electromagnetic field were investigated with the help of an experimental setup whose principal part was a purposely designed oil-stratum model made of a nonconducting material, namely, a polyvinylchloride tube with an inner diameter of 22 mm and a length of 50 cm. Quartz sand with a fractional composition from 0.25 to 0.5 mm was used as a filler for the porous medium. The variation of the output solvent concentration was determined by photocolorimetric methods. This made it possible to qualita-

tively estimate the intensity of mass-exchange processes in the filtration flow under the action of the electromagnetic field. As a generator of the high-frequency field, we employed a 6-kW commercial VCHDZ-6/81 facility operating at a frequency of 81.36 MHz.

The model of the porous medium was placed inside the generator onto its lower electrode. A preliminary calibrated thermocouple connected to an ammeter was fixed at the model output. This procedure was applied for both monitoring the heat transfer and performing the test experiment under the action of the electromagnetic field. In this experiment, an identical model of the oil stratum was made, which was electrically heated to the same temperature as in the first experiment. An experiment was also performed in which oil was replaced by a solvent without any external action.

The measured concentrations (marked by dots) for one of the components (solvent) C_1 at the output of the porous-medium model are presented in the figure as a function of time. We have carried out three comparative experiments under identical conditions: without any external action, upon heating, and under the action of a high-frequency electromagnetic field.

On the basis of the experimental results and taking into account the simplified equation

$$m\frac{\partial C_1}{\partial t} + (\mathbf{v}\nabla)C_1 = D_f\nabla^2 C_1$$

under the boundary conditions

$$C_1(x, 0) = 0, \quad C_1(0, t) = 1, \text{ and } \frac{\partial C_1(L, t)}{\partial x} = 0,$$

the following values for the effective coefficients of the convective diffusion were obtained: $D_f^{\text{em}} = 0.215$ cm^2 s^{-1} under the action of the microwave electromagnetic field, $D_f^T = 0.169$ cm^2/s in the case of heating, and $D_f = 0.117$ cm^2/s in the absence of any external action.

Using the results of these experiments, we evaluated the corresponding cross parameters. Here, we based our calculations on the more complete convective diffusion equation and the heat conduction equation with the coefficients obtained for cross diffusion effects being taken into account:

$$m\frac{\partial C_1}{\partial t} + (\mathbf{v}\nabla)C_1 = D\nabla^2 C_1 + (\alpha_T + \alpha_T^E)D\nabla^2 T, \quad (9)$$

$$\rho c\frac{\partial T}{\partial t} + \rho_f c_f(\mathbf{v}\nabla)T = \lambda\nabla^2 T + Q. \quad (10)$$

Here, m is the porosity of the model; $\mathbf{v}$ is the averaged filtration rate; ρ and c and ρ_f and c_f are the densities and the specific heats of the medium and the mixture being filtered, respectively; and λ is the heat-conductivity coefficient for the saturated porous medium. Such values as the heat conductivity and the volumetric heat capacity are assumed to be additive and are determined by the expressions

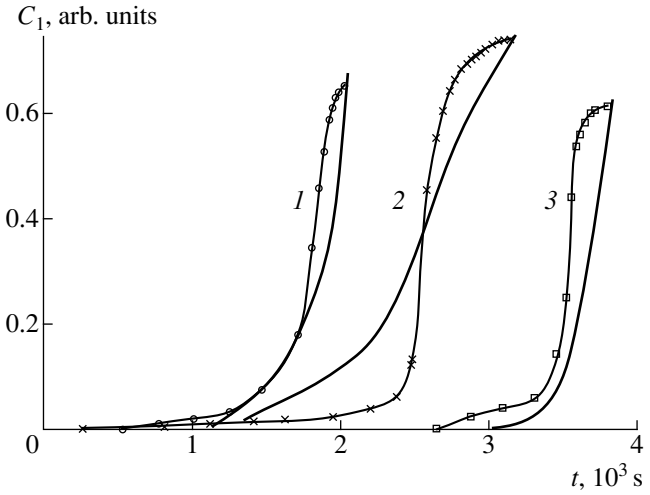

Solvent concentration at the output of the stratum model as a function of time: (*1*) thermal action, (*2*) action of the high-frequency electromagnetic field, and (*3*) absence of any action.

$$\lambda = (1 - m)\lambda_k + m(C_1\lambda_1 + C_2\lambda_2),$$

$$c\rho = (1 - m)\alpha_c + m(C_1\alpha_1 + C_2\alpha_2),$$

$$c_f\rho_f = C_1\alpha_1 + C_2\alpha_2,$$

where λ_c, λ_1, and λ_2 and α_c, α_1, and α_2 are the heat conductivity and volumetric heat capacity of the porous-medium skeleton, of the solvent, and of the oil, respectively.

The expression for distributed heat sources Q has the form [7]

$$Q = \frac{\omega\varepsilon_0\varepsilon'\tan\delta}{2}|E|^2, \quad (11)$$

where ω and E are the circular frequency and the intensity of the electromagnetic field, respectively, and $\tan\delta$ is the tangent of the dielectric loss in the medium.

With allowance for the conditions of the experiment, the problem (9)–(11) was solved in linear geometry at the following boundary conditions:

$$C_1(x, 0) = 0, \quad C_1(0, t) = 1, \quad \frac{\partial C_1(L, t)}{\partial x} = 0;$$

$$T(x, 0) = T(0, t) = T_0, \quad \frac{\partial T(L, t)}{\partial x} = 0.$$

Numerical calculations were performed for the following parameters corresponding to the physical properties of the medium and the experimental conditions: $T_0 = 22°$C, $m = 0.4$, $L = 0.5$ m, $\alpha_c = 2.038 \times 10^6$, $\alpha_1 = 1.582 \times 10^6$, $\alpha_2 = 1.913 \times 10^6$ J m^{-3} K^{-1}, $D = 1.17 \times 10^{-5}$ m^2 s^{-1}, $\lambda_c = 1.67$, $\lambda_1 = 0.122$, $\lambda_2 = 0.125$ W m^{-1} K^{-1},

$\varepsilon_2' = 3.426$, $\varepsilon_1' = 2.163$, $\tan\delta = 0.008274$, and $E = 11.1$ kV m^{-1}.

Comparison of the experimental and numerical results shows (see figure, solid lines) that in the case under consideration of convective diffusion transport, the total coefficient of the total thermal diffusion and the electric-thermal diffusion ($D_T + D_T^E$) exceeds, by more than an order of magnitude, the thermal-diffusion coefficient D_T in itself. The thermodynamic parameters determined as ratios of the coefficients of thermal diffusion and electric-thermal diffusion to the interdiffusion coefficient for the experiment described are equal to $\alpha_T = \dfrac{D_T}{D} = 0.0025$ K^{-1} and $\alpha_T^E = \dfrac{D_T^E}{D} = 0.115$ K^{-1}, respectively.

CONCLUSIONS

Thus, along with the well-known cross effects in multicomponent systems, a new phenomenon arises under the action of high-frequency electromagnetic radiation, namely, cross mass transfer by electric-thermal diffusion. The effect of the electric-thermal diffusion can be quite essential and can considerably exceed the conventional transfer by the thermal diffusion. This is caused by the fact that the thermal diffusion is determined by only the internal system parameters, i.e., the difference in the component enthalpies (or chemical potentials), whereas the electric-thermal diffusion is determined by both the internal (difference of the component's permittivity) and the external parameters (in the case under consideration, by the electric-field intensity squared).

Although the values obtained for the parameters α_T and α_T^E relate to the experimental conditions which we dealt with, it is important that the effect of the electric-thermal diffusion is confirmed by the ratio of these parameters rather than by their absolute values. The effect under discussion takes place in all cases when, under the action of a high-frequency electromagnetic field, there exists a permittivity-dispersion region dependent on the field frequency. As is well-known, in the dispersion frequency region, the tangent of the dielectric-loss angle, i.e., $\tan\delta$, represents a resonance curve which corresponds to the maximum dissipation of the electromagnetic energy in a medium and the maximum degree of its polarizability. In the case of a multicomponent system consisting of components with different permittivities, a nonhomogeneous-polarization field arises under the action of electromagnetic radiation. This, evidently, intensifies the mass transfer with the transport factor proportional to the electric-field intensity squared.

REFERENCES

1. L. I. Sedov, *Mechanics of Continua* (Nauka, Moscow, 1973).
2. V. V. Gogosov, V. A. Naletova, and G. A. Shaposhnikova, Prikl. Mat. Mekh. **43**, 489 (1979).
3. K. P. Gurov, *Phenomenological Thermodynamics of Irreversible Processes* (Nauka, Moscow, 1978).
4. A. A. Shteĭn, Prikl. Mat. Mekh. **41**, 271 (1977).
5. L. D. Landau and E. M. Lifshitz, *Course of Theoretical Physics*, Vol. 8: *Electrodynamics of Continua* (Nauka, Moscow, 1982; Pergamon, New York, 1984).
6. R. I. Nigmatulin, *Principles of Mechanics of Heterogeneous Media* (Nauka, Moscow, 1978).
7. S. R. de Groot and P. Mazur, *Nonequilibrium Thermodynamics* (North-Holland, Amsterdam, 1962; Mir, Moscow, 1964).
8. Boa-Te-Chu, in *Plasma in Magnetic Field and Direct Heat Energy Conversion in Electric Energy* (Gosatomizdat, Moscow, 1962), pp. 62–83.
9. F. L. Sayakhov, L. A. Kovaleva, M. A. Fatykhov, and F. S. Khismatullina, Élektron. Obrab. Mater., No. 1, 59 (1995).

Translated by Yu. Vishnyakov